Formation of Transition Metal Chalcogenide Thin Films by Electrochemical Atomic Layer Deposition (E-ALD)

by

Chu Fan Tsang

(Under the direction of John Lewellen Stickney)

Abstract

This dissertation describes the deposition of transition metal dichalcogenide (TMDC) thin films by electrochemical atomic layer deposition (E-ALD). E-ALD was proposed to grow chalcogenide (S, Se and Te) films involving valve metals (Ta, Nb and Ti). Tantalum is a refractory metal that readily forms a stable and protective surface oxide layer when exposed to ambient conditions. In a Ta chalcogenide deposition process, the surface oxide of Ta must be removed prior to depositing a chalcogen onto it. The nature of the Ta oxide was studied, and attempts to electrochemically reduce the oxide were made. Te, S, and Cu were deposited onto reduced Ta surfaces. These processes were examined by in-situ electrochemical scanning tunneling microscopy (EC-STM), cyclic voltammetry (CV), and X-ray photoelectron spectroscopy (XPS).

Molybdenum is another valve metal that is electrochemically similar to tantalum. The electrochemistry of Mo was also investigated with the intent to form Mo chalcogenides using E-ALD. Preliminary $MoSe_2$ films were grown by this method. The electrodeposition processes were explored using CV, coulometry. and XPS. The $MoSe_2$ films were characterized by electron probe micro-analyzer (EPMA), X-ray diffraction (XRD), photoelectrochemistry (PEC), scanning electron microscopy (SEM), scanning tunneling microscopy (STM), micro-Raman spectroscopy, and XPS.

INDEX WORDS: Transition Metal Dichalcogenides, Tantalum, Molybdenum, Copper, E-ALD, UPD, Electrodeposition, Cyclic Voltammetry, Photoelectrochemistry, Thin Film, EC-STM, EPMA, Raman, XPS, UHV

Formation of Transition Metal Chalcogenide Thin Films by Electrochemical Atomic Layer Deposition (E-ALD)

by

Chu Fan Tsang

B.S. Chem, University of Georgia, 2010

A Dissertation Submitted to the Graduate Faculty
of The University of Georgia in Partial Fulfillment
of the
Requirements for the Degree

Doctor of Philosophy

Athens, Georgia

2015

Formation of Transition Metal Chalcogenide Thin Films by Electrochemical Atomic Layer Deposition (E-ALD)

by

Chu Fan Tsang

Approved:

Major Professor: John Lewellen Stickney

Committee: I. Jonathan Amster
Jeffrey L. Urbauer

Electronic Version Approved:

Suzanne Barbour
Dean of the Graduate School
The University of Georgia
December 2015

Acknowledgments

First and foremost, I thank my loving parents for their lifelong devotion to shaping me into a better person. Their dedications have been unwavering, and their sacrifices gave me the opportunity to pursue my interests. I also wish to acknowledge my first high school chemistry teacher Larry Chappell for inspiring me to become a chemist, my undergraduate advisor Dr. Wayne Suggs for sparking my interest in analytical chemistry, and my graduate advisor Dr. John Stickney for encouraging me to enroll in graduate school. Coincidentally, they all share an uncanny resemblance to Santa Claus.

I wish to further thank Dr. John Stickney for his role in creating a challenging and educational environment. His guidance and support go well beyond the chemistry in laboratories. For that, I am grateful. Former and current members of the Stickney group have also been very supportive. In addition to their many helpful scientific discussions, their presence made working in a basement much more tolerable.

Table of Contents

Chapter 1

Introduction and Literature Review

TaX_n and NbX_n (X = S, Se, or Te; n = 2 or 3) are transition metal chalcogenides (TMCs) that belong to a family of highly-anisotropic compounds. The anisotropy arises from the nature of the layered structures these materials possess. Similar to graphenes in graphite, the TMCs have strong in-plane bonding and relatively weak out-of-plane van der Waals interactions among layers. Variations in stacking orders of these TMC layers and in the transition metal coordination can lead to a multitude of different polytypes when the bulk crystals are formed.[1,2] While the properties of bulk transition metal chalcogenides have been studied and known for decades, knowledge on the two-dimensional (2D) forms of these materials are less pervasive. There has recently been a heightened interest in applications of TMCs in electronics and opto-electronics devices. The attention is focused particularly on the 2D nanosheets of the TMCs, which may exhibit properties different from the corresponding bulk materials.

Many dichalcogenides and trichalcogenides of tantalum or niobium possess properties of superconductivity and/or charge-density waves (CDW).[3] For example, one-dimensional $TaSe_3$ becomes superconductive below 2.1 K.[4] $NbSe_3$ undergoes two phase transitions at 145 K and 59 K, below which anomalies in resistivity and specific heat occur due to the formation of charge density waves.[5] Disulfides and diselenides of niobium and tantalum have also been reported to possess superconductivity and CDW characteristics. 1T-TaS_2 has a relatively-high CDW transition temperature at 352 K, and 1T-$TaSe_2$ has one at 473 K.[6,7]

Electrons' charge density normally appears uniform and random in space for metals at room temperature. However, these free electrons tend to pair at low temperatures. For many of such tantalum or niobium chalcogenide compounds, self-organization can occur below a critical transition temperature, T_c, whereby the electrons interact in such a way that leads to a periodic distortion of the underlying lattice. Such electron interaction and lattice distortion result in an ordered structure where charge varies in space. The spatial periodic modulation of the charge density is called a charge-density wave.[8]

For materials in a CDW state at a temperature below T_c, the CDW is normally pinned by defects of the underlying lattice. However, the CDW can be depinned by applying an electric field having field strength above a threshold, E_T. Once depinned, the CDW becomes mobile and produces a collective current that can be used in information processing applications. Recent experimental and theoretical works have demonstrated that thin films of transition metal chalcogenides obtained from exfoliating the bulk crystals exhibit an increased T_c closer to room temperature.[9,10] This augments the applicability of CDW for use in electronic and optoelectronic devices and provides motivations for growing and studying thin films of the CDW materials.

A goal of this project was to grow the aforementioned transition metal chalcogenides using a synthesis route that is suitable for use in device fabrication. Conventional and non-conventional methods for growing some of the chalcogenide compounds as presented in the literature will be described. The feasibility of each method for use in device fabrication will also be evaluated. An electrochemical synthesis route using aqueous solutions was proposed for this project, and it will be described as well.

The most common method for growing high-quality single crystals of tantalum or niobium chalcogenides has been Chemical Vapor Transport (CVT) within a sealed quartz ampoule. By the CVT growth method, the starting materials can be pure elemental forms of the transition metal and of the chalcogen mixed in stoichiometric

quantities. Polycrystalline forms of the binary compound from a separate synthesis can also be used as the starting material. A few grams of the starting mixture are placed inside a fused quartz ampoule of about 30 cm long and about 2 cm wide. A catalytic transport agent is also added to the original mixture. This transport agent aids the movement of the non-volatile starting material within the ampoule by carrying it into the vapor phase. I_2 is the most efficient and widely-used foreign transport agent. ICl_3 and chalcogen halides (S_2Cl_2, Se_2Cl_2, $TeCl_4$, .etc) can also be used. These foreign transport agents are typically added in 5–10 mg cm^{-3} ampoule volume. If a foreign species is not desired, 5 to 10 mol % of excess chalcogen can be added to serve as the transport agent instead.[11]

Once all the necessary reagents are inserted into one end of the quartz ampoule, it is purged with an inert gas, evacuated to $\sim 10^{-6}$ Torr, and then sealed. The sealed ampoule is placed in a gradient furnace, which usually has two or three zones, and a temperature gradient is established over the length of the ampoule. The rate of heating can vary and is usually on the order of 50 °C h^{-1}. Once the targeted temperature gradient is established, it is maintained over the course of several days to allow the reagents to react and/or the transport to occur. Ideally, majority of the reaction between the transition metal and the chalcogen take place during this period. The polycrystalline product that forms is carried over by the transport agent to the opposite end of the ampoule, where the single crystal product forms by nucleation and growth. A forward or reverse gradient is used depending on the nature of the reaction between the transport agent and the reactant. A forward gradient – source end hottest – is used if that reaction is endothermic. By the same rationale, a reverse gradient – source end coldest – is used if the reaction is exothermic.[12]

The magnitude of the gradient can also affect the crystal growth. A smaller gradient will result in slower transport, which usually yields smaller and less crystals but of a higher quality.[11] The final step following the reactant transport is the cooldown.

Usually, a slow cooldown is desirable at a speed similar to that used for the initial warm up period. Instead of a slow cooldown, a quick one can sometimes be used by water-cooling the ampoule, which effectively quenches the reaction. At the end of the reaction, the total mass of transported crystal is usually a few percent of the mass of the starting materials.[12]

A wide range of temperature gradients have been reported in the literature for growing crystals of tantalum or niobium chalcogenides. The chosen temperatures are mostly dictated by the particular transition metal chalcogenide compound to be grown, reaction time, starting materials, and the desired polytype. Average temperatures along the growth ampoules were reported anywhere from 600 to 900 °C. The reported temperature gradients were usually within 50 °C and 80 °C.[11–15]

Some of the highest-quality transition metal chalcogenide single crystals have been made using the CVT method. However, the average synthesis takes a week. The required high temperatures are fatal to most substrates, thus prohibiting the ability to grow directly onto devices by this method. Potentially elaborate cleaning steps must be taken to ensure that walls of the quartz ampoule are free of contaminants. The layered characters of these chalcogenide materials permit contaminants to easily intercalate into the van der Waals gap, which may be detrimental to the quality of the final product. Since pure Nb/Ta are very reactive with oxygen, the partial pressure of oxygen must be kept to a minimum by thoroughly purging the ampoule with an inert gas prior to evacuating and sealing it preferably inside an inert atmosphere.

Growth methods alternative to CVT have been known. Schuffenhauer et al. explored the gas-phase synthesis of TaS_2 using atmospheric pressure chemical vapor deposition (APCVD).[16] $TaCl_5$ and H_2S were used as precursors and N_2 as the carrier gas. $TaCl_5$ powders were vaporized and brought into the center of a furnace by a N_2 stream. Sulfidization to TaS_2 occurs as the vaporized Ta precursor reacts with a stream of H_2S in the furnace at a temperature between 450 °C and 600 °C. The

sulfidization step is followed by a nucleation and growth mechanism to form nanoparticles. The products formed in the gas phase were collected by filters at the end of the furnace. Fullerene-like TaS_2 nanoparticles having diameters from 20 nm to 80 nm were collected.

While optimizing the growth conditions, the furnace temperature was varied between 210 °C and 800 °C. Lower temperatures below 300 °C resulted in poorer crystallinity as amorphous nanoparticles were observed; higher temperatures above 700 °C resulted in larger platelet TaS_2 having higher crystallinity. The APCVD growth had reaction times of only 15 s to 20 s, which is a significant advantage over the CVT method. However, the platelet forms of TaS_2 may be more desirable for exfoliation and CDW studies. The higher temperatures required to form these platelets are comparable to those used for CVT growth, limiting the use of APCVD.

Kikkawa et al. attempted to grow trisulfide and triselenides of Ta and Nb at high pressures.[17] In the high-pressure synthesis, powdered Ta/Nb and S/Se in a stoichiometric mix were place in a cubic anvil device, which was subjected to 700 °C and 2 GPa for 30 min. The resulting product was polycrystalline. Attempts to grow single crystals by melting the product with excess chalcogen and solidifying at different cooling rates were unsuccessful.

Stender et al. used a solution-based one-pot synthesis method to grow transition-metal chalcogenides in general and grew TaS_2, $TaSe_2$, and $NbSe_2$ nanoplates between 15 nm and 60 nm thick and 300 nm to 800 nm wide.[18] $TaCl_5$/$NbCl_5$, elemental S/Se, and dodecylamine (surfactant) were combined in a flask under N_2 to react at 250 °C for 2–4 h. The intermediate was then extracted with hexane and further heated in a quartz flask under N_2 at 650 °C for 2–4 h.

Ueno et al and Shimada et al. grew ultrathin films of $NbSe_2$ and $TaSe_2$ using a technique called van der Waals epitaxy (VDWE), which is molecular beam epitaxy (MBE) that proceeds with van der Waals forces.[1,19] By relying on the layered-nature

of these materials, the authors claimed heteroepitaxy with up to 50 % lattice mismatch can be achieved. Ta/Nb was e-beam deposited while Se/S was sublimed from a Knudsen cell. Substrate temperatures were about 500 °C. Films of thickness up to 16 monolayers were grown, and good crystallinity and flatness were reported.

The aforementioned non-electrochemical growth methods tend to involve high temperature and/or pressure. Growth time is usually long as well. The idea of an electrochemical growth method is enticing for making the tantalum or niobium chalcogenide films, as the growth conditions are usually close to ambient and therefore are easily attainable. The depositions of Te, Se and S have been studied and are fairly well-known by the Stickney group.[20–24] Tantalum and niobium, however, are far more difficult to electrodeposit since aqueous electrochemical studies of the two transition metals under ambient conditions are scarce in the literature. Previous attempts to electrodeposit tantalum or tantalum alloys in aqueous solutions typically involved using temperatures between 65 °C and 90 °C at various pH conditions under constant current densities. Those electrodeposition attempts were not reproducible.[25]

Tantalum and niobium have similar atomic radius as a result of lanthanide contraction, and the two metals also share a great deal of similarities in their coordination chemistry.[26,27] A common misconception is that Ta and Nb are highly corrosion resistant, but the two metals are in fact highly reactive. Under ambient conditions, both tantalum and niobium react with oxygen to form a passive oxide layer.[28] This surface oxide has excellent corrosion resistance and causes the metals to appear highly inert under most conditions. In the presence of this oxide, tantalum is immune to attacks by common acids such as HCl, H_2SO_4, and HNO_3. It is even resistant to aqua regia and caustic alkali solutions.[29] The protective oxide layer is known to screen the metal surface from solution, inhibiting electron transfer and/or resulting in poor film adhesion.[30–33] In order to grow high quality deposits, the oxide must first be removed.

The most thermodynamically-stable oxides of tantalum and niobium are Ta_2O_5 and Nb_2O_5, respectively.[34] The common halide salts of Ta/Nb are soluble in some polar organic solvents, but they readily decompose in water into the insoluble Ta_2O_5 or Nb_2O_5. Aqueous chemistry of tantalum and niobium are therefore limited. In order to cleanly electrodeposit Ta or Nb, a soluble precursor of the respective metals in aqueous solutions is necessary.

A Ta/Nb complexing agent is needed to dissolve the metals in aqueous solutions by preventing precipitation into their respective oxides. Hydrofluoric acid is the most commonly-known among the few reagents capable of penetrating the protective oxide to attack the metals.[27,29,35,36] Ta/Nb dissolves in HF by forming mostly anionic fluoride and oxyfluoride complexes. The number of fluoride ligands per tantalum varies as a function of HF concentration, and tantalum oxyfluorides are more likely to form at HF concentrations below 0.1 M.[37–39] Voltammetric and impedance studies have been done on Ta electrodes in HF to show the dissolution of Ta and Ta_2O_5 into soluble tantalum fluoride complexes.[40,41] Similar trends in solubility and fluoride complexes are expected in an Nb−HF system, since Ta and Nb tend to share very similar physical and chemical properties.

Aqueous Ta−HF and Nb−HF solutions are conceptually simple to prepare by dissolving the respective metal oxides in HF; however, HF is extremely hazardous to health. A certain level of free fluoride ions is needed in solution in order to maintain a desired concentration of a particular Ta/Nb fluoride complex. The fluoride ions can potentially etch instruments and/or substrates, so fluoride may not be desirable as the complexing agent. Soluble Ta/Nb complexes have been known to form in aqueous solutions of oxalic, tartaric and citric acids. Water-soluble complexes with peroxides, some α-hydroxy acids and some amines have also been reported.[26,42]

The first step of preparing soluble Ta/Nb solutions reported in the literature usually involves obtaining the hydrated oxides of the respective metals. The hydrated

oxide can then be dissolved in H_2O in the presence of a proper complexing agent. The hydrated metal oxides, sometimes referred to as Ta/Nb hydroxides or tantalic/niobic acids, can be obtained by fusing the metal oxides with KOH in a crucible at 400–500 °C for 2–5 h. To obtain a peroxo complex, the melt is filtered and dissolved in H_2O and excess H_2O_2 while hot.[43] To obtain the hydrated oxide, the melt is dissolved in H_2O and filtered. The hydrated oxide is precipitated from the resulting clear solution by addition of glacial acetic acid followed by filtration or centrifugation.[44]

An alternative way to obtain the hydrated metal oxide is by first dissolving Ta_2O_5 or Nb_2O_5 in HF. Addition of ammonia to the clear solution will precipitate out the hydrated metal oxide, which can then be filtered and isolated.[45–47] Addition of ammonia to a colloidal suspension created by adding the metal chloride salt to H_2O will also form the hydrated oxide.[48] Once the hydrated metal oxide is obtained, it can be dissolved in H_2O with stirring and heating in the presence of a stoichiometric excess of tartaric acid, citric acid or oxalic acid.

Electrochemical atomic layer deposition (E-ALD) was proposed as the method of choice for growing Ta/Nb chalcogenide films in this project. E-ALD is the electrochemical form of ALD, which is a method to form materials one atomic layer at a time. Conventional ALD is a gas-phase technique. Very fine control is possible in ALD because the reactions involved are surface-limited. Exposing a substrate to a sequence of gases, in which each gas deposits up to only one atomic layer onto the substrate, constitutes a cycle. The thickness of the material is determined by the number of cycles used during the material growth. Materials formed by ALD usually have exceptional quality.

In E-ALD, electrochemical surface-limited reactions, generally referred to as underpotential deposits (UPD), are used.[22,49,50] UPD is where the first atomic layer deposits at a potential prior to, or under, that where the element deposits onto itself. It results from the free energy of formation of a surface alloy or compound. The

surface-limited nature of UPD is generally used in an E-ALD cycle, where solutions containing different elements are exchanged at controlled potentials. Thin films of desired thicknesses are formed by repetition of that cycle.

Figure 1.1 shows the schematic of an E-ALD flow cell system. Different precursor solutions and blank rinsing solutions are contained in their own bottles. The bottles are individually connected to a distribution valve, which is in turn connected to a flow cell and a peristaltic pump. The solution bottles, the valve, and majority of the solution tubes are housed within a Plexiglas box. The solutions and the box are directly purged with nitrogen to exclude air from interfering with the electrochemical reactions of interest. Both the distribution valve and the pump are digitally controlled by a controller board interfaced to a computer. That allows the computer to select a particular solution to pump through the flow cell. The flow cell is a 3-electrode electrochemical cell that contains a planar substrate as the working electrode, a 3 M Ag/AgCl reference electrode, and a Au wire auxiliary electrode parallel to the working electrode. Figure 1.2 shows the schematics for a version of the E-ALD flow cell. Compared to a conventional electrochemical cell setup, this flow cell has the additional advantage of excluding air from the reactants and the ability to change solutions without losing potential control of the working electrode. The potentiostat that controls and monitors the potential and current of the flow cell is also interfaced to the computer. Since the potential controls and the solution flows are managed through the computer, a vast number of electrochemical experiments and depositions can be automated.

For the purpose of growing tantalum and niobium chalcogenide films, the electrodepositions of Ta and Nb from a soluble species are requisites. No report of successful tantalum or niobium deposition in aqueous solutions is known from the literature, so experimental values of Ta/Nb deposition potentials are not available. Based on the Gibbs energy of formation for Nb_2O_5, Latimer calculated the electrode poten-

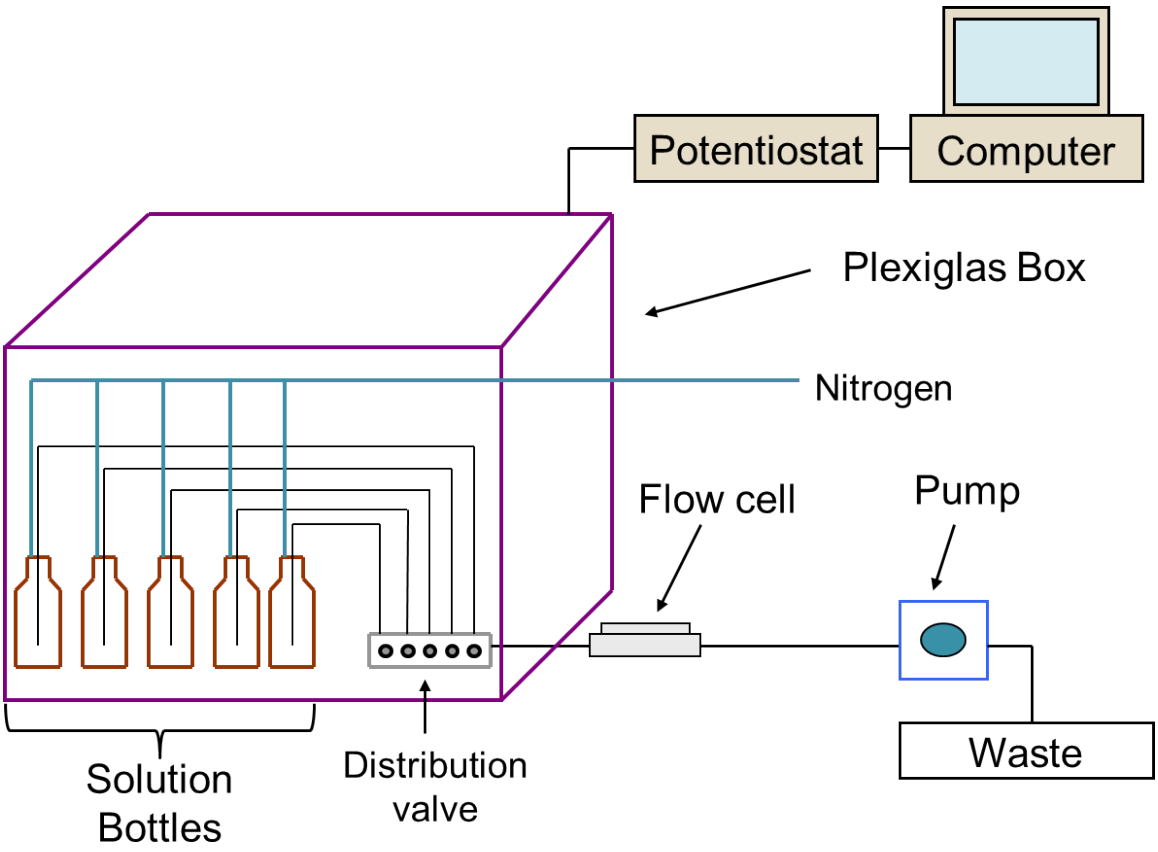

Figure 1.1: Schematic of an E-ALD flow cell system.

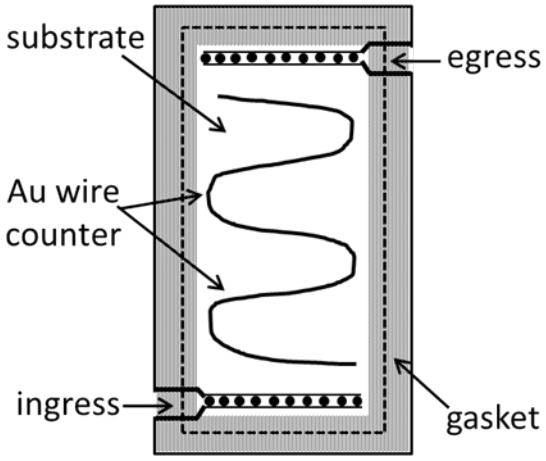

(a)

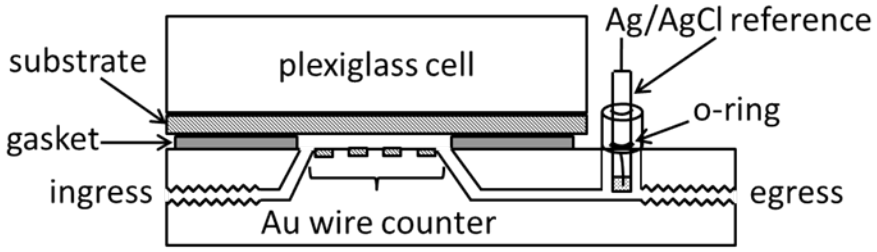

(b)

Figure 1.2: Schematics for a version of the flow cell. (a) Top-down view of the cell showing the planar working electrode parallel to the page. (b) Side view of the cell showing the planar working electrode perpendicular to the page.

tial E^0 for the reduction of the niobium pentoxide to niobium metal to be $-0.65\,\mathrm{V}$.[51] Pourbaix reported the theoretically calculated E^0 for reduction of tantalum pentoxide to tantalum to be $-0.75\,\mathrm{V}$.[29] Attempts to deposit Cu onto Ta suggested that the oxide can be reduced by applying an overpotential.[32,33,52]

Bulk sulfur deposition from a sulfide solution occurs positive of $-0.6\,\mathrm{V}$ vs. Ag/AgCl.[20] Se deposition occurs at potentials negative of $-0.7\,\mathrm{V}$ in a pH 4.7 Se solution.[21] Bulk Te can deposit over a wide range of potentials from $0.2\,\mathrm{V}$ to $-0.8\,\mathrm{V}$, depending on the solution pH.[53] Based on the experimentally-reported potentials for depositions of the chalcogens, S/Se/Te can possibly coexist at the same potentials where Ta/Nb should be reduced.

While experimental data demonstrated that it is possible to deposit Te and S onto a reduced Ta surface, the attempts to electrodeposit Ta or Nb were met with extreme difficulties. The preliminary Ta/Nb precursor solutions made by following recipes found in the literature were prone to precipitation. Due to the lack of a reliable carboxylate-based precursor along with the hazards involved in using HF either during the synthesis steps or as a final complexing agent, the objective to grow Ta/Nb chalcogenides by E-ALD was deferred. Instead, the focus was shifted toward studying the electrodeposition of molybdenum for the purpose of forming molybdenum dichalcogenides. Because the electrodeposition of molybdenum dichalcogenides is also challenging owing to the difficulties in depositing molybdenum, a successful method for electrodepositing molybdenum dichalcogenides might be applicable for depositing Ta/Nb chalcogenides.

Aside from growing molybdenum dichalcogenides, understanding the electrochemistry of Mo is also crucial for making materials for photovoltaic (PV) devices. In the area of PV, Mo is commonly used as a back contact for the absorber material.[54–56] A detailed understanding of the Mo surface would be essential for electrochemical growth of the absorber material onto the substrate. For example, poor adhesion of

the absorber to the substrate may adversely affect the electron-hole transport characteristics and lead to lower device performance.[57] The ability to modify the substrate to improve the interface between Mo and the absorber is therefore highly desirable.

MoX_2 belongs in the category of transition metal dichalcogenides (TMDCs) that has the general formula MX_2, where M is a transition metal (such as Ta, Nb, Mo, or W) and X is a chalcogen (S, Se, or Te).[2] TMDCs are a subset of 2D materials that have garnered much attention from material chemists, physicists, and engineers. It is a blooming field that trails the glamour brought about by graphene, which is commonly seen as the epitome of a 2D material.[58,59] Since intrinsic graphene has no band gap, semiconductor TMDCs such as MoX_2 and WX_2 are seen as promising complements to graphene.[60] Unlike graphite, which is composed entirely of one element and the graphene sheets are only one atom thick, TMDCs are structurally more complicated. Similar to graphite, bulk TMDCs are also composed of sheets that interact with each other via van der Waals forces.[61] However, each MX_2 sheet is a trilayer made up of a transition metal center layer sandwiched by two chalcogen layers. The interaction among these layers within the trilayer is covalent. Depending on the stacking orientations of the trilayers with respect to each other, different structural polytypes can exist for the bulk material.

Properties of molybdenum dichalcogenides and tungsten dichalcogenides, especially the disulfides, have been widely investigated for their potential applications. As the material thickness decreases, the band gaps of MoX_2 and WX_2 exhibit a crossover from indirect to direct transitions in the limit of a single layer.[62–65] These particular materials also have band gap energies in the UV-visible region, making them potential materials to be used in making photonic and optoelectronic devices.[66,67] In the area of renewable solar energy research, $MoSe_2$ and WSe_2 can be used as a catalyst or as a catalyst support for hydrogen evolution reaction (HER).[68–72] Group VI transition metal dichalcogenides such as $MoSe_2$ and MoS_2 are potentially more suitable than

semiconductors such as CdS, CdSe, PbS and GaAs as photoelectrodes in regenerative electrochemical solar cells. The photogenerated excitons in these TMDCs originate from the non-bonding *d*-orbitals, thus the photoinitiated reactions arising from these transitions do not directly result in broken crystal bonds, making these materials less susceptible to photodecomposition.[73]

Individual MX_2 materials already exhibit very unique properties for a wide range of potential applications. For example, the thicknesses of few-layer MoS_2 flakes are identifiable by their Raman frequency shift.[74]. MoS_2 also exhibits dramatically higher photoluminescence quantum yield as the thickness decreases.[63] More interesting characteristics can be observed by combining different MX_2 as heterostructures or alloys.[75,76] By forming heterostructures of two different MoX_2, properties such as the band gap, band offset, carrier densitiy, and polarity can become more tunable.[77] The isomorphic nature of the TMDCs makes substitution at the atomic level possible without phase separation.[78] For instance, MoS_2 can be doped with Se to have the Se substitution occur only at the S sites. By controlling the dopant concentration, the band gap can be continuously tuned between that of MoS_2 and of $MoSe_2$.

Heterostructures of MoX_2 and WX_2 generally come in two forms: stacked heterostructures and lateral heterostructures. The stacked heterostructures are formed by the vertical interaction of one trilayer of a MX_2 material with another trilayer of a different MX_2 material. The interaction is through van der Waals forces similar to the interaction among trilayers within the bulk of the same MX_2 material. Lateral heterostructures are formed by in-plane interconnection of two different MX_2 materials at a heterojunction. The interaction at the heterojunction is covalent just as the interaction between the transition metal and the chalcogens within a trilayer of the same MX_2 material. Obtaining one heterostructure over another can be a function of the growth temperature.[79] A new band gap different from those of the individual

MX_2 components can arise as a result of coupling between the two different MX_2 layers in the stacked structure.[80]

More attentions appear to be focused on lateral heterostructures because of interests in the lateral heterojunction. A lateral heterojunction between two different MX_2 materials can form a p-n junction with an atomically sharp interface. Such a junction holds the prospect of creating monolayer p-n rectifying diodes, light-emitting diodes, photovoltaic devices, and bipolar junction transistors.[77] Similar to the stacked heterostructures, the lateral structures can possess a new band gap different from those of the individual MX_2 components. Within the monolayer lateral heterostructure, the original band gaps of the individual MX_2 components can still exist on their respective sides across the interface. Furthermore, a new band gap can be found at the heterojunction. Additionally, photoluminescence at the heterojunction is more intense than at either sides of the junction.[81]

While particular TMDCs such as TaX_2 and TiX_2 are commonly grown by the CVT method to make pristine bulk single crystals, chemical vapor deposition (CVD) has recently become more commonly used for growing MoX_2 and WX_2.[60,82,83] The CVD growth of Mo/W dichalcogenides were usually restricted to a few monolayers because the interests were mostly focused on their few-layer properties.[84] Contrary to exfoliation of CVT-grown crystals, CVD is a bottom-up growth method that eliminates the need for exfoliation when monolayers are desired.[85]

The setup for CVD of Mo/W chalcogenides shares some resemblance to the setup for CVT. In both CVT and CVD, the reactions are carried out in a horizontal quartz tube furnace. A main difference is that the tube is not sealed and no foreign transport agent is needed in the CVD. In place of a transport agent, a carrier gas stream assists in the transport of reactants. Inside the quartz tube, unlike in CVT, the reactants are placed in separate locations, and a Si/SiO_2 substrate is generally used. Since the reactants and substrate are placed at different locations, they can be heated separately

to different temperatures during growth. The reactants are always placed upstream of the carrier gas flow while the substrate is placed downstream.[84]

When growing Mo dichalcogenides, the precursors may be pre-synthesized MoX_2 powders.[81] More commonly, the precursors are the chalcogen in its elemental state and MoO_3.[78,83,84,86,87] Relative to the gas flow, the chalcogen is placed upstream, followed by the MoO_3 downstream, then the substrate. The carrier gas is mostly inert, usually N_2/Ar, and might or might not contain H_2 depending on the chalcogen.[67,88] The reaction temperatures can reach up to 850 °C. For WX_2 growth, the precursor can be WX_2 powders, similar to the case of MoX_2.[81] The precursors can also be the chalcogen powders in their elemental state placed upstream while either W powder is placed onto the substrate or WO_3 is pre-deposited onto the substrate downstream.[89]

The Penner group had created MoS_2 nanowires by an interesting combination of electrodeposition with vapor phase reactions. The group originally devised a method to create Mo nanowires selectively onto step edges of HOPG substrates.[90,91] The method involves first electrodepositing MoO_2 onto the HOPG step edges. Because the step edge sites of HOPG are significantly more reactive than the terrace sites, MoO_2 can be deposited exclusively onto the step edges by properly controlling the substrate potential. Following the MoO_2 electrodeposition, the deposit was transferred to a tube furnace where the MoO_2 nanowires were reduced to metallic Mo nanowires in the presence of H_2 (10 % H_2/90 % N_2) at 500 °C. This method of preparation was referred to as electrochemical step edge decoration (ESED).

Following the initial work done on creating the Mo nanowires, the group extended the work to make MoS_2 by the same method.[92] Initially in the preparation, MoO_x was again electrodeposited onto step edges of HOPG by ESED. The MoO_x-decorated substrate was then transferred into a tube furnace where it was exposed to flowing H_2S at 500–1000 °C. Sulfidization of the MoO_x occurred for 5–84 h to convert the MoO_x into MoS_2. Two types of MoS_2 was formed as a function of the temperature

used. Between 500 °C and 700 °C, 2H-MoS_2 nanowires were formed. Above 800 °C, 3R-MoS_2 nanoribbons were made.

The formation of $MoSe_2$ by E-ALD was attempted in this project. In the electrochemical formation of $MoSe_2$, a major obstacle lies in the difficulty in electrodepositing Mo. Metallic Mo electrodeposits at a potential where HER can thermodynamically occur. In theory, Mo electrodeposition can proceed by the reaction[35,93]

$$MoO_4^{2-} + 4\ H_2O + 6\ e^- \longleftrightarrow Mo + 8\ OH^- \qquad E^0 = -0.913\,V \text{ vs. S.H.E.} \quad (1.1)$$

Pure Mo electrodeposition from aqueous solutions typically has ∼1 % current efficiency at best due to the concurrent HER as the dominant side reaction.[94,95] Mo deposition can be facilitated by depositing it as an alloy with Fe, Co, or Ni.[96,97] The success in codepositing Mo as an alloy with an Fe-group metal guided the prospect of using chalcogen to induce Mo electrodeposition.[98–101] The present work examines the electrodeposition of Mo together with Se by E-ALD. The interaction between the electrodeposited Mo and Se led to the formation of $MoSe_2$. While the as-deposited films contained significant amount of oxide impurity, the film compositions can be improved by annealing at temperatures considerably lower than those used in CVD of MX_2.

References

(1) Shimada, T.; Nishikawa, H.; Koma, A.; Furukawa, Y.; Arakawa, E.; Takeshita, K.; Matsushita, T. Polytypes and crystallinity of ultrathin epitaxial films of layered materials studied with grazing incidence X-ray diffraction. *Surface Science* **1996**, *369*, 379–384.

(2) Wang, Q. H.; Kalantar-Zadeh, K.; Kis, A.; Coleman, J. N.; Strano, M. S. Electronics and optoelectronics of two-dimensional transition metal dichalcogenides. *Nat Nano* **2012**, *7*, 699–712.

(3) Wilson, J. A.; Disalvo, F. J.; Mahajan, S. Charge-Density Waves in Metallic, Layered, Transition-Metal Dichalcogenides. *Physical Review Letters* **1974**, *32*, 882–885.

(4) Sambongi, T.; Yamamoto, M.; Tsutsumi, K.; Shiozaki, Y.; Yamaya, K.; Abe, Y. Superconductivity in One-Dimensional $TaSe_3$. *Journal of the Physical Society of Japan* **1977**, *42*, 1421–1422.

(5) Monceau, P.; Ong, N. P.; Portis, A. M.; Meerschaut, A.; Rouxel, J. Electric-Field Breakdown of Charge-Density Wave-Induced Anomalies in $NbSe_3$. *Physical Review Letters* **1976**, *37*, 602–606.

(6) Beal, A. R.; Hughes, H. P.; Liang, W. Y. Reflectivity Spectra of Some Group Va Transition-Metal Dichalcogenides. *Journal of Physics C-Solid State Physics* **1975**, *8*, 4236–4248.

(7) Wilson, J. A.; Disalvo, F. J.; Mahajan, S. Charge-Density Waves and Superlattices in Metallic Layered Transition-Metal Dichalcogenides. *Advances in Physics* **1975**, *24*, 117–201.

(8) Brown, S.; Gruner, G. Charge and Spin-Density Waves. *Scientific American* **1994**, *270*, 50–56.

(9) Goli, P.; Khan, J.; Wickramaratne, D.; Lake, R. K.; Balandin, A. A. Charge Density Waves in Exfoliated Films of van der Waals Materials: Evolution of Raman Spectrum in $TiSe_2$. *Nano Letters* **2012**, *12*, 5941–5945.

(10) Calandra, M.; Mazin, I. I.; Mauri, F. Effect of dimensionality on the charge-density wave in few-layer 2H-$NbSe_2$. *Phys. Rev. B: Condens. Matter Mater. Phys.* **2009**, *80*, 241108/1–241108/4.

(11) Levy, F.; Berger, H. Single-Crystals of Transition-Metal Trichalcogenides. *Journal of Crystal Growth* **1983**, *61*, 61–68.

(12) Thorne, R. E. Effect of Crystal-Growth Conditions on Charge-Density-Wave Pinning in $NbSe_3$. *Physical Review B* **1992**, *45*, 5804–5810.

(13) Naik, I.; Rastogi, A. K. Charge density wave and superconductivity in 2H- and 4H-$NbSe_2$: A revisit. *Pramana-Journal of Physics* **2011**, *76*, 957–963.

(14) Patel, A. J.; Bhayani, M. K.; Jani, A. R. Growth and Surface Microtopography of 2H-TaS_xSe_{2-x} Single Crystals. *Chalcogenide Letters* **2009**, *6*, 491–502.

(15) Zybtsev, S. G.; Pokrovskii, V. Y.; Nasretdinova, V. F.; Zaitsev-Zotov, S. V. Gigahertz-range synchronization at room temperature and other features of charge-density wave transport in the quasi-one-dimensional conductor NbS_3. *Applied Physics Letters* **2009**, *94*.

(16) Schuffenhauer, C.; Parkinson, B. A.; Jin-Phillipp, N. Y.; Joly-Pottuz, L.; Martin, J. M.; Popovitz-Biro, R.; Tenne, R. Synthesis of fullerene-like tantalum disulfide nanoparticles by a gas-phase reaction and laser ablation. *Small* **2005**, *1*, 1100–1109.

(17) Kikkawa, S.; Ogawa, N.; Koizumi, M.; Onuki, Y. High-Pressure Syntheses of TaS_3, NbS_3, $TaSe_3$, and $NbSe_3$ with $NbSe_3$-Type Crystal-Structure. *Journal of Solid State Chemistry* **1982**, *41*, 315–322.

(18) Stender, C. L.; Sekar, P.; Odom, T. W. Solid-state chemistry on a surface and in a beaker: Unconventional routes to transition metal chalcogenide nanomaterials. *Journal of Solid State Chemistry* **2008**, *181*, 1621–1627.

(19) Ueno, K.; Saiki, K.; Shimada, T.; Koma, A. Epitaxial-Growth of Transition-Metal Dichalcogenides on Cleaved Faces of Mica. *Journal of Vacuum Science & Technology A: Vacuum, Surfaces, and Films* **1990**, *8*, 68–72.

(20) Colletti, L. P.; Teklay, D.; Stickney, J. L. Thin-Layer Electrochemical Studies of the Oxidative Underpotential Deposition of Sulfur and Its Application to the Electrochemical Atomic Layer Epitaxy Deposition of CdS. *Journal of Electroanalytical Chemistry* **1994**, *369*, 145–152.

(21) Gebregziabiher, D. K.; Ledina, M. A.; Preisser, R.; Stickney, J. L. Cu(111) Surface Passivation with Atomic Layers of Te, Se or I, Studied Using Auger Spectrscopy. *Journal of the Electrochemical Society* **2012**, *159*, H675–H679.

(22) Gregory, B. W.; Norton, M. L.; Stickney, J. L. Thin-Layer Electrochemical Studies of the Underpotential Deposition of Cadmium and Tellurium on Polycrystalline Au, Pt and Cu Electrodes. *Journal of Electroanalytical Chemistry* **1990**, *293*, 85–101.

(23) Sorenson, T. A.; Varazo, K.; Suggs, D. W.; Stickney, J. L. Formation of and phase transitions in electrodeposited tellurium atomic layers on Au(111). *Surface Science* **2001**, *470*, 197–214.

(24) Suggs, D. W.; Stickney, J. L. Characterization of Atomic Layers of Tellurium Electrodeposited on the Low-Index Planes of Gold. *Journal of Physical Chemistry* **1991**, *95*, 10056–10064.

(25) Seim, H. J.; Holt, M. L. Attempts to Electrodeposit Tantalum. *Journal of the Electrochemical Society* **1949**, *96*, 43–47.

(26) Bayot, D.; Devillers, M. Peroxo complexes of niobium(V) and tantalum(V). *Coordination Chemistry Reviews* **2006**, *250*, 2610–2626.

(27) Housecroft, C. E.; Sharpe, A. G., *Inorganic Chemistry*, Second; Prentice Hall: 2005, pp 654–658.

(28) Enghag, P. In *Encyclopedia of the Elements*; Wiley-VCH Verlag GmbH & Co. KGaA: 2004, pp 561–570.

(29) Pourbaix, M., *Atlas of Electrochemical Equilibria in Aqueous Solutions*; Pergamon: 1966.

(30) Radisic, A.; Oskam, G.; Searson, P. C. Influence of oxide thickness on nucleation and growth of copper on tantalum. *Journal of the Electrochemical Society* **2004**, *151*, C369–C374.

(31) Zheng, M.; Kelly, J. J.; Deligianni, H. Electrodeposition of Cu on Ta-based layers - I. Electrodeposition on Ta. *Journal of the Electrochemical Society* **2007**, *154*, D400–D405.

(32) Starosvetsky, D.; Sezin, N.; Ein-Eli, Y. Seedless copper electroplating on Ta from an alkaline activated bath. *Electrochim. Acta* **2012**, *82*, 367–371.

(33) Starosvetsky, D.; Sezin, N.; Ein-Eli, Y. Seedless copper electroplating on Ta from a "single" electrolytic bath. *Electrochimica Acta* **2010**, *55*, 1656–1663.

(34) Lide, D. R., *CRC Handbook of Chemistry and Physics, 88th Edition*; Journal of the American Chemical Society; CRC Press/Taylor & Francis Group: Boca Raton, FL, 2008.

(35) Bard, A. J.; Parsons, R.; Jordan, J.; Editors, *Standard Potentials in Aqueous Solution*; Marcel Dekker, Inc.: 1985, p 834.

(36) Nan, Z.; Xiang, H. A study of electrodes used in controlled-potential electrolysis of metal ions. *Talanta* **1990**, *37*, 677–81.

(37) Agulyansky, A. In *Chemistry of Tantalum and Niobium Fluoride Compounds*; Elsevier Science: Amsterdam, 2004, pp 125–134.

(38) Baumann, E. W. Investigation of Tantalum Fluoride System Using Fluoride-Selective Electrode. *Journal of Inorganic & Nuclear Chemistry* **1972**, *34*, 687–695.

(39) Varga, L. P.; Freund, H. Formation Constants of Tantalum Fluoride System. 2. Tantalum Electrode Potential Studies. *Journal of Physical Chemistry* **1962**, *66*, 187–189.

(40) Du, B.; Suni, I. I. Electrochemical dissolution of Ta and TaN diffusion barrier materials. *Electrochemical and Solid State Letters* **2005**, *8*, G283–G285.

(41) Sapra, S.; Li, H. Q.; Wang, Z. C.; Suni, I. I. Voltammetry and impedance studies of Ta in aqueous HF. *Journal of the Electrochemical Society* **2005**, *152*, B193–B197.

(42) Fairbrother, F.; Robinson, D.; Taylor, J. B. Some Water-Soluble Complexes of Pentavalent Niobium and Tantalum. *Journal of Inorganic & Nuclear Chemistry* **1958**, *8*, 296–301.

(43) Dengel, A. C.; Griffith, W. P. Studies on Transition-Metal Peroxo Complexes. 9. Carboxylato Peroxo Complexes of Niobium(V), Tantalum(V), Zirconium(IV) and Hafnium(IV). *Polyhedron* **1989**, *8*, 1371–1377.

(44) Li, A. D.; Kong, J. Z.; Zhai, H. F.; Cheng, J. B.; Li, H.; Wu, D. Synthesis, Characterization, and Applications of Water-Soluble Tantalum Carboxylate Precursors via a Flux Method. *Journal of the American Ceramic Society* **2009**, *92*, 1959–1965.

(45) Das, R. N.; Pramanik, P. Single step chemical synthesis of lead based relaxor ferroelectric niobate fine powders. *Nanostructured Materials* **1999**, *11*, 325–330.

(46) Panda, A. B.; Pathak, A.; Pramanik, P. Chemical synthesis of nanocrystalline strontium bismuth tantalate powders using tantalum-tartarate complex. *Journal of the American Ceramic Society* **2006**, *89*, 737–739.

(47) Sarkar, A.; Pramanik, P. A new and facile route to prepare mesoporous tantalum phosphate with high surface area using tantalum tartrate precursor. *Journal of Non-Crystalline Solids* **2010**, *356*, 2709–2713.

(48) Santibanez-Mendieta, A. B.; Fabbri, E.; Licoccia, S.; Traversa, E. Soft Chemistry Routes for the Synthesis of $Sr_{0.02}La_{0.98}Nb_{0.6}Ta_{0.4}O_4$ Proton Conductor. *Journal of the Electrochemical Society* **2011**, *158*, B1485–B1490.

(49) Gregory, B. W.; Stickney, J. L. Electrochemical Atomic Layer Epitaxy (ECALE). *Journal of Electroanalytical Chemistry* **1991**, *300*, 543–561.

(50) Gregory, B. W.; Suggs, D. W.; Stickney, J. L. Conditions for the Deposition of CdTe by Electrochemical Atomic Layer Epitaxy. *Journal of the Electrochemical Society* **1991**, *138*, 1279–1284.

(51) Latimer, W. M., *The Oxidation States of the Elements and Their Potentials in Aqueous Solutions. 2nd ed*; Prentice-Hall: 1952.

(52) Wang, Z. C.; Li, H. Q.; Shodiev, H.; Suniga, I. I. Immersion/electroless deposition of Cu on Ta. *Electrochemical and Solid State Letters* **2004**, *7*, C67–C69.

(53) Lay, M. D.; Stickney, J. L. EC-STM studies of Te and CdTe atomic layer formation from a basic Te solution. *Journal of the Electrochemical Society* **2004**, *151*, C431–C435.

(54) Peter, L. M. Electrochemical routes to earth-abundant photovoltaics: A minireview. *Electrochemistry Communications* **2015**, *50*, 88–92.

(55) Hossain, M. A.; Wang, M.; Choy, K.-L. Ecofriendly and Nonvacuum Electrostatic Spray-Assisted Vapor Deposition of Cu(In,Ga)(S,Se)$_2$ Thin Film Solar Cells. *ACS Applied Materials & Interfaces* **2015**, *7*, 22497–22503.

(56) Drayton, J. A.; Williams, D. D.; Geisthardt, R. M.; Cramer, C. L.; Williams, J. D.; Sites, J. R. Molybdenum oxide and molybdenum oxide-nitride back contacts for CdTe solar cells. *Journal of Vacuum Science & Technology A* **2015**, *33*.

(57) Zhou, F.; Zeng, F.; Liu, X.; Liu, F.; Song, N.; Yan, C.; Pu, A.; Park, J.; Sun, K.; Hao, X. Improvement of Jsc in a Cu_2ZnSnS_4 Solar Cell by Using a Thin Carbon Intermediate Layer at the Cu_2ZnSnS_4/Mo Interface. *ACS Applied Materials & Interfaces* **2015**, *7*, 22868–22873.

(58) Novoselov, K. S.; Geim, A. K.; Morozov, S. V.; Jiang, D.; Zhang, Y.; Dubonos, S. V.; Grigorieva, I. V.; Firsov, A. A. Electric field effect in atomically thin carbon films. *Science* **2004**, *306*, 666–669.

(59) Li, X. S.; Cai, W. W.; An, J. H.; Kim, S.; Nah, J.; Yang, D. X.; Piner, R.; Velamakanni, A.; Jung, I.; Tutuc, E.; Banerjee, S. K.; Colombo, L.; Ruoff, R. S. Large-Area Synthesis of High-Quality and Uniform Graphene Films on Copper Foils. *Science* **2009**, *324*, 1312–1314.

(60) Zhan, Y. J.; Liu, Z.; Najmaei, S.; Ajayan, P. M.; Lou, J. Large-Area Vapor-Phase Growth and Characterization of MoS_2 Atomic Layers on a SiO_2 Substrate. *Small* **2012**, *8*, 966–971.

(61) Chhowalla, M.; Shin, H. S.; Eda, G.; Li, L. J.; Loh, K. P.; Zhang, H. The chemistry of two-dimensional layered transition metal dichalcogenide nanosheets. *Nature Chemistry* **2013**, *5*, 263–275.

(62) Zhao, W. J.; Ribeiro, R. M.; Toh, M. L.; Carvalho, A.; Kloc, C.; Neto, A. H. C.; Eda, G. Origin of Indirect Optical Transitions in Few-Layer MoS_2, WS_2, and WSe_2. *Nano Letters* **2013**, *13*, 5627–5634.

(63) Mak, K. F.; Lee, C.; Hone, J.; Shan, J.; Heinz, T. F. Atomically Thin MoS_2: A New Direct-Gap Semiconductor. *Physical Review Letters* **2010**, *105*.

(64) Tongay, S.; Zhou, J.; Ataca, C.; Lo, K.; Matthews, T. S.; Li, J. B.; Grossman, J. C.; Wu, J. Q. Thermally Driven Crossover from Indirect toward Direct Bandgap in 2D Semiconductors: $MoSe_2$ versus MoS_2. *Nano Letters* **2012**, *12*, 5576–5580.

(65) Zhang, Y.; Chang, T. R.; Zhou, B.; Cui, Y. T.; Yan, H.; Liu, Z. K.; Schmitt, F.; Lee, J.; Moore, R.; Chen, Y. L.; Lin, H.; Jeng, H. T.; Mo, S. K.; Hussain, Z.; Bansil, A.; Shen, Z. X. Direct observation of the transition from indirect to direct bandgap in atomically thin epitaxial $MoSe_2$. *Nature Nanotechnology* **2014**, *9*, 111–115.

(66) Lopez-Sanchez, O.; Lembke, D.; Kayci, M.; Radenovic, A.; Kis, A. Ultrasensitive photodetectors based on monolayer MoS_2. *Nature Nanotechnology* **2013**, *8*, 497–501.

(67) Wang, X. L.; Gong, Y. J.; Shi, G.; Chow, W. L.; Keyshar, K.; Ye, G. L.; Vajtai, R.; Lou, J.; Liu, Z.; Ringe, E.; Tay, B. K.; Ajayan, P. M. Chemical Vapor Deposition Growth of Crystalline Monolayer $MoSe_2$. *ACS Nano* **2014**, *8*, 5125–5131.

(68) Saadi, F. H.; Carim, A. I.; Velazquez, J. M.; Baricuatro, J. H.; McCrory, C. C. L.; Soriaga, M. P.; Lewis, N. S. Operando Synthesis of Macroporous Molybdenum Diselenide Films for Electrocatalysis of the Hydrogen-Evolution Reaction. *ACS Catalysis* **2014**, *4*, 2866–2873.

(69) Wang, H. T.; Kong, D. S.; Johanes, P.; Cha, J. J.; Zheng, G. Y.; Yan, K.; Liu, N. A.; Cui, Y. $MoSe_2$ and WSe_2 Nanofilms with Vertically Aligned Molecular Layers on Curved and Rough Surfaces. *Nano Letters* **2013**, *13*, 3426–3433.

(70) Velazquez, J. M.; Saadi, F. H.; Pieterick, A. P.; Spurgeon, J. M.; Soriaga, M. P.; Brunschwig, B. S.; Lewis, N. S. Synthesis and hydrogen-evolution activity of tungsten selenide thin films deposited on tungsten foils. *Journal of Electroanalytical Chemistry* **2014**, *716*, 45–48.

(71) Velazquez, J. M.; John, J.; Esposito, D. V.; Pieterick, A.; Pala, R. A.; Sun, G.; Zhou, X.; Huang, Z.; Ardo, S.; Soriaga, M. P.; Brunschwig, B. S.; Lewis, N. A Scanning Probe Investigation of the Role of Surface Motifs in the Behavior of p-WSe_2 Photocathodes. *Energy & Environmental Science* **2015**.

(72) McKone, J. R.; Pieterick, A. P.; Gray, H. B.; Lewis, N. S. Hydrogen Evolution from Pt/Ru-Coated p-Type WSe_2 Photocathodes. *Journal of the American Chemical Society* **2013**, *135*, 223–231.

(73) Tributsch, H. Hole Reactions from d-Energy Bands of Layer Type Group VI Transition Metal Dichalcogenides: New Perspectives for Electrochemical Solar Energy Conversion. *Journal of the Electrochemical Society* **1978**, *125*, 1086–1093.

(74) Li, H.; Zhang, Q.; Yap, C. C. R.; Tay, B. K.; Edwin, T. H. T.; Olivier, A.; Baillargeat, D. From Bulk to Monolayer MoS_2: Evolution of Raman Scattering. *Advanced Functional Materials* **2012**, *22*, 1385–1390.

(75) Mann, J.; Ma, Q.; Odenthal, P. M.; Isarraraz, M.; Le, D.; Preciado, E.; Barroso, D.; Yamaguchi, K.; Palacio, G. V.; Nguyen, A.; Tran, T.; Wurch, M.; Nguyen, A.; Klee, V.; Bobek, S.; Sun, D. Z.; Heinz, T. F.; Rahman, T. S.; Kawakami, R.; Bartels, L. 2-Dimensional Transition Metal Dichalcogenides

with Tunable Direct Band Gaps: $MoS_{2(1-x)}Se_{2x}$ Monolayers. *Advanced Materials* **2014**, *26*, 1399–1404.

(76) Li, H. L.; Duan, X. D.; Wu, X. P.; Zhuang, X. J.; Zhou, H.; Zhang, Q. L.; Zhu, X. L.; Hu, W.; Ren, P. Y.; Guo, P. F.; Ma, L.; Fan, X. P.; Wang, X. X.; Xu, J. Y.; Pan, A. L.; Duan, X. F. Growth of Alloy $MoS_{2x}Se_{2(1-x)}$ Nanosheets with Fully Tunable Chemical Compositions and Optical Properties. *Journal of the American Chemical Society* **2014**, *136*, 3756–3759.

(77) Li, M. Y.; Shi, Y. M.; Cheng, C. C.; Lu, L. S.; Lin, Y. C.; Tang, H. L.; Tsai, M. L.; Chu, C. W.; Wei, K. H.; He, J. H.; Chang, W. H.; Suenaga, K.; Li, L. J. Epitaxial growth of a monolayer WSe_2-MoS_2 lateral p-n junction with an atomically sharp interface. *Science* **2015**, *349*, 524–528.

(78) Gong, Y. J.; Liu, Z.; Lupini, A. R.; Shi, G.; Lin, J. H.; Najmaei, S.; Lin, Z.; Elias, A. L.; Berkdemir, A.; You, G.; Terrones, H.; Terrones, M.; Vajtai, R.; Pantelides, S. T.; Pennycook, S. J.; Lou, J.; Zhou, W.; Ajayan, P. M. Band Gap Engineering and Layer-by-Layer Mapping of Selenium-Doped Molybdenum Disulfide. *Nano Letters* **2014**, *14*, 442–449.

(79) Gong, Y. J.; Lin, J. H.; Wang, X. L.; Shi, G.; Lei, S. D.; Lin, Z.; Zou, X. L.; Ye, G. L.; Vajtai, R.; Yakobson, B. I.; Terrones, H.; Terrones, M.; Tay, B. K.; Lou, J.; Pantelides, S. T.; Liu, Z.; Zhou, W.; Ajayan, P. M. Vertical and in-plane heterostructures from WS_2/MoS_2 monolayers. *Nature Materials* **2014**, *13*, 1135–1142.

(80) Fang, H.; Battaglia, C.; Carraro, C.; Nemsak, S.; Ozdol, B.; Kang, J. S.; Bechtel, H. A.; Desai, S. B.; Kronast, F.; Unal, A. A.; Conti, G.; Conlon, C.; Palsson, G. K.; Martin, M. C.; Minor, A. M.; Fadley, C. S.; Yablonovitch,

E.; Maboudian, R.; Javey, A. Strong interlayer coupling in van der Waals heterostructures built from single-layer chalcogenides. *Proceedings of the National Academy of Sciences of the United States of America* **2014**, *111*, 6198–6202.

(81) Huang, C. M.; Wu, S. F.; Sanchez, A. M.; Peters, J. J. P.; Beanland, R.; Ross, J. S.; Rivera, P.; Yao, W.; Cobden, D. H.; Xu, X. D. Lateral heterojunctions within monolayer $MoSe_2-WSe_2$ semiconductors. *Nature Materials* **2014**, *13*, 1096–1101.

(82) Lee, Y. H.; Zhang, X. Q.; Zhang, W. J.; Chang, M. T.; Lin, C. T.; Chang, K. D.; Yu, Y. C.; Wang, J. T. W.; Chang, C. S.; Li, L. J.; Lin, T. W. Synthesis of Large-Area MoS_2 Atomic Layers with Chemical Vapor Deposition. *Advanced Materials* **2012**, *24*, 2320–2325.

(83) Van der Zande, A. M.; Huang, P. Y.; Chenet, D. A.; Berkelbach, T. C.; You, Y. M.; Lee, G. H.; Heinz, T. F.; Reichman, D. R.; Muller, D. A.; Hone, J. C. Grains and grain boundaries in highly crystalline monolayer molybdenum disulphide. *Nature Materials* **2013**, *12*, 554–561.

(84) Ling, X.; Lee, Y. H.; Lin, Y. X.; Fang, W. J.; Yu, L. L.; Dresselhaus, M. S.; Kong, J. Role of the Seeding Promoter in MoS_2 Growth by Chemical Vapor Deposition. *Nano Letters* **2014**, *14*, 464–472.

(85) Splendiani, A.; Sun, L.; Zhang, Y. B.; Li, T. S.; Kim, J.; Chim, C. Y.; Galli, G.; Wang, F. Emerging Photoluminescence in Monolayer MoS_2. *Nano Letters* **2010**, *10*, 1271–1275.

(86) Duan, X. D.; Wang, C.; Shaw, J. C.; Cheng, R.; Chen, Y.; Li, H. L.; Wu, X. P.; Tang, Y.; Zhang, Q. L.; Pan, A. L.; Jiang, J. H.; Yu, R. Q.; Huang, Y.; Duan, X. F. Lateral epitaxial growth of two-dimensional layered semiconductor heterojunctions. *Nature Nanotechnology* **2014**, *9*, 1024–1030.

(87) Najmaei, S.; Liu, Z.; Zhou, W.; Zou, X. L.; Shi, G.; Lei, S. D.; Yakobson, B. I.; Idrobo, J. C.; Ajayan, P. M.; Lou, J. Vapour phase growth and grain boundary structure of molybdenum disulphide atomic layers. *Nature Materials* **2013**, *12*, 754–759.

(88) Shaw, J. C.; Zhou, H. L.; Chen, Y.; Weiss, N. O.; Liu, Y.; Huang, Y.; Duan, X. F. Chemical vapor deposition growth of monolayer $MoSe_2$ nanosheets. *Nano Research* **2014**, *7*, 511–517.

(89) Elias, A. L.; Perea-Lopez, N.; Castro-Beltran, A.; Berkdemir, A.; Lv, R. T.; Feng, S. M.; Long, A. D.; Hayashi, T.; Kim, Y. A.; Endo, M.; Gutierrez, H. R.; Pradhan, N. R.; Balicas, L.; Houk, T. E. M.; Lopez-Urias, F.; Terrones, H.; Terrones, M. Controlled Synthesis and Transfer of Large-Area WS_2 Sheets: From Single Layer to Few Layers. *ACS Nano* **2013**, *7*, 5235–5242.

(90) Zach, M. P.; Ng, K. H.; Penner, R. M. Molybdenum nanowires by electrodeposition. *Science* **2000**, *290*, 2120–2123.

(91) Zach, M. P.; Inazu, K.; Ng, K. H.; Hemminger, J. C.; Penner, R. M. Synthesis of molybdenum nanowires with millimeter-scale lengths using electrochemical step edge decoration. *Chemistry of Materials* **2002**, *14*, 3206–3216.

(92) Li, Q.; Walter, E. C.; van der Veer, W. E.; Murray, B. J.; Newberg, J. T.; Bohannan, E. W.; Switzer, J. A.; Hemminger, J. C.; Penner, R. M. Molybdenum disulfide nanowires and nanoribbons by electrochemical/chemical synthesis. *Journal of Physical Chemistry B* **2005**, *109*, 3169–3182.

(93) Enghag, P. In *Encyclopedia of the Elements*; Wiley-VCH Verlag GmbH & Co. KGaA: 2007, pp 589–604.

(94) Morley, T. J.; Penner, L.; Schaffer, P.; Ruth, T. J.; Benard, F.; Asselin, E. The deposition of smooth metallic molybdenum from aqueous electrolytes

containing molybdate ions. *Electrochemistry Communications* **2012**, *15*, 78–80.

(95) Syed, R.; Ghosh, S. K.; Sastry, P. U.; Sharma, G.; Hubli, R.; Chakravartty, J. K. Electrodeposition of thick metallic amorphous molybdenum coating from aqueous electrolyte. *Surface & Coatings Technology* **2015**, *261*, 15–20.

(96) Elezovic, N. R.; Jovic, V. D.; Krstajic, N. V. Kinetics of the hydrogen evolution reaction on Fe-Mo film deposited on mild steel support in alkaline solution. *Electrochimica Acta* **2005**, *50*, 5594–5601.

(97) Pellicer, E.; Gomez, E.; Valles, E. Use of the reverse pulse plating method to improve the properties of cobalt-molybdenum electrodeposits. *Surface & Coatings Technology* **2006**, *201*, 2351–2357.

(98) Anand, T. J. S.; Sanjeeviraja, C.; Jayachandran, M. Preparation of layered semiconductor ($MoSe_2$) by electrosynthesis. *Vacuum* **2001**, *60*, 431–435.

(99) Chandra, S.; Sahu, S. N. Electrodeposited semiconducting molybdenum selenide films. I. Preparatory technique and structural characterisation. *Journal of Physics D: Applied Physics* **1984**, *17*, 2115.

(100) Delphine, S. M.; Jayachandran, M.; Sanjeeviraja, C. Pulsed electrodeposition and characterization of molybdenum diselenide thin film. *Materials Research Bulletin* **2005**, *40*, 135–147.

(101) Hankare, P. P.; Chate, P. A.; Delekar, S. D.; Bhuse, V. M.; Asabe, M. R.; Jadhav, B. V.; Garadkar, K. M. Structural and opto-electrical properties of molybdenum diselenide thin films deposited by chemical bath method. *Journal of Crystal Growth* **2006**, *291*, 40–44.

Chapter 2

Ta Surface Chemistry in Aqueous Solutions and the Possible Formation of $TaTe_2$ and TaS_3[1]

[1]Tsang, C.; Kim, Y. G.; Gebregziabiher, D.; Stickney, J. Ta Surface Chemistry in Aqueous Solutions and the Possible Formation of $TaTe_2$ and TaS_3. *Journal of the Electrochemical Society* **2013**, *160*, D3278–D3284.

2.1 Abstract

This report discusses the reductive removal of Ta oxide electrochemically using cyclic voltammetry (CV), in-situ electrochemical scanning tunneling microscopy (EC-STM), and X-ray photoelectron spectroscopy (XPS). From CVs, it was shown that the longer a Ta electrode was maintained at potentials negative of −1.5 V, the more surface oxide that was reduced, as evidenced by increases in hydrogen evolution. Atomically-resolved EC-STM images were obtained after reduction at −1.8 V. The efficacy of Te at passivating Ta surfaces was investigated and found to work well, from EC-STM, CVs and XPS. S and Cu were also deposited onto Ta following an oxide reduction step. EC-STM images of the Ta surface in $HTeO_2^+$ and Na_2S solutions suggested the formation of $TaTe_2$ and TaS_3, respectively, on the surface.

2.2 Introduction

Tantalum is a refractory metal that forms a stable surface oxide layer, Ta_2O_5, when exposed to ambient conditions. The native oxide formed in air is about 2–3 nm thick.[1–3] This passivating oxide is resistant to most commonly-known acids and bases,[4–6] making further reactions with the underlying metallic tantalum difficult. Owing to its passive oxide layer, tantalum has special importance in applications such as liners for corrosion- and heat-resistant equipment, capacitors, and biomedical uses.[6,7]

The presence of the oxide layer on Ta is not always desirable. In the copper damascene process for interconnect technologies, Ta is typically used as a diffusion barrier layer between Cu and silicon dioxide or the low-k interlayer dielectric.[8,9] Deposition of Cu onto the Ta barrier is heavily influenced by the oxide layer. Historically a Cu seed layer is first deposited by physical vapor deposition (PVD) on the oxide, before the electrochemical fill step. The seed layer should be a conformal homogeneous layer

of Cu a few atomic layers thick. However since the Cu seed deposits by nucleation and growth on the Ta oxide, it is not homogeneous or conformal and is much thicker than desired as the dimensions of vias continue to decrease. If Cu could be electrodeposited directly on the Ta barrier metal, not the oxide, a seed layer might not be necessary. Removing the Ta oxide would be the first step to realizing this advance.[10–13].

TaX_n (X = S, Se, or Te; $n = 2$ or 3) are transition metal chalcogenides (TMCs) that possess layered ($n = 2$) or chain-like ($n = 3$) structures.[14,15] Similar to graphene in graphite, the highly-anisotropic TMCs are composed of layers or chains that interact through van der Waals gaps. Interesting phenomena such as charge-density waves (CDW) and superconductivity arise, at least partially, from the compound's anisotropy.[16] Recently there has been heightened interest in application of TMCs in electronic and optoelectronic devices.[17,18] Attention has focused particularly on 2D nanosheets of the TMCs, which may exhibit properties different from the corresponding bulk materials. Recent experimental and theoretical works have indicated that thin films of transition metal chalcogenides can exhibit CDW transition temperatures higher than those of their bulk counterparts.[19,20] High-quality TMCs have traditionally been grown using chemical vapor transport (CVT),[21–23] which requires high temperatures for a week. The need for thin film CDW materials has motivated attempts at growing TMCs by alternative bottom-up methods, possibly by electrochemical atomic layer deposition (E-ALD).[24–27]

The present study is a first step in determining if E-ALD can be used to grow transition metal (valve metals: Ta, Nb and Ti) chalcogenide (S, Se and Te) films at room temperature. Atomic Layer Deposition (ALD) is a deposition method based on the use of surface-limited reactions to form deposits one atomic layer at a time. Electrochemical surface limited reactions are referred to as underpotential deposits (UPD).[28–30] UPD is where the first atomic layer deposits at a potential prior to, under, that needed to deposit the element on itself. In E-ALD atomic layers of the elements

are deposited alternately on each other, in a cycle. The more cycles performed the thicker the deposit. To develop an E-ALD cycle for the deposition of a compound, the electrochemical behavior of the participating elements on each other should first be investigated. This is a study of the electrochemical surface chemistry of Te and S on Ta, as a precursor to designing a cycle for the formation of $TaTe_n$ and TaS_n ($n = 2$ or 3) using E-ALD. It is also a precursor to development of a seedless process for Cu on Ta.

The stable Ta_2O_5 is an n-type semiconductor with a band gap of about about 4 eV,[31,32] and its standard reduction potential is -0.75 V vs. SHE.[33] To follow the state of the surface under electrochemical reduction, cyclic voltammetry (CV), electrochemical scanning tunneling microscopy (EC-STM) and X-ray Photoelectron Spectroscopy (XPS) measurements were performed. In addition, the deposition of Te, S, or Cu on the reduced Ta surfaces was performed.

2.3 Experimental

All potentials were reported vs. a Ag/AgCl (3 M KCl) reference electrode (Bioanalytical Systems, Inc.). The Ta foils were purchased from Alfa Aesar, 99.95 %, and were 0.5 mm thick. Ta/Au/glass substrates were made by in-house by e-beam evaporation of Ta (Kurt J. Lesker, 99.95 %) onto commercial Au/glass (EMF Corp) substrates. The Au/glass substrates had a 100 nm Au layer and a 5 nm Ti adhesion layer, between the Au and glass. The e-beam deposited Ta layer was ∼100 nm thick. All solutions were prepared with 18 MΩ H_2O from a Milli-Q purification system. The following reagents were used: $NaClO_4$ (Fisher Scientific, HPLC grade), $NaHCO_3$ (J.T. Baker), KOH (J.T. Baker), NaOH (Fisher Scientific, 98.9 %), $KClO_4$ (Sigma-Aldrich, 99.99+ %), TeO_2 (Alfa Aesar, 99.995 %), Na_2S (Sigma-Aldrich, 99.99+ %), $Cu(ClO_4)_2$ (Sigma-Aldrich, 98 %).

A Nanoscope III (Digital Instruments, Santa Barbara, CA) was used with a custom built in-situ EC-STM cell. This cell used a Au wire auxiliary electrode and a commercial 3 M Ag/AgCl reference electrode (BAS). All EC-STM images were obtained using W tips partially coated with nail polish. STM dimensions were calibrated using HOPG, (0.25 ± 0.01) nm. XPS studies were carried out using a Mg K$\alpha_{1,2}$ (STAIB) X-ray source, at $\sim$70° to hemispherical analyzer axes (Leybold Heraeus).

2.4 Results and Discussion

2.4.1 Ta oxide reduction study

The redox behavior of a Ta foil electrode was initially studied using cyclic voltammetry (CV). The inset of Figure 2.1 shows a CV cycle of the Ta electrode in 1.78 M KOH over the potential range of -1.6 V and -0.2 V. Two points are observed where the currents of the forward and reverse scans cross, at -1.48 V and -0.55 V. It is proposed that the bulk of the charge passed negative of -0.6 V is due to the hydrogen evolution reaction (HER), while positive of -0.2 V the current is primarily Ta oxide formation. Kinetics for both of these electrochemical reactions are significantly affected by the oxide thickness on the working electrode.[32] For a given applied potential, part of the potential will be dropped across the oxide layer, with an increasing fraction as the oxide thickens, reducing the driving force.[10,34] It is assumed that some of the negative potential applied to the Ta electrode is dropped by the presence of an oxide, so that the potential at the oxide-solution interface will be lowered. The thicker the oxide layer, the less negative the potential will be, and the lower the HER rate.[35] From the inset of Figure 2.1, it is evident that there is more HER scanning positive, than there was during the initial negative-going scan. This suggests some loss of oxide at the most negative potentials, near -1.6 V. Scans were performed with the Ta electrode to various positive potential limits. Figure 2.1 displays the subsequent HER currents near -1.6 V, after reversing the previous scan at the indicated potentials. When the

potential was scanned to −420 mV twice, the second scan shows more HER current than the first scan, suggesting there was a net oxide removal, though the removal process was slow. As the positive potential limit was increased, the HER current decreased, indicating that more oxide was produced during the more positive portion of the scan, resulting in lower HER currents at the more negative scan potentials. If the potential was kept below −0.42 V, no significant oxide increase occurred in the positive part of the scan, and during the subsequent cycle, still more oxide reduced at −1.6 V, as evidenced by the increase in HER. For reference, the theoretical potential (vs. 3 M Ag/AgCl) for oxidation of Ta to Ta_2O_5 is given by[33]

$$E\,(\mathrm{V}) = -0.960 - 0.059 \cdot \mathrm{pH} \tag{2.1}$$

Figure 2.2 shows EC-STM images of the Ta electrode surface while it was scanned between −1.3 V and −0.6 V in a 0.1 M $KClO_4$ electrolyte solution. E_{bias}, the tip potential relative to the working electrode, was 580 mV. The tip current, I_{tip}, was between −2 and −4 nA. The surface was first held at −1.0 V for 10 min to reduce Ta oxide prior to imaging. Patches showing a step-terraced surface, with 5 – 10 nm steps, were observed. Triangular pits, outlined in Figure 2.2b, were observed to grow during the scan. Atomic-level images of the surface were not obtained, presumably because the surface was not completely reduced. Atomically-resolved images are not expected if tantalum oxide were present on the polycrystalline Ta substrate. Tantalum oxide formed natively in air is multiple layers thick,[1–3] and Ta_2O_5 formed at low temperatures is known to be disordered and possibly amorphous.[36,37] Since tantalum oxide is an *n*-type semiconductor with a 4-eV bandgap, it can act as a barrier to electron tunneling, exponentially reducing the probability as the oxide thickens.[38] The potential was then held at −1.8 V for approximately 30 min, though due to extensive hydrogen evolution the potential was stepped to near −1 V for imaging. Atomically-resolved images were then observed (Figure 2.3). The surface appeared

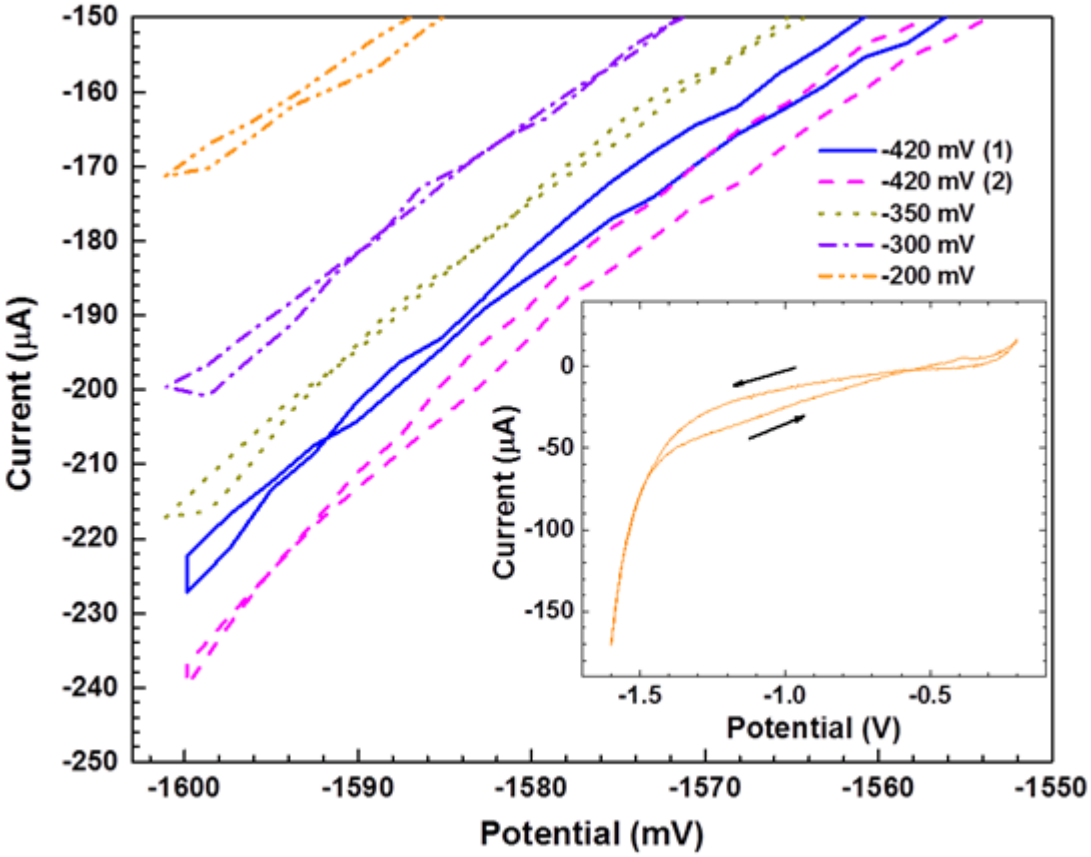

Figure 2.1: Ta foil in 1.78 M KOH. Scan rate: $10\,\mathrm{mV\,s^{-1}}$. Electrode area: $1.8\,\mathrm{cm^2}$.

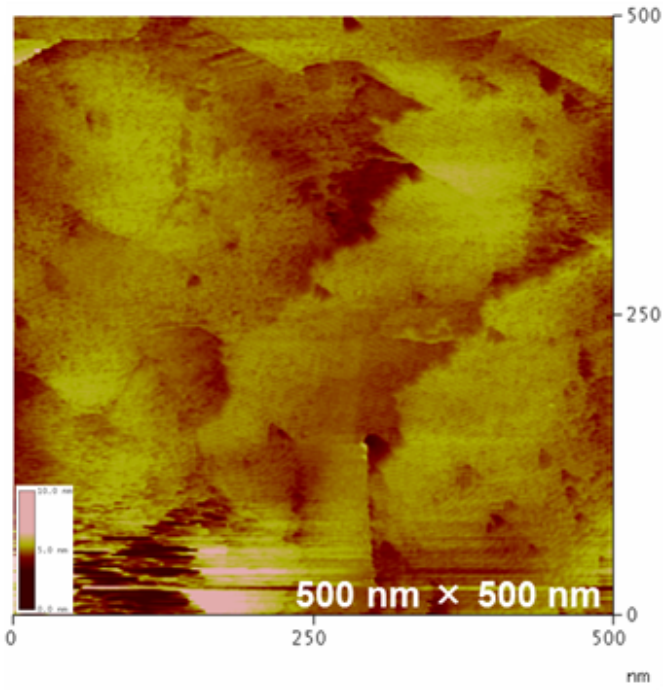

(a)

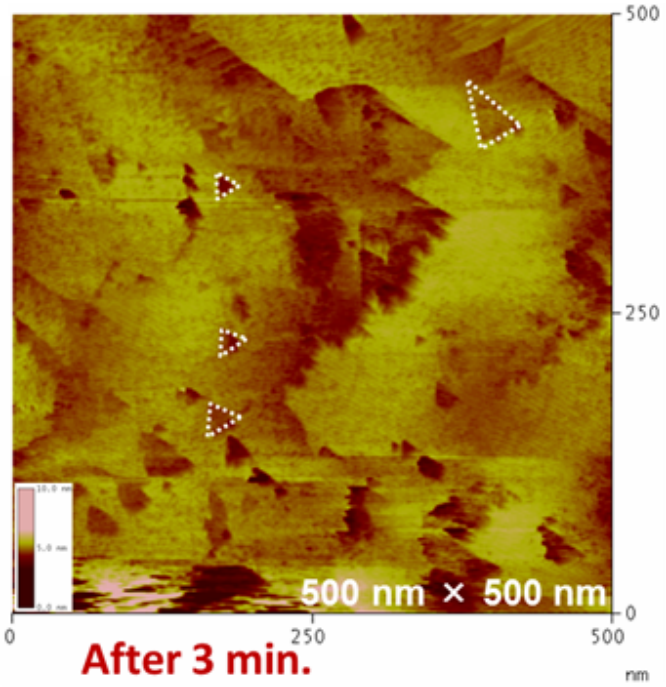

(b)

Figure 2.2: EC-STM images of Ta foil at between $-1.3\,\mathrm{V}$ and $-0.6\,\mathrm{V}$ after holding at $-1.0\,\mathrm{V}$ for oxide reduction. $0.1\,\mathrm{M}$ $KClO_4$ (pH $\sim$ 5) was used as the electrolyte. Triangular pits that grew during imaging are outlined in dashes in (b). The height scale at the bottom left of each image ranges from 0 to 10 nm. E_{bias} : 580 mV. (a) I_{tip} : $-2.14\,\mathrm{nA}$. (b) I_{tip} : $-3.67\,\mathrm{nA}$.

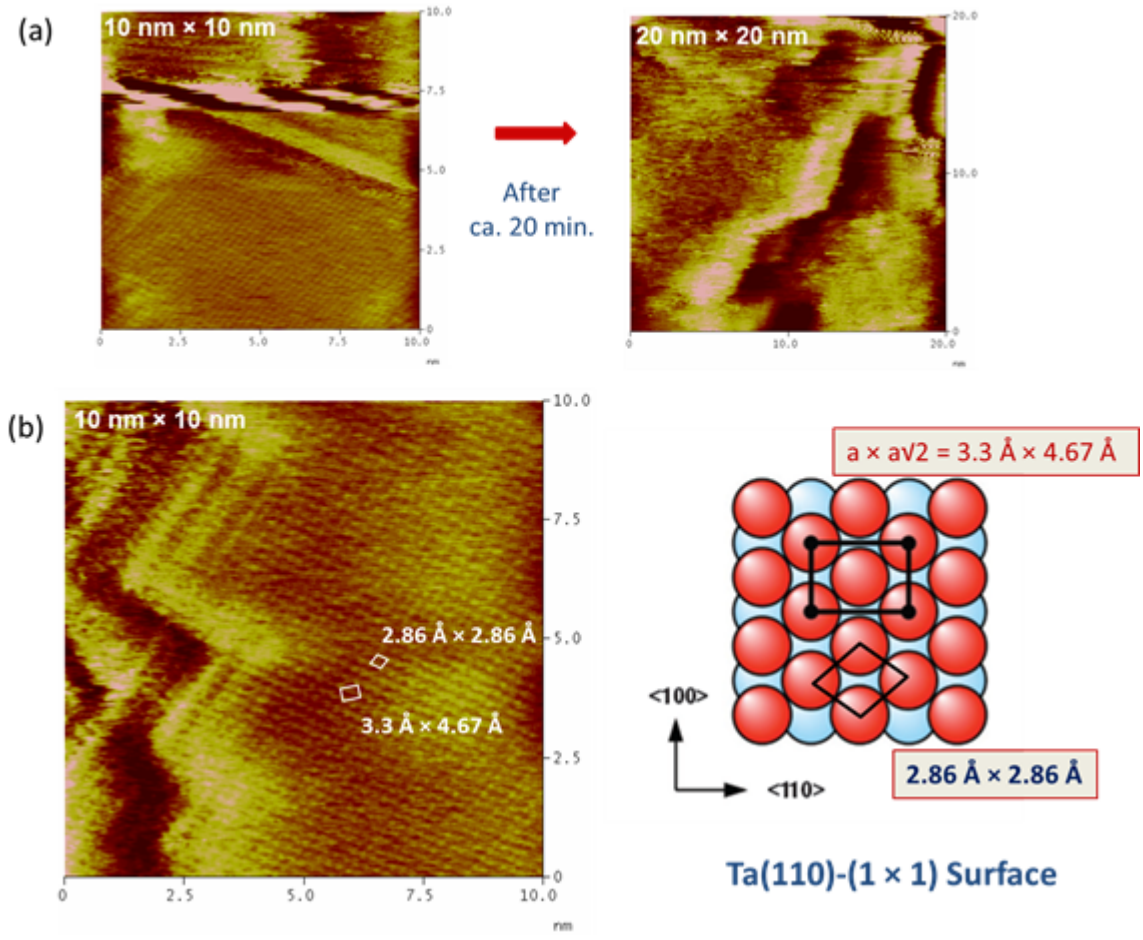

Figure 2.3: Ta foil in 1.78 M KOH. Scan rate: 10 mV s^{-1}. Electrode area: 1.8 cm^2.

to display a (1×1) structure on Ta(110) facets. The measured interatomic distance was (3.0 ± 0.2) Å, which is in good agreement with the expected value of 2.86 Å. After approximately 20 min, atomic resolution was lost, presumably because the surface was slowly re-oxidizing near -1 V. Attempts to obtain atomically-resolving images using a Ta(111) single crystal were unsuccessful, suggesting the overpotential needed for oxide reduction is facet-dependent and is greater for Ta(111) than for Ta(110). Such a difference would be consistent with reports that electrochemical reactions on polycrystalline Ta/Ta_2O_5 electrodes are spatially-localized, to certain electroactive sites.[1,32]

2.4.2 Characterization of Te deposition onto Ta by EC-STM

Te was investigated as a possible passivating agent for Ta, given its ability to passivate other metal surfaces such as Cu and Au, and because the electrochemistry of Te has been studied extensively by this group for 25 years.[39–42] Successful deposition of Te onto Ta is also relevant to the attempts by this group to form metal chalcogenides for CDW device fabrication. After reductive removal of the Ta oxide layer, Te was deposited at -1 V. After Te deposition, the solution was exchanged for 0.1 M $KClO_4$ blank for imaging. It is expected that any bulk Te present initially would be reduced to a soluble Te^{2-} species, leaving no more than an atomic layer of Te atoms on the surface. However, if $TaTe_2$ was formed, it might be more than one compound layer thick. The Ta surface was relatively easy to image after Te deposition, as can be seen from the atomically-resolved EC-STM images in Figure 2.4. The images were stable for substantially longer times and over a wider potential range, up to -0.3 V, compared to the Te-free surface. Both observations suggest the Te layer was electrodeposited onto a Ta surface and protected the Ta surface from oxidation.

A particularly interesting Te-covered surface structure at -0.5 V in 0.2 mM $HTeO_2^+$ solution is shown in Figure 2.5. The structure resembles a "double zigzag"

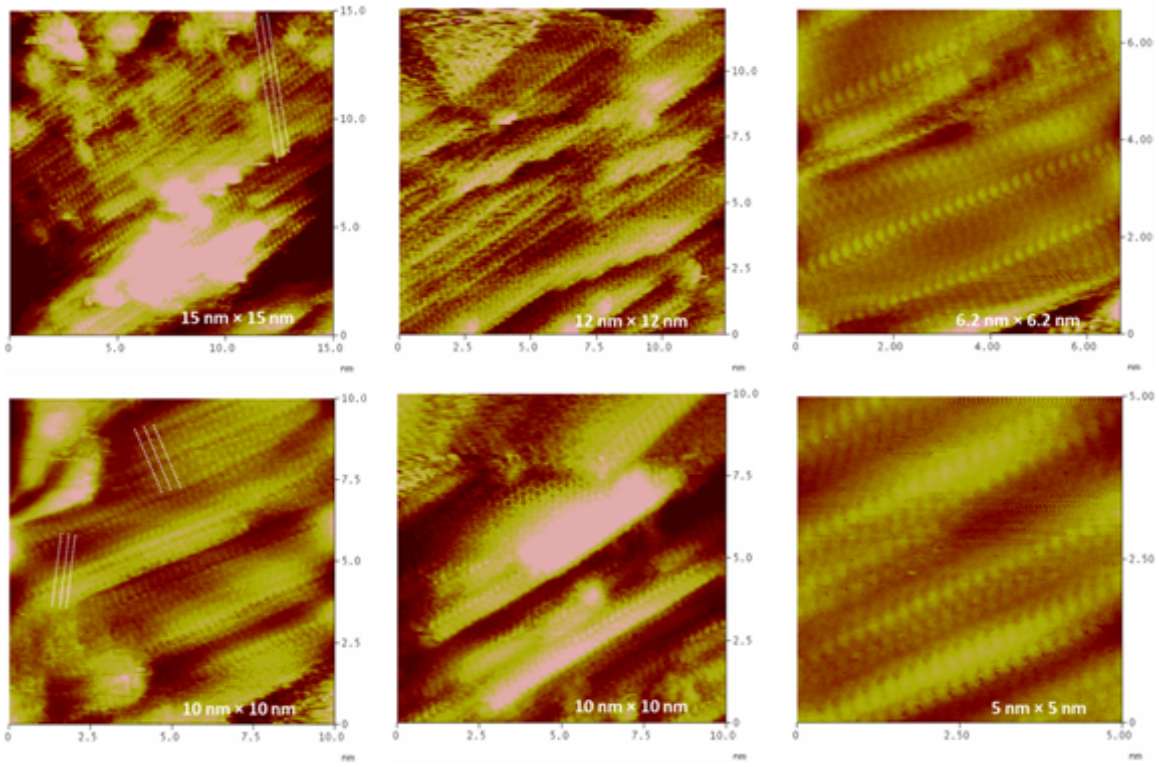

Figure 2.4: EC-STM images of various densely-packed bcc(hkl) surfaces of Te on Ta/Au/glass substrate. Te was deposited onto a Ta/Au/glass substrate at -1 V from a solution containing 0.2 mM $HTeO_2^+$ and 0.1 M $KClO_4$. Images were obtained in 0.1 M $KClO_4$. E_{bias} : 100 to 420 mV; I_{tip} : -9.95 to -36.2 nA.

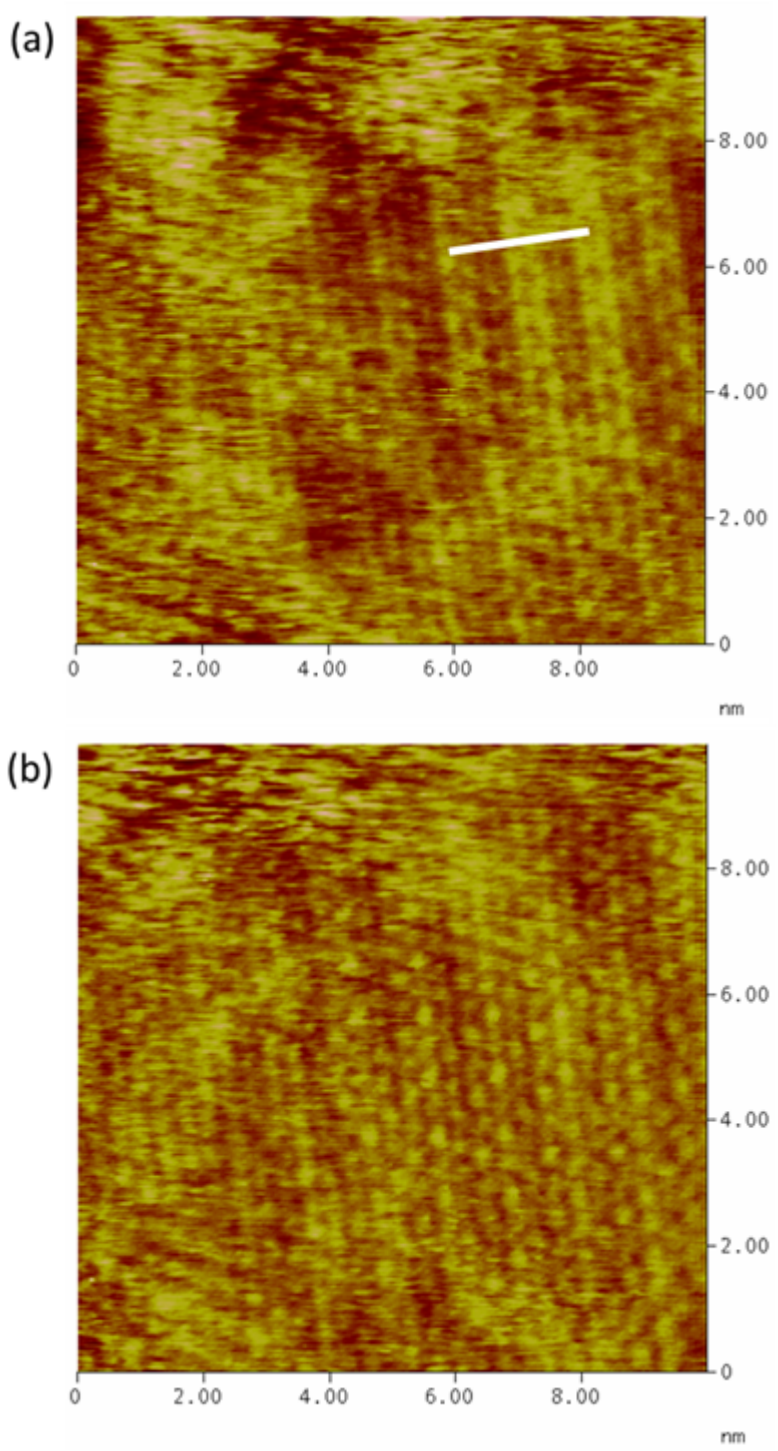

Figure 2.5: EC-STM images of a Te-covered Ta/Au/glass surface at $-0.5\,\mathrm{V}$ in a $0.2\,\mathrm{mM}$ $HTeO_2^+$ solution (pH $\sim$ 5). The atomic distance is $(0.33 \pm 0.02)\,\mathrm{nm}$. The distance indicated by the solid line in (a) is $\sim$22 Å. E_{bias} : $200\,\mathrm{mV}$; I_{tip} : (a) $-18\,\mathrm{nA}$ and (b) $-20\,\mathrm{nA}$.

pattern reported by Kim et al. for a 1T-$TaTe_2$ (001) surface, suggesting $TaTe_2$ formed on the electrode surface.[43] Kim used AFM to image the single crystal $TaTe_2$ surface and measured the unit cell parameters a and b to be (19.2 ± 0.2) Å and (3.6 ± 0.2) Å, respectively, which are in agreement with the crystallographic data published by Brown.[44] In this EC-STM study, the measured interatomic distance was 3.3 Å and the periodic distance in the direction perpendicular to the rows of Te atoms was about 22 Å as indicated in Figure 2.5. The measured distance appear consistent with the values reported by Kim and by Brown. If $TaTe_2$ was formed on the Ta electrode, the discrepancy with the measured distances might be microscope drift. If the Te is present as a single layer on the metallic Ta surface, different lattice constant would be expected relative to those for a $TaTe_2$ nanofilm. During imaging, some small particles appeared in the images, suggesting that some nm-sized flakes of $TaTe_2$ were present. The particles were very mobile, indicating that they were not strongly bound to the surface, as the tunneling process itself moved them, as would be expected for a van der Waals material like $TaTe_2$.

2.4.3 Characterization of Te deposition on Ta by CV and XPS

Cyclic voltammetry and X-ray photoelectron spectroscopy were also used to investigate deposition of Te on Ta electrodes and the possibility of passivating Ta with Te. CVs of a Ta foil in a pH 10.5 solution of TeO_2 are shown in Figure 2.6a. The potential was initially held at -0.9 V to promote oxide reduction and Te deposition. In the initial positive scan, significant oxidation was observed above -0.66 V (red). From the blank scan in Figure 2.6b (no TeO_2) similar oxidation current was only observed for the first positive scan (red). This initial oxidation is proposed to correspond to the irreversible oxidation of Ta or oxidation of an unstable surface layer of Ta, initially present.[32,45,46] On top of this irreversible oxidation current, bulk Te oxidation is observed starting at -0.15 V in Figure 2.6a. A comparison of the oxidation current

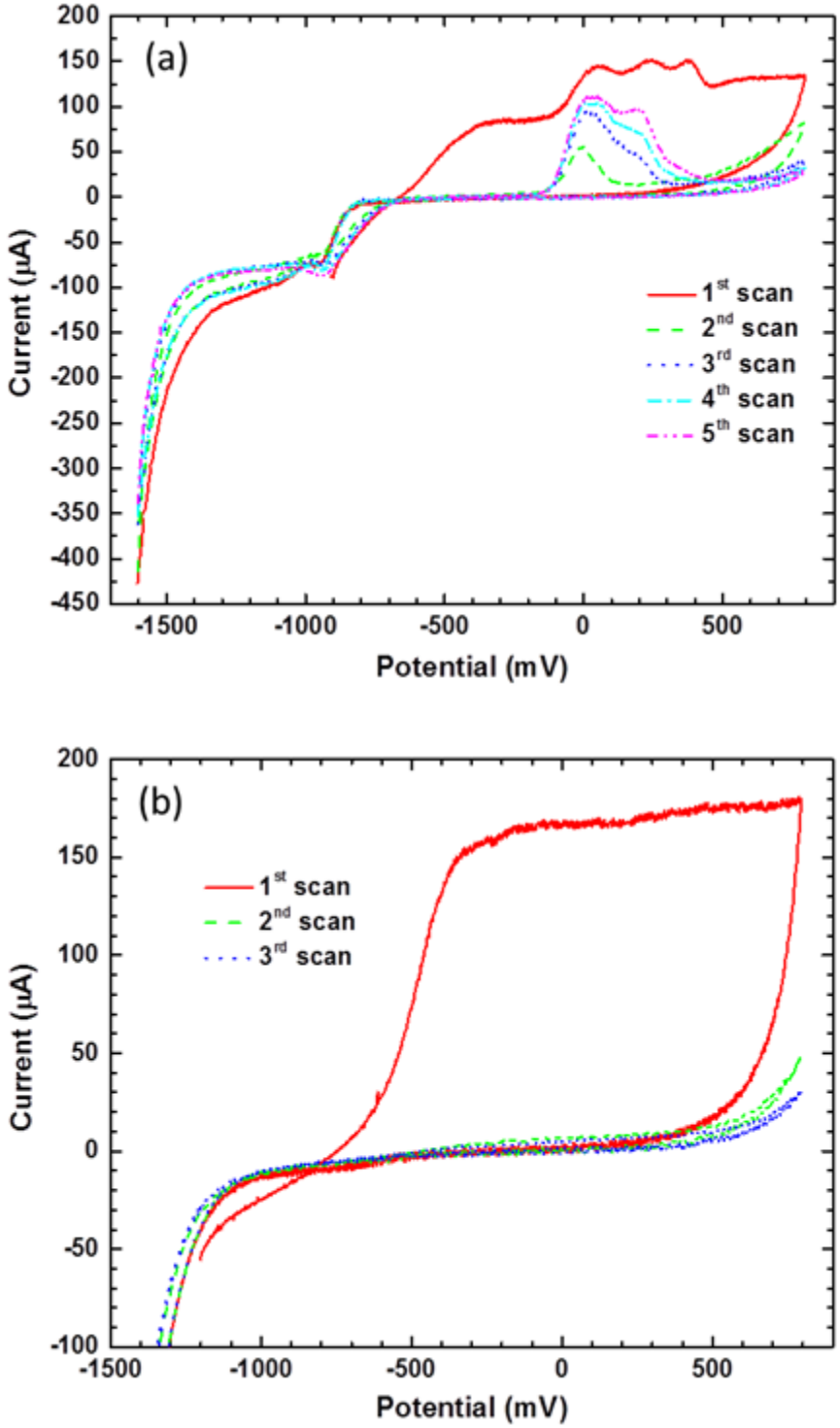

Figure 2.6: (a) CV of a polished Ta foil in 0.25 mM TeO_2 (pH 10.5). The potential was initially held at −0.9 V for 10 min before started scanning positive. (b) CV of a polished Ta foil in 0.1 M $NaClO_4$ blank (pH 10.5). The potential was initially held at −1.2 V for 10 min before started scanning positive.

negative of −0.1 V in Figure 2.6a (red solid) with that in Figure 2.6b (red solid) suggests that adsorbed Te may have suppressed some of the Ta oxidation. Between −0.1 and 0.5 V in Figure 2.6a two or three peaks for Te oxidation are evident. The second cycle (green dash), however, shows only one. Subsequent cycles show increases in the first peak and growth of a second. A reduction feature between −0.7 V and −1.0 V corresponds to the initial deposition of Te. The lack of voltammetric features for Te between −0.2 V and −0.8 V is characteristic of the well known irreversibility of Te deposition.

A Ta/Au/glass electrode was first cleaned by cold Ar^+ ion bombardment in the UHV chamber, and then transferred to an UHV antechamber equipped with an electrochemical cell. The open-circuit potential (OCP) of this sample in a pH 10 TeO_2 solution was −0.85 V. Te was deposited by scanning the potential negative from the OCP and cycling between −1.6 V and −0.4 V three times, followed by a 1-min hold at −1.6 V. The sample was then transferred back to the UHV analysis chamber for XPS analysis. Figure 2.7 shows XPS spectra for Ta, O, and Te. Spectra of Ta and O before and after Te deposition are shown for comparison. While the intensities of the oxidized Ta peaks remain relatively unchanged, the metallic Ta peak intensities drop dramatically, most likely due to oxidation of metallic Ta near the surface. However, the O signal intensity was relatively unchanged, possibly indicating that some metallic tantalum instead reacted with Te, which protected the Ta from oxidation during transfer from the ante chamber (in wet UHP Ar gas) into the analysis chamber at UHV. For 1T-$TaTe_2$, the expected binding energies of the Ta $4f_{7/2}$ and $4f_{5/2}$ peaks are 22.4 and 24.3 eV, respectively.[47] That no clearly resolved peaks are evident for this shift probably results from it being a minority species, with respect to the multiple layers of oxide present.

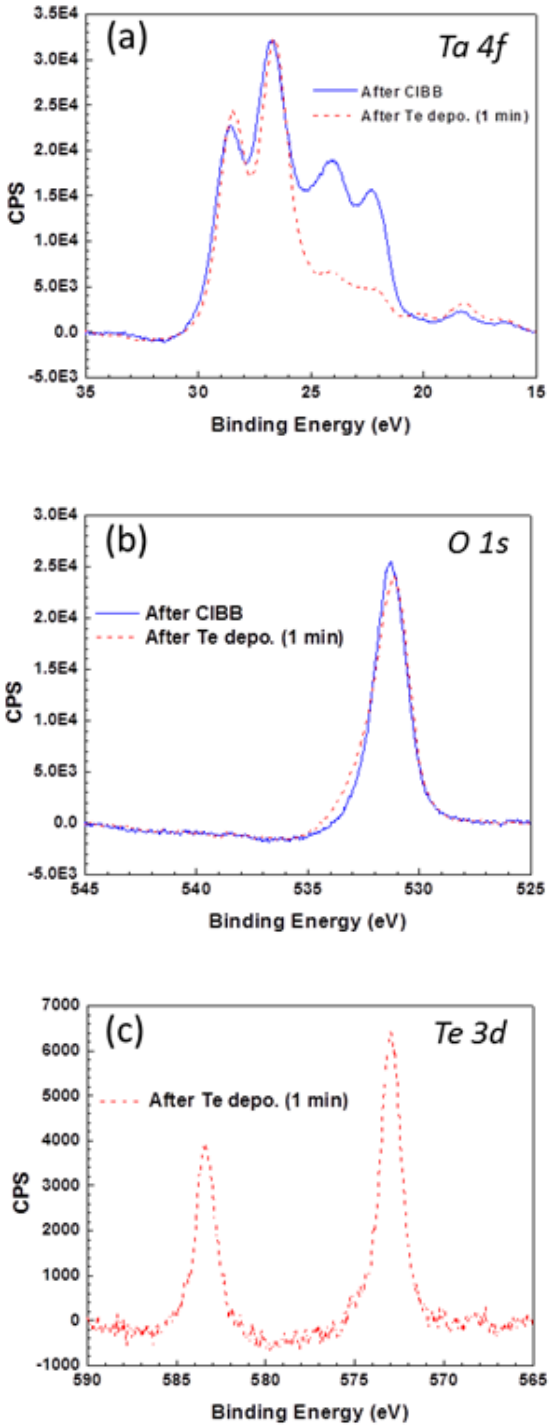

Figure 2.7: XPS spectra of Ta/Au/glass electrode before and after Te deposition. Te was deposited in a solution containing 0.25 mM TeO_2, 18 mM NaOH and 20 mM $NaHCO_3$. Prior to Te deposition, the electrode was cleaned by cold ion bombardment (CIBB). The photoelectric peaks correspond to (a) Ta 4f, (b) O 1s, and (c) Te 3d as indicated in the respective spectra.

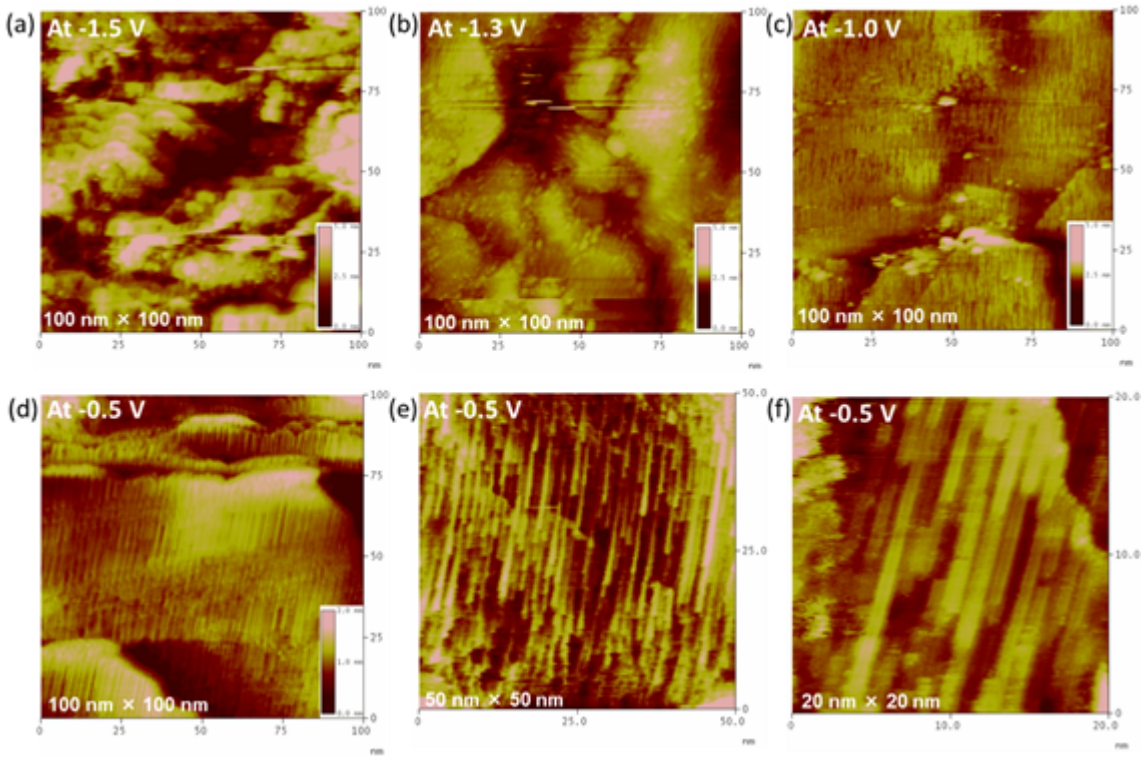

Figure 2.8: EC-STM images of Ta/Au/glass electrode surface in a 2 mM Na_2S solution at (a) −1.5 V, (b) −1.3 V, (c) −1.0 V, and (d-f) −0.5 V. The height scale ranges from 0 to 5 nm for (a) to (c) and from 0 to 2 nm for (d). E_{bias} : 300 to 500 mV; I_{tip} : −10 to −66 nA.

2.4.4 Characterization of Ta surface exposed to S and Cu deposition by EC-STM

While sulfur adsorption is pertinent to the formation of tantalum sulfide for CDW applications, sulfur and copper are important in the damascene process in ULSI. In this report S and Cu were studied separately on Ta surfaces. Similar to the EC-STM study of Te on Ta, described above, a Ta/Au/glass electrode was electrochemically reduced at $-1.8\,\mathrm{V}$ to remove oxide. Following the oxide removal step, sulfide was introduced to the elctrochemical cell, and S was deposited on the Ta surface at a range of potentials. EC-STM images following the surface morphology as a function of potential are shown in Figure 2.8. As the potential was shifted incrementally from $-1.5\,\mathrm{V}$ to $-0.5\,\mathrm{V}$, rod-like structures were seen to grow over the surface. These rods resemble the monoclinic TaS_3 (m-TaS_3) chain structure. Most transition metal trichalcogenides, like TaS_3 and $NbSe_3$, possess pseudo one-dimensional chain structures weakly held together by van der Waals forces.[15,48]

Figure 2.9 is a close-up image of the rod-like structure at $-1.3\,\mathrm{V}$ in a $2\,\mathrm{mM}$ Na_2S solution after a half hour of imaging. The measured interatomic distance, indicated by the solid line, was about $2.2\,\text{Å}$. The width of the rod, indicated by the dotted line, was about $6.8\,\text{Å}$. The separation between two rods (the dashed line), presumably by a van der Waals gap, was about $7.8\,\text{Å}$. Comparison of dimensions from the a-c plane of m-TaS_3 bulk crystals show a very similar chain-like structure to those observed in the EC-STM images in Figure 2.8.[49] The average sulfur interatomic distance was $2.5\,\text{Å}$ along the c-axis. The chain width along the a-axis was about $6.7\,\text{Å}$, while the van der Waals gap between chains was about $2.3\,\text{Å}$. Only the presumed van der Waals gap width disagrees appreciably between the measurements. If the rod-like structures do correspond to TaS_3, the discrepancy between the measured distances and those of the known bulk crystal may arise from stress exhibited by the TaS_3 chains on the Ta substrate. Van der Waals gaps are expected to be most susceptible dimensions to

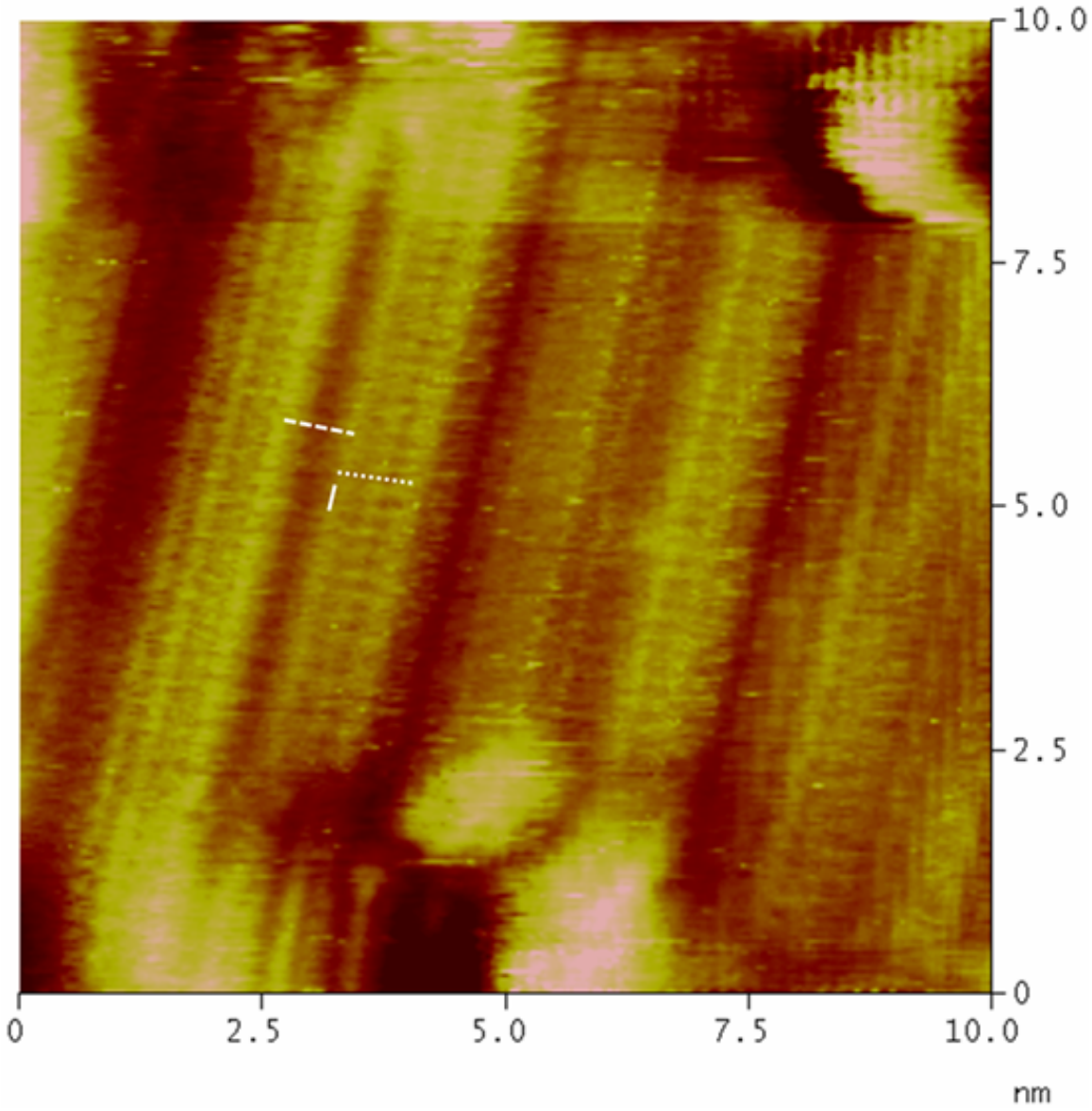

Figure 2.9: A close-up EC-STM image of the S-covered Ta/Au/glass surface in a 2 mM Na_2S solution at -1.3 V. The measured distances are about 2.2 Å (—), 6.8 Å ($\cdots$), and 7.8 Å (- - -). E_{bias} : 400 mV; I_{tip} : -27.9 nA.

such a stress, possibly resulting in a larger deviations in measured widths. The weak van der Waals forces can also be distorted by the tip/surface interaction, potentially leading to surface instability and perturbation by the tip.[48]

Following the oxide removal step, Cu was deposited onto a Ta/Au/glass substrate near $-1\,\mathrm{V}$ in a $1\,\mathrm{mM}$ $CuClO_4$ solution. Similar studies of electrochemical Ta oxide removal followed by Cu electrodeposition have been reported.[12,13] Atomically-resolved EC-STM images of the Cu lattice on the Ta at $-1\,\mathrm{V}$ in $0.1\,\mathrm{M}$ $KClO_4$ are shown in Figure 2.10. Step terraces resembling Cu(111) and Cu(100) were observed. In Figure 2.10a, the Cu(100)-like surface has an interatomic distance of $(0.27 \pm 0.02)\,\mathrm{nm}$ and an average step height of $(0.20 \pm 0.02)\,\mathrm{nm}$.

2.5 Conclusion

The electrochemical oxide reduction of Ta was studied by CV, STM and XPS. CV initially suggested some oxide can be reduced at very negative potentials, as indicated by changes in the HER current. In the EC-STM study, an oxide-removal step at $-1.8\,\mathrm{V}$ was used to obtain atomic resolution images. The EC-STM study also showed that an oxide-free Ta surface would spontaneously re-oxidize even at $-1\,\mathrm{V}$. Use of Te to passivate the Ta surface also resulted in atomic resolution, and suggested greatly increased stability, up to as much as $-0.3\,\mathrm{V}$. A "double zigzag" pattern observed in some STM images appears to be evidence of $TaTe_2$ formed on the surface. S and Cu were also deposited onto Ta following the oxide-removal step. EC-STM of the S layer on Ta displayed rod-like structures that resemble TaS_3 chains. CV and XPS data support these conclusions, but there are more questions to be addressed.

2.6 Acknowledgments

Support for this work is gratefully acknowledged and was from 311 NSF ECCS, award number 1124733.

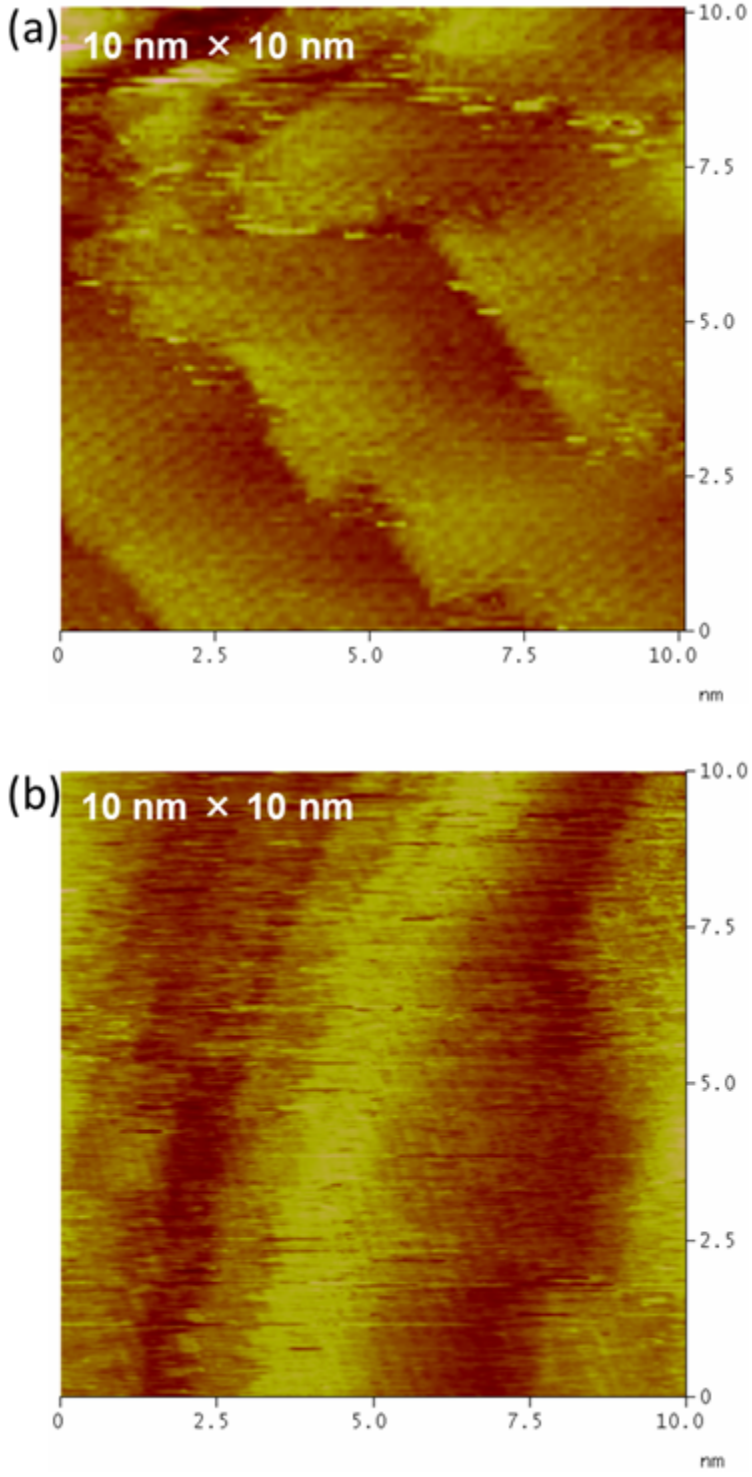

Figure 2.10: EC-STM images of Cu on Ta/Au/glass at (a) $-0.6\,\mathrm{V}$ and (b) $-1\,\mathrm{V}$ in $0.1\,\mathrm{M}$ $KClO_4$, showing step terraces resembling (a) the square array Cu(100) and (b) the hexagonal Cu(111). E_{bias} : (a) $300\,\mathrm{mV}$ and (b) $437\,\mathrm{mV}$; I_{tip} : $-30\,\mathrm{nA}$.

References

(1) Basame, S. B.; White, H. S. Chemically-selective and spatially-localized redox activity at Ta/Ta_2O_5 electrodes. *Langmuir* **1999**, *15*, 819–825.

(2) Macagno, V.; Schultze, J. W. The Growth and Properties of Thin Oxide Layers on Tantalum Electrodes. *Journal of Electroanalytical Chemistry* **1984**, *180*, 157–170.

(3) Mathieu, H. J.; Landolt, D. On the Influence of Crater Geometry on Depth Resolution of AES and XPS Profiles of Tantalum Oxide Films. *Surface and Interface Analysis* **1983**, *5*, 77–82.

(4) Housecroft, C. E.; Sharpe, A. G., *Inorganic Chemistry*, Second; Prentice Hall: 2005, pp 654–658.

(5) Bard, A. J.; Parsons, R.; Jordan, J.; Editors, *Standard Potentials in Aqueous Solution*; Marcel Dekker, Inc.: 1985, p 834.

(6) Enghag, P., *Encyclopedia of the elements: technical data, history, processing, applications*; Wiley-VCH: Weinheim, 2004.

(7) Silva, R. A.; Walls, M.; Rondot, B.; Belo, M. D.; Guidoin, R. Electrochemical and microstructural studies of tantalum and its oxide films for biomedical applications in endovascular surgery. *Journal of Materials Science-Materials in Medicine* **2002**, *13*, 495–500.

(8) Andricacos, P. C.; Uzoh, C.; Dukovic, J. O.; Horkans, J.; Deligianni, H. Damascene copper electroplating for chip interconnections. *Ibm Journal of Research and Development* **1998**, *42*, 567–574.

(9) Andricacos, P. C. Copper on-chip interconnections: a breakthrough in electrodeposition to make better chips. *Electrochem. Soc. Interface* **1999**, *8*, 32–37.

(10) Radisic, A.; Oskam, G.; Searson, P. C. Influence of oxide thickness on nucleation and growth of copper on tantalum. *Journal of the Electrochemical Society* **2004**, *151*, C369–C374.

(11) Zheng, M.; Kelly, J. J.; Deligianni, H. Electrodeposition of Cu on Ta-based layers - I. Electrodeposition on Ta. *Journal of the Electrochemical Society* **2007**, *154*, D400–D405.

(12) Starosvetsky, D.; Sezin, N.; Ein-Eli, Y. Seedless copper electroplating on Ta from an alkaline activated bath. *Electrochim. Acta* **2012**, *82*, 367–371.

(13) Starosvetsky, D.; Sezin, N.; Ein-Eli, Y. Seedless copper electroplating on Ta from a "single" electrolytic bath. *Electrochimica Acta* **2010**, *55*, 1656–1663.

(14) Wang, Q. H.; Kalantar-Zadeh, K.; Kis, A.; Coleman, J. N.; Strano, M. S. Electronics and optoelectronics of two-dimensional transition metal dichalcogenides. *Nat Nano* **2012**, *7*, 699–712.

(15) Srivastava, S. K.; Avasthi, B. N. Preparation, Structure and Properties of Transition-Metal Trichalcogenides. *Journal of Materials Science* **1992**, *27*, 3693–3705.

(16) Wilson, J. A.; Disalvo, F. J.; Mahajan, S. Charge-Density Waves in Metallic, Layered, Transition-Metal Dichalcogenides. *Physical Review Letters* **1974**, *32*, 882–885.

(17) Ogawa, N.; Miyano, K. Charge-density wave as an electro-optical switch and memory. *Applied Physics Letters* **2002**, *80*, 3225–3227.

(18) Mihailovic, D.; Dvorsek, D.; Kabanov, V. V.; Demsar, J.; Forro, L.; Berger, H. Femtosecond data storage, processing, and search using collective excitations of a macroscopic quantum state. *Applied Physics Letters* **2002**, *80*, 871–873.

(19) Goli, P.; Khan, J.; Wickramaratne, D.; Lake, R. K.; Balandin, A. A. Charge Density Waves in Exfoliated Films of van der Waals Materials: Evolution of Raman Spectrum in $TiSe_2$. *Nano Letters* **2012**, *12*, 5941–5945.

(20) Calandra, M.; Mazin, I. I.; Mauri, F. Effect of dimensionality on the charge-density wave in few-layer 2H-$NbSe_2$. *Phys. Rev. B: Condens. Matter Mater. Phys.* **2009**, *80*, 241108/1–241108/4.

(21) Levy, F.; Berger, H. Single-Crystals of Transition-Metal Trichalcogenides. *Journal of Crystal Growth* **1983**, *61*, 61–68.

(22) Thorne, R. E. Effect of Crystal-Growth Conditions on Charge-Density-Wave Pinning in $NbSe_3$. *Physical Review B* **1992**, *45*, 5804–5810.

(23) Patel, A. J.; Bhayani, M. K.; Jani, A. R. Growth and Surface Microtopography of 2H-TaS_xSe_{2-x} Single Crystals. *Chalcogenide Letters* **2009**, *6*, 491–502.

(24) Harris, F. R.; Standridge, S.; Johnson, D. C. The Synthesis of $[(Bi_2Te_3)_x$–$\{(TiTe_2)_y\}_{1.36}]$ Superlattices from Modulated Elemental Reactants. *Journal of the American Chemical Society* **2005**, *127*, 7843–7848.

(25) Stender, C. L.; Sekar, P.; Odom, T. W. Solid-state chemistry on a surface and in a beaker: Unconventional routes to transition metal chalcogenide nanomaterials. *Journal of Solid State Chemistry* **2008**, *181*, 1621–1627.

(26) Ueno, K.; Saiki, K.; Shimada, T.; Koma, A. Epitaxial-Growth of Transition-Metal Dichalcogenides on Cleaved Faces of Mica. *Journal of Vacuum Science & Technology A: Vacuum, Surfaces, and Films* **1990**, *8*, 68–72.

(27) Shimada, T.; Nishikawa, H.; Koma, A.; Furukawa, Y.; Arakawa, E.; Takeshita, K.; Matsushita, T. Polytypes and crystallinity of ultrathin epitaxial films of layered materials studied with grazing incidence X-ray diffraction. *Surface Science* **1996**, *369*, 379–384.

(28) Vaidyanathan, R.; Cox, S. M.; Happek, U.; Banga, D.; Mathe, M. K.; Stickney, J. L. Preliminary studies in the electrodeposition of PbSe/PbTe superlattice thin films via electrochemical atomic layer deposition (ALD). *Langmuir* **2006**, *22*, 10590–10595.

(29) Venkatasamy, V.; Jayaraju, N.; Cox, S. M.; Thambidurai, C.; Mathe, M.; Stickney, J. L. Deposition of HgTe by electrochemical atomic layer epitaxy (EC-ALE). *Journal of Electroanalytical Chemistry* **2006**, *589*, 195–202.

(30) Lister, T. E.; Stickney, J. L. Formation of the first monolayer of CdSe on Au(111) by electrochemical ALE. *Applied Surface Science* **1996**, *107*, 153–160.

(31) Nashed, R.; Hassan, W. M. I.; Ismail, Y.; Allam, N. K. Unravelling the interplay of crystal structure and electronic band structure of tantalum oxide (Ta_2O_5). *Physical Chemistry Chemical Physics* **2013**, *15*, 1352–1357.

(32) Basame, S. B.; White, H. S. Scanning electrochemical microscopy of metal / metal oxide electrodes. Analysis of spatially localized electron-transfer reactions during oxide growth. *Analytical Chemistry* **1999**, *71*, 3166–3170.

(33) Pourbaix, M., *Atlas of Electrochemical Equilibria in Aqueous Solutions*; Pergamon: 1966.

(34) Casillas, N.; Charlebois, S.; Smyrl, W. H.; White, H. S. Pitting Corrosion of Titanium. *Journal of the Electrochemical Society* **1994**, *141*, 636–642.

(35) Sapra, S.; Li, H. Q.; Wang, Z. C.; Suni, I. I. Voltammetry and impedance studies of Ta in aqueous HF. *Journal of the Electrochemical Society* **2005**, *152*, B193–B197.

(36) Askeljung, C.; Marinder, B. O.; Sundberg, M. Effect of heat treatment on the structure of L$-Ta_2O_5$: a study by XRPD and HRTEM methods. *Journal of Solid State Chemistry* **2003**, *176*, 250–258.

(37) Lee, S.-H.; Kim, J.; Kim, S.-J.; Kim, S.; Park, G.-S. Hidden structural order in orthorhombic Ta_2O_5. *Phys. Rev. Lett.* **2013**, *110*, 235502/1–235502/5.

(38) Thundat, T.; Nagahara, L. A.; Oden, P. I.; Lindsay, S. M.; George, M. A.; Glaunsinger, W. S. Modification of Tantalum Surfaces by Scanning Tunneling Microscopy in an Electrochemical Cell. *Journal of Vacuum Science & Technology A: Vacuum, Surfaces, and Films* **1990**, *8*, 3537–3541.

(39) Gebregziabiher, D. K.; Ledina, M. A.; Preisser, R.; Stickney, J. L. Cu(111) Surface Passivation with Atomic Layers of Te, Se or I, Studied Using Auger Spectrscopy. *Journal of the Electrochemical Society* **2012**, *159*, H675–H679.

(40) Lay, M. D.; Stickney, J. L. EC-STM studies of Te and CdTe atomic layer formation from a basic Te solution. *Journal of the Electrochemical Society* **2004**, *151*, C431–C435.

(41) Sorenson, T. A.; Varazo, K.; Suggs, D. W.; Stickney, J. L. Formation of and phase transitions in electrodeposited tellurium atomic layers on Au(111). *Surface Science* **2001**, *470*, 197–214.

(42) Gregory, B. W.; Norton, M. L.; Stickney, J. L. Thin-Layer Electrochemical Studies of the Underpotential Deposition of Cadmium and Tellurium on Polycrystalline Au, Pt and Cu Electrodes. *Journal of Electroanalytical Chemistry* **1990**, *293*, 85–101.

(43) Kim, S. J.; Park, S. J.; Jeon, I. C.; Kim, C.; Pyun, C.; Yee, K. A. AFM image visualization of layered dichalcogenides, 1T-MTe_2 (M = V, Ta). *Journal of Physics and Chemistry of Solids* **1997**, *58*, 659–663.

(44) Brown, B. E. Crystal Structures of $NbTe_2$ and $TaTe_2$. *Acta Crystallographica* **1966**, *20*, 264.

(45) Emery, S. B.; Hubbley, J. L.; Roy, D. Voltammetric and amperometric analyses of electrochemical nucleation: electrodeposition of copper on nickel and tantalum. *Journal of Electroanalytical Chemistry* **2004**, *568*, 121–133.

(46) Ghicov, A.; Schmuki, P. Self-ordering electrochemistry: a review on growth and functionality of TiO_2 nanotubes and other self-aligned MOx structures. *Chemical Communications* **2009**, 2791–2808.

(47) Ohno, Y. The scanning-tunneling microscopy, the X-ray photoelectron spectroscopy, the inner-shell-electron energy-loss spectroscopy studies of MTe_2 and M_3SiTe_6 (M = Nb and Ta). *Journal of Solid State Chemistry* **1999**, *142*, 63–73.

(48) Gammie, G.; Hubacek, J. S.; Skala, S. L.; Tucker, J. R.; Lyding, J. W. Surface-Structure Studies of Quasi-One-Dimensional Charge-Density Wave Compounds by Scanning Tunneling Microscopy. *Journal of Vacuum Science & Technology B* **1991**, *9*, 1027–1031.

(49) Meerschaut, A.; Guemas, L.; Rouxel, J. Structure and Properties of the New Phase of the Pseudo One-Dimensional Compound TaS_3. *Journal of Solid State Chemistry* **1981**, *36*, 118–123.

Chapter 3

Electrodeposition of Molybdenum Diselenide by Electrochemical Atomic Layer Deposition (E-ALD) [1]

[1] Tsang, C.; Ledina, M.; Stickney, J. To be submitted to the *Journal of the Electrochemical Society*.

3.1 Abstract

Cyclic voltammetry (CV) of Au in MoO_3 and SeO_2 solutions were studied under both basic and acidic conditions for the prospect of electrodepositing $MoSe_2$. Preliminary $MoSe_2$ thin films on Au substrates were formed by E-ALD from the acidic MoO_3 and SeO_2 precursor solutions. Photoelectrochemical (PEC) photovoltage measurements revealed an optical band gap of 1.1 eV for $MoSe_2$ in the as-deposited films. MoO_2 impurity was also detected in the films by the PEC measurements. Thermal annealing can be used to remove Se and MoO_x impurities from the films and to improve film crystallinity, as confirmed by X-ray photoelectron spectroscopy (XPS), Raman spectroscopy, and electron probe microanalysis (EPMA). This study reinforced the premise that Se can be used to suppress Mo oxidation and induce Mo deposition during the $MoSe_2$ film growth.

3.2 Introduction

Graphene is the epitome of a 2-dimensional (2D) material, and it has garnered the most spotlights among all the 2D materials known to date.[1] Trailing the torrential outpour of graphene-related publications, a separate class of 2D materials is firmly gaining footholds in the literature. Transition metal dichalcogenides (TMDCs) make up such a class of 2D materials that are capturing the attentions of material chemists, physicists and, engineers. Congruent to its name, TMDCs have the general formula MX_2, where M is a transition metal (such as Ta, Nb, Mo, or W) and X is a chalcogen (S, Se, or Te).[2] Each MX_2 trilayer is made up of two chalcogen layers sandwiching a transition metal center layer. The trilayers are stacked through van der Waals interaction in the bulk material, and different structural polytypes exist depending on the stacking orientations.[3]

TMDCs exhibit numerous intriguing properties befitting a wide range of potential applications. One such property is the ability of some TMDCs to undergo Peierls transitions to form charge density waves (CDW).[4] The possibility of utilizing CDW in electronic device applications has been considered, which recognized the need to grow TMDC nanofilms by alternative growth methods.[5,6] Preliminary electrochemical studies of chalcogen deposition onto Ta substrates by this group yielded promising results, affirming electrodeposition a viable technique for growing TMDCs.[7]

In the present study, Electrochemical Atomic Layer Deposition (E-ALD) was used to grow molybdenum diselenide ($MoSe_2$). Whereas conventional ALD is based on gas-phase chemical reactions, E-ALD is based on the sequential use of electrochemical reactions to deposit thin films. By using electrochemical surface-limited reactions, referred to as underpotential deposition (UPD), the deposits can be formed one atomic layer at a time.[8–14] Atomic layers of the elements are deposited alternately on each other, in a cycle. The number of cycles performed dictates the thickness of the deposit.

Properties of molybdenum dichalcogenides have been widely investigated for their potential applications. As the material thickness decreases, both band gaps of MoS_2 and $MoSe_2$ exhibit a crossover from indirect to direct transitions in the limit of a single layer.[15–17] Owing to their band gap energies in the UV-visible region, MoS_2 and $MoSe_2$ have potential uses in making photonic and optoelectronic devices.[18,19] In the area of renewable solar energy research, $MoSe_2$ can be used as a catalyst for hydrogen evolution reaction (HER).[20,21] Group VI transition metal dichalcogenides such as $MoSe_2$ and MoS_2 can be suitable photoelectrodes in regenerative electrochemical solar cells because they are less susceptible to photodecomposition. Their photogenerated excitons originate from the non-bonding *d*-orbitals, thus the photoinitiated reactions arising from these transitions do not directly result in broken crystal bonds.[22]

The difficulty in electrodepositing $MoSe_2$ stems from the negative standard reduction potential for molybdenum deposition, which occurs at a potential where HER

can thermodynamically occur. In theory, Mo electrodeposition can proceed by this reaction[23,24]

$$MoO_4^{2-} + 4\ H_2O + 6\ e^- \longleftrightarrow Mo + 8\ OH^- \qquad E^0 = -0.913\,V \text{ vs. S.H.E.} \quad (3.1)$$

Pure Mo electrodeposition from aqueous solutions typically has ∼1 % current efficiency at best due to the concurrent HER as the dominant side reaction.[25,26] Metallic Mo can be electrodeposited more easily as an alloy with Fe, Co, or Ni.[27,28] The success in codepositing Mo as an alloy with an Fe-group metal guided the prospect of using chalcogen to induce Mo electrodeposition.[29–32] The present work examines the electrodeposition of Mo in the presence of Se. The deposition of both Mo and Se effectively formed $MoSe_2$. Preliminary $MoSe_2$ thin films were grown by E-ALD. While the as-deposited films contained significant amount of oxide impurity, the film compositions were improved by annealing at reasonably low temperatures. Improvements in the quality of the as-deposited films can be expected by further optimization of the deposition conditions.

3.3 Experimental

All potentials were reported vs. a Ag/AgCl (3 M KCl) reference electrode (Bioanalytical Systems, Inc.). The Au substrates (EMF Corp) were 100 nm of Au (99.9 %) evaporated onto glass slides coated with 50 Å of Ti as the adhesion layer. All solutions were prepared with 18 MΩ H_2O from a Milli-Q purification system. The MoO_3 solutions were prepared by first sonicating to dissolve MoO_3 (J.T. Baker, 99.5 %) with one NaOH (Fisher Scientific, 99.6 %) pellet in ∼20 mL H_2O. The solution was then diluted to final volume and adjusted to the proper pH. In the basic MoO_3 solution, NH_4Cl (Macron Fine Chemicals, ACS grade) was added prior to the dilution. To make the acidic MoO_3 solution, $HClO_4$ (J.T. Baker, 60–62 %) was used to acidify the basic MoO_3 solution without adding NH_4Cl. The SeO_2 (Alfa Aesar, 99.999 %) solutions

were made by dissolving SeO_2 in H_2O, then adjusting the pH with $HClO_4$ or NaOH. All solutions contained 0.1 M $NaClO_4$ as supporting electrolyte. The $NaClO_4$ stock solution was prepared by neutralizing $HClO_4$ with NaOH. Commercial $MoSe_2$ (Alfa Aesar, 99.9 %) powder was used as a reference in the Raman study.

All electrochemical experiments were done in an automated flow deposition system (Electrochemical ALD, L.C., Athens, GA). The system was comprised of several different solution bottles connected to a distribution valve. The valve was further connected to an electrochemical deposition flow cell and a peristaltic pump. The flow cell was a 3-electrode cell that housed a substrate as the working electrode, a 3 M Ag/AgCl reference electrode, and a Au wire auxiliary electrode parallel to the planar working electrode. The cell had a volume of about 0.3 mL, and its potential was controlled by a potentiostat. The entire system was interfaced to a computer to allow remote control of the cell potential and the solution flow. During $MoSe_2$ deposition, the flow rate was 15 mL min^{-1} for all steps except the stagnant deposition steps where there was no flow. All CVs were done at a potential scan rate of 10 mV s^{-1} and under flowing conditions at a flow rate of $\sim$2 mL min^{-1}. All solutions were purged with N_2 (Airgas) before each experiment.

Electron probe microanalysis (EPMA) of the samples was performed on a JEOL JXA-8600 Superprobe using an electron beam of 10 µm diameter, 10 keV accelerating voltage, and 15 nA current. Scanning electron microscopy (SEM) and energy-dispersive X-ray spectroscopy (EDS) were performed on a FEI Inspect F50 FEG SEM (FEI, Hillsboro, OR). STM images were obtained in air using a Nanoscope III (Digital Instruments, Santa Barbara, CA) with a tungsten tip. Raman spectra were obtained using a Renishaw inVia Raman microprobe (Renishaw, Wotton-under-edge, U.K.) equipped with a CCD detector. A 514-nm Ar-ion laser (Modu-Laser, LLC, Centerville, UT) running at 0.67 mW was used as the excitation source. An 1800-lines/mm grating and a 20X objective were used during the spectral acquisition. X-ray photo-

electron spectroscopy (XPS) was performed using a Mg K$\alpha_{1,2}$ (STAIB) X-ray source, at $\sim$70° to hemispherical analyzer axis (Leybold Heraeus). The Au $4f_{7/2}$ peak at 84.0 eV originating from the substrate was used to calibrate the binding energies. A Shirley background was assumed and subtracted for each spectrum.[33]

In the photoelectrochemical (PEC) measurements, the light from a 300 W Xe arc lamp (Oriel Instruments, Stratford, CT) was dispersed by a monochromator (Oriel Cornerstone 260 Model 74100) equipped with a 1200-lines/mm grating. The light was then chopped at 20 Hz and illuminated onto the $MoSe_2$ sample through a quartz window. The sample was immersed in 0.1 M $NaClO_4$ electrolyte solution at pH 1.5. The photovoltage was measured as the 20-Hz component of the open-circuit potential through a lock-in amplifier (Standard Research Systems Model SR830, Sunnyvale, CA).

Sample annealings were performed in a tube furnace (Lindberg/Blue Model TF55030A-1, Asheville, NC) in a H_2-Ar mixture (Airgas) containing 1 % H_2 and 99 % Ar (Airgas). In each annealing, the temperature was ramped from room temperature up to the annealing temperature at 5 °C min^{-1}. After half an hour at the annealing temperature, the temperature was then ramped down to room temperature at no more than 5 °C min^{-1}.

3.4 Results and Discussion

3.4.1 Voltammetric Behavior of Mo and Se

A cyclic voltammogram (CV) of Au in 1 mM MoO_3 is shown in Figure 3.1. Starting from the open-circuit potential (ocp) of 63 mV, the potential was scanned negatively toward −1 V. The onset of reduction occurred at −850 mV. Hysteresis was observed whereby the reductive current on the reverse scan was higher than that on the forward scan. This may be due to a nucleation and growth mechanism by which MoO_x was deposited from reduction of MoO_4^{2-} species in solution. The HER overpotential on

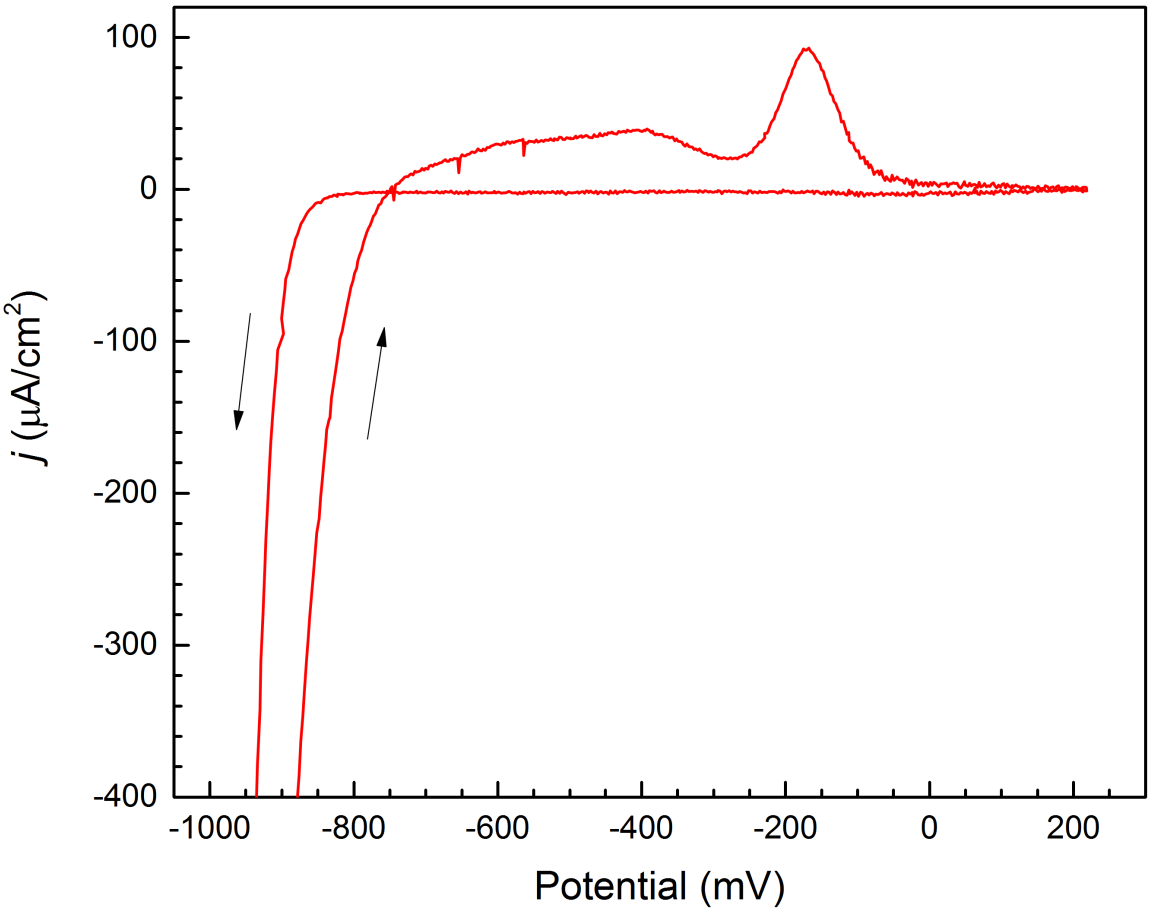

Figure 3.1: CV of Au in 1 mM MoO_3 and 1 M NH_4Cl (pH 8.3). Open-circuit potential was 63 mV. The negative-going forward scan was reversed at −1 V.

a Mo surface is lower than that on a Au surface.[26] Deposition of MoO_x may trigger extensive HER, leading to more reductive current on the reverse scan than on the forward scan. On the reverse scan, the reductive current was quickly followed by the oxidative current at −750 mV. The oxidation consists of two observable components: a broad oxidation, followed by a Gaussian-shaped oxidation peak. The abrupt transition from reductive to oxidative current suggests that a side reaction, likely HER, was occurring during the transition. Integration of the current revealed that there was more than six times as much reductive charge as oxidative charge, confirming the notion that HER was the dominant side reaction. While it is uncertain what role NH_3 played in the reduction of ${MoO_4}^{2-}$, it is worth noting that the reduction under basic conditions would not proceed without the presence of NH_3. In this CV study, NH_4Cl served as the source of NH_3.

To examine the electrochemistry of Mo in an acidic condition, the MoO_3 solution was acidified to pH 1.5. CV of Au in the acidic MoO_3 solution is shown in Figure 3.2. The open-circuit potential was 423 mV. On the negative-going scan from ocp, a shoulder was observed prior to the onset of HER. This reduction was attributed to the reduction of Mo^{VI} species in solution. No hysteresis was observed, contrary to the case in pH 8.3. The oxidation features, however, appear very comparable to the oxidation in pH 8.3: a broad oxidation, followed by another oxidation peak.

Further experiments were done to help elucidate the nature of this oxidation. In a flow cell, MoO_x was deposited onto a Au electrode at −410 mV for 30 s from the acidic MoO_3 solution. The solution was subsequently replaced with a blank solution at open circuit. CV of the electrode in the blank solution under flowing condition is shown in Figure 3.3. The ocp was −185 mV, from which the potential was scanned to 200 mV. The broad oxidation was immediately observed as the potential was scanned positively from ocp, which is reminiscent of a passivation process.[7,34] After oxidizing at potentials up to 200 mV, the potential was scanned to −1.3 V, followed by a positive

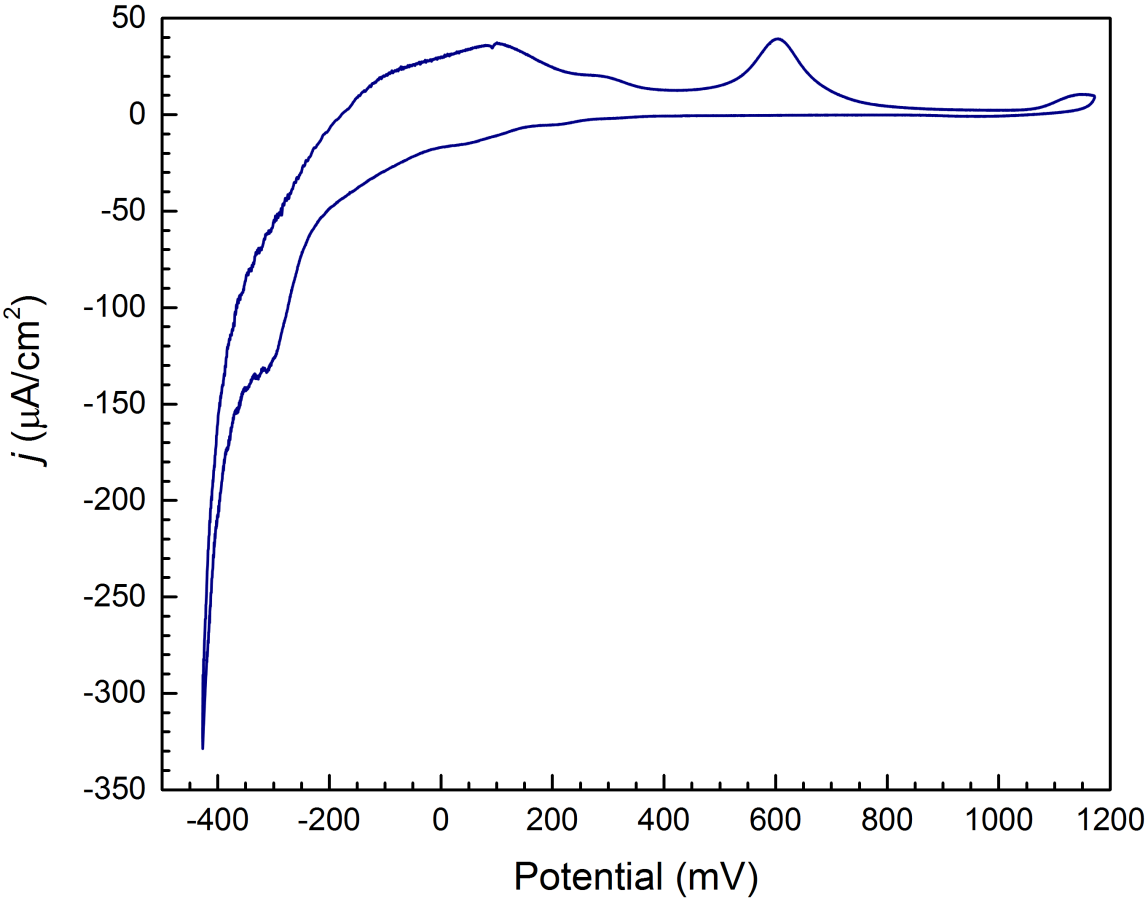

Figure 3.2: CV of Au in 1 mM MoO_3 (pH 1.5). Open-circuit potential was 423 mV.

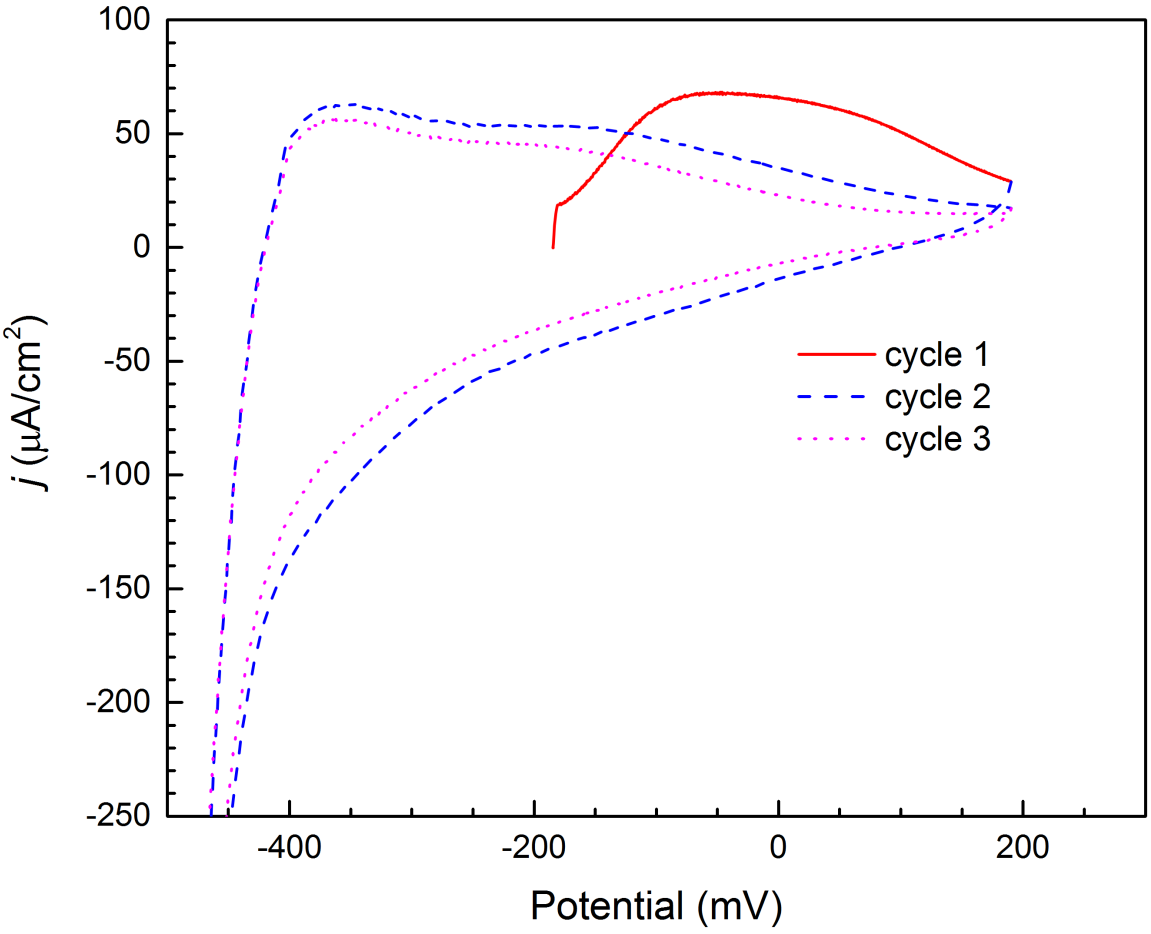

Figure 3.3: CV of MoO_x/Au in 0.1 M $NaClO_4$ (pH 1.5). Open-circuit potential was −185 mV. In cycles 2 and 3, the negative-going scan was reversed at −1.3 V.

scan to 200 mV again. The reappearance of the broad oxidation peak confirms that the dominant product of this oxidation is insoluble. This insoluble product can be oxidized to a soluble species by scanning the potential up to 1 V.

By analyzing this result within context of the Pourbaix diagram for Mo, the first broad oxidation can be attributed to the oxidation of metallic Mo to the passive MoO_2.[35] A repeat of the scan from -1.3 V to 200 mV (cycle 3 in Figure 3.3) showed slightly less oxidation charge than its preceding scan. This may be a result of some metallic Mo oxidizing to the soluble Mo^{3+} under the highly acidic condition, though this appears to be a minority product of the oxidation. The soluble product of MoO_2 oxidation at further positive potentials can be attributed to a Mo^{VI} species.

Selenium deposition was also examined as a function of solution pH. At pH 8.3, no Se deposition was evident according to a CV of Au in 0.1 mM SeO_2. Deposition from a 0.5 mM SeO_2 solution was also attempted without success. At pH 5, shown in Figure 3.4, Se deposition appeared to be limited to mostly UPD. The onset of UPD oxidation is about 550 mV, and the most oxidation charge from the Se stripping corresponded to 0.5 monolayer (cycle 1). Here, one monolayer is defined as one adsorbate atom (Se) for every substrate surface atom (Au). All subsequent scans, even to more negative potentials, showed less oxidation. The slow kinetics and irreversibility of Se deposition at pH 5 prompted a further lowering of the solution pH. At pH 1.5, the behavior of Se appeared markedly different. The features for Se deposition and stripping, shown in Figure 3.5, are much more discernable. On the negative-going scan from ocp of 430 mV, the first two reduction peaks correspond to surface-limited deposition of UPD Se.[36] Its corresponding oxidation occurred at 780 mV. Se UPD was followed by bulk Se deposition until ~ -250 mV, where bulk Se reductively stripped to Se^{2-}. HER on the Se surface occurred at ~ -600 mV. Compared to the CV of Au in a MoO_3 solution (Figure 3.2), HER overpotential on the Se surface was about 200 mV higher than that on a MoO_x surface. Since pure Mo electrodeposition is hindered by

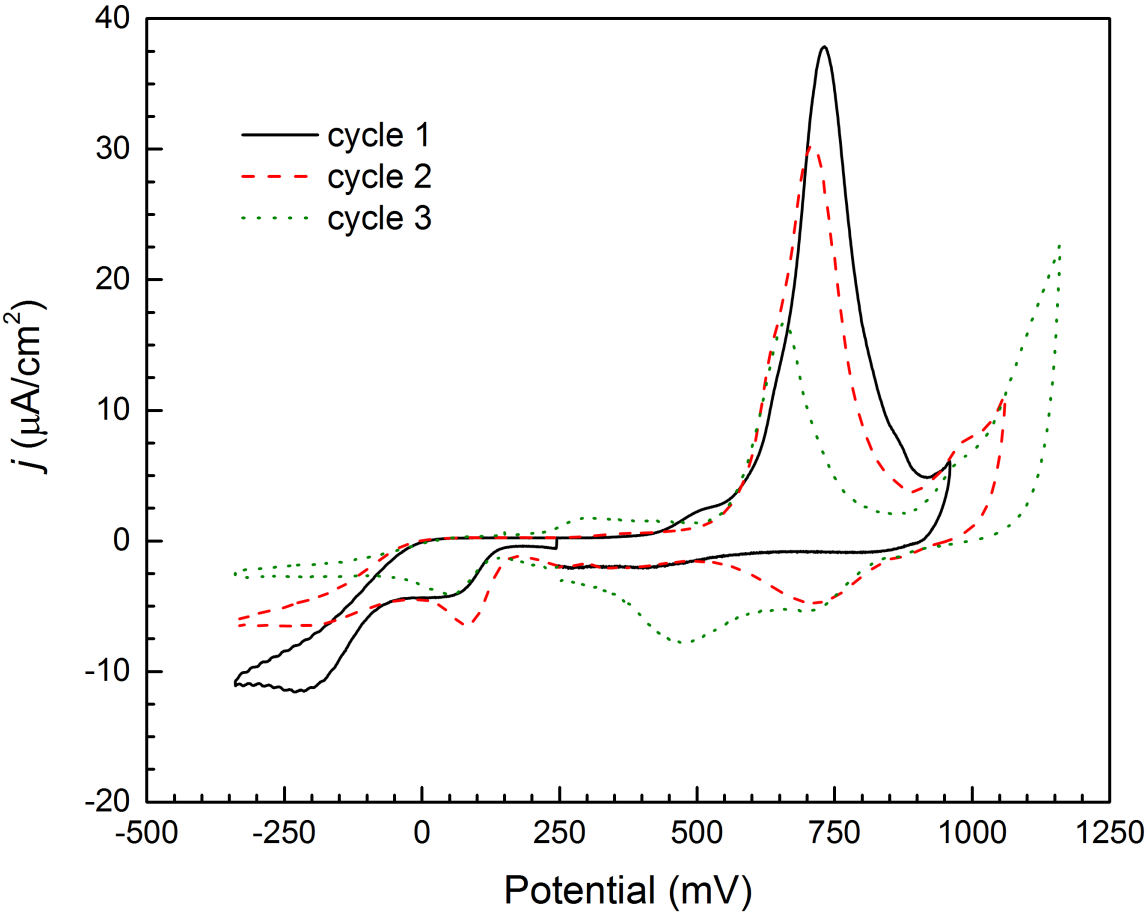

Figure 3.4: CV of Au in 0.1 mM SeO_2 (pH 5). Open-circuit potential was 245 mV.

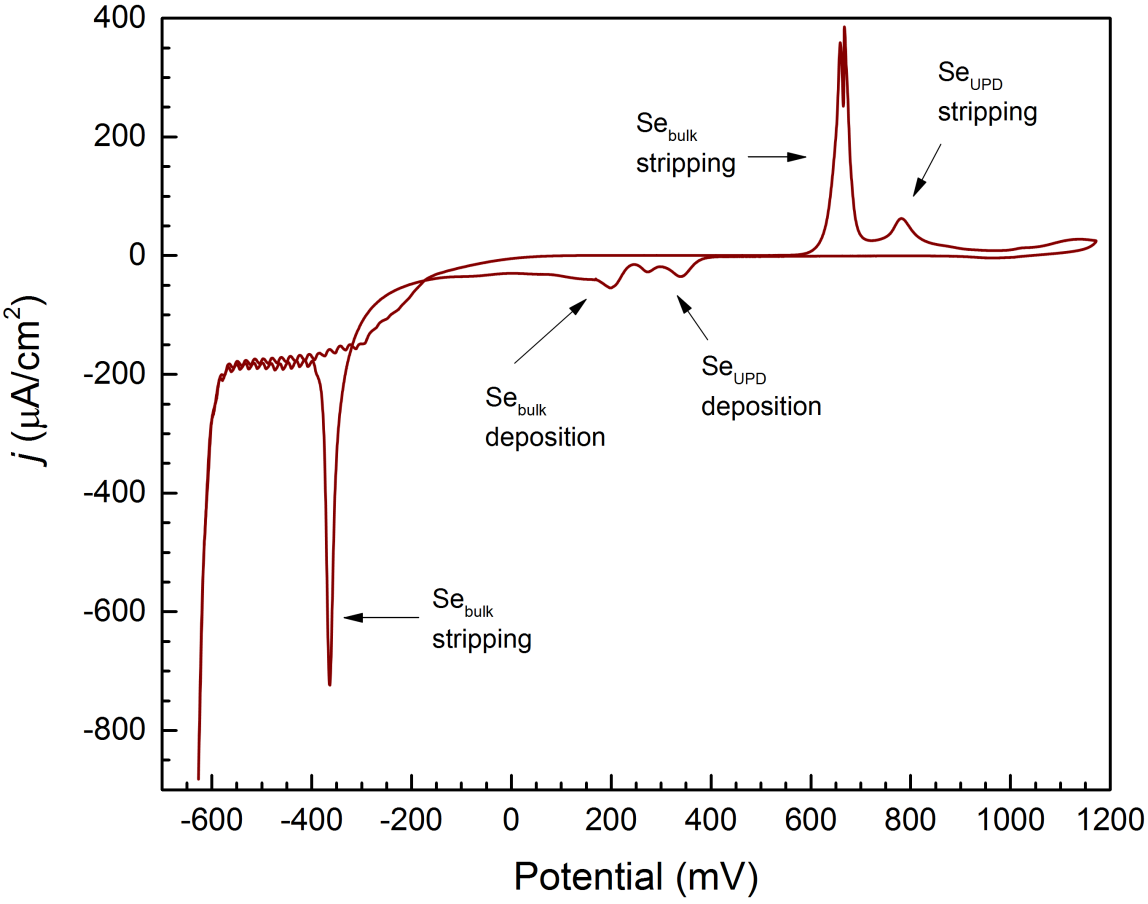

Figure 3.5: CV of Au in 0.5 mM SeO_2 (pH 1.5). Open-circuit potential was 430 mV.

extensive HER, this higher HER overpotential on Se might be a determinant factor for inducing Mo deposition in the formation of $MoSe_2$.

3.4.2 E-ALD of $MoSe_2$

For $MoSe_2$ deposition, the precursor solutions were 0.5 mM SeO_2 and 1 mM MoO_3. Both solutions were adjusted to pH 1.5. A simplified scheme for forming $MoSe_2$ by E-ALD is shown in Figure 3.6. Prior to $MoSe_2$ deposition, the Au substrate in a flow cell was coated with UPD Se (step **a**). MoO_x was then deposited from the MoO_3 solution at a potential designated as $E1$ (step **b**). Following the MoO_x deposition step, the MoO_3 solution was replaced by a blank solution, followed by the SeO_2 solution. Se was deposited from the SeO_2 solution at $E1$ (step **c**). In the final step (step **d**), the potential was stepped to $E2$, a more negative potential than $E1$. At the more negative $E2$, the MoO_x was reduced to form $MoSe_2$. Any excess bulk Se was also expected to reductively strip at $E2$. Steps **b** to **d** formed an E-ALD cycle that can be repeated to grow thicker films. When switching between precursor solutions, a pH 1.5 blank solution was always used to rinse out the antecedent precursor to avoid intermixing of the two precursors. An example of an E-ALD cycle is shown in Figure 3.7, which shows the solutions and potentials used in each step of the deposition cycle, along with the corresponding current response.

CV was used to characterize some preliminary $MoSe_2$ films grown using the E-ALD scheme depicted in Figure 3.7. During the growth of these films, $E1$ was -200 mV, and $E2$ was -400 mV. Stripping voltammograms of these films are shown in Figure 3.8. To strip these films, the potential was scanned from -400 mV to 1.5 V. For ease of comparison, only the films that were 4-, 5- and 6-cycles thick are shown. A prominent Gaussian-like oxidation peak was observed in each scan. The position of these peaks shifted more positive as the number of E-ALD cycles increased, suggesting that film stability increased with cycle numbers or film thickness. It is also important to note

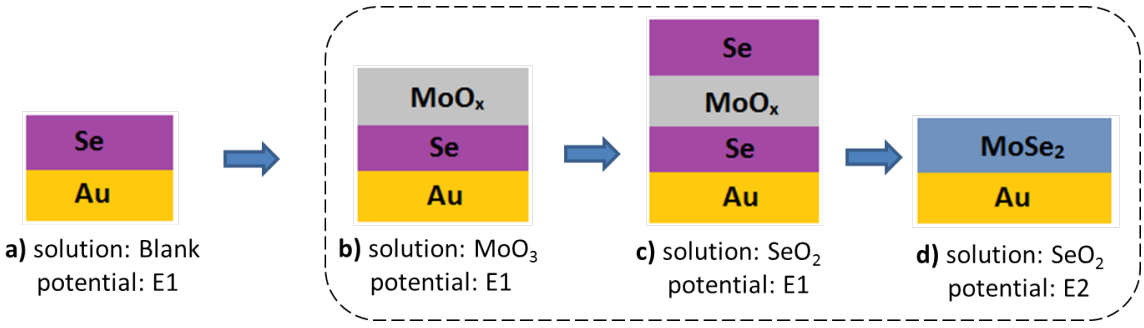

Figure 3.6: A simplified scheme for forming $MoSe_2$ by E-ALD. Steps **b** to **d** are repeated to deposit $MoSe_2$ in an ALD manner. Blank solution rinse steps are excluded in this illustration.

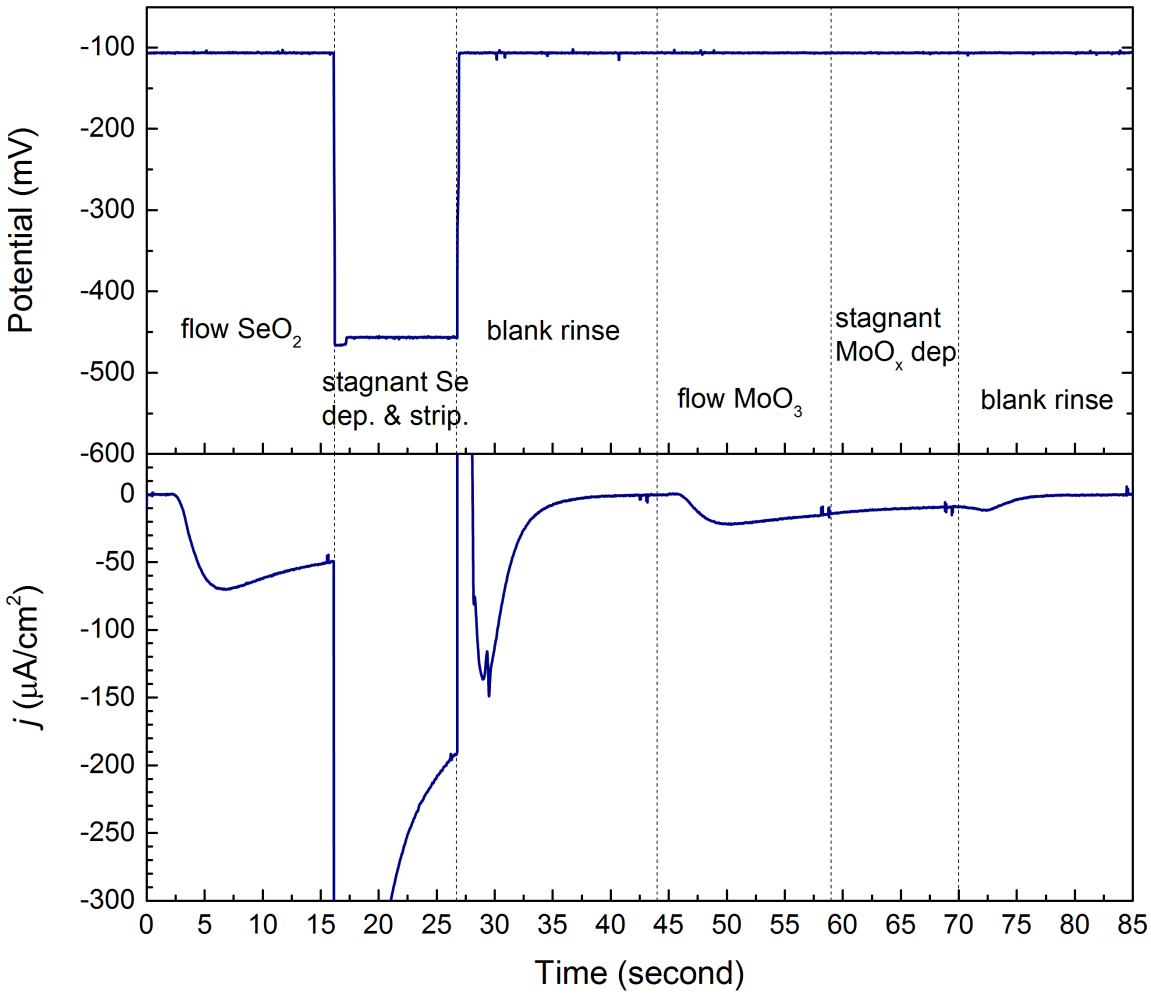

Figure 3.7: Potential profile used in an E-ALD cycle of $MoSe_2$, along with the corresponding current response. The vertical dashed lines mark the different steps in the cycle.

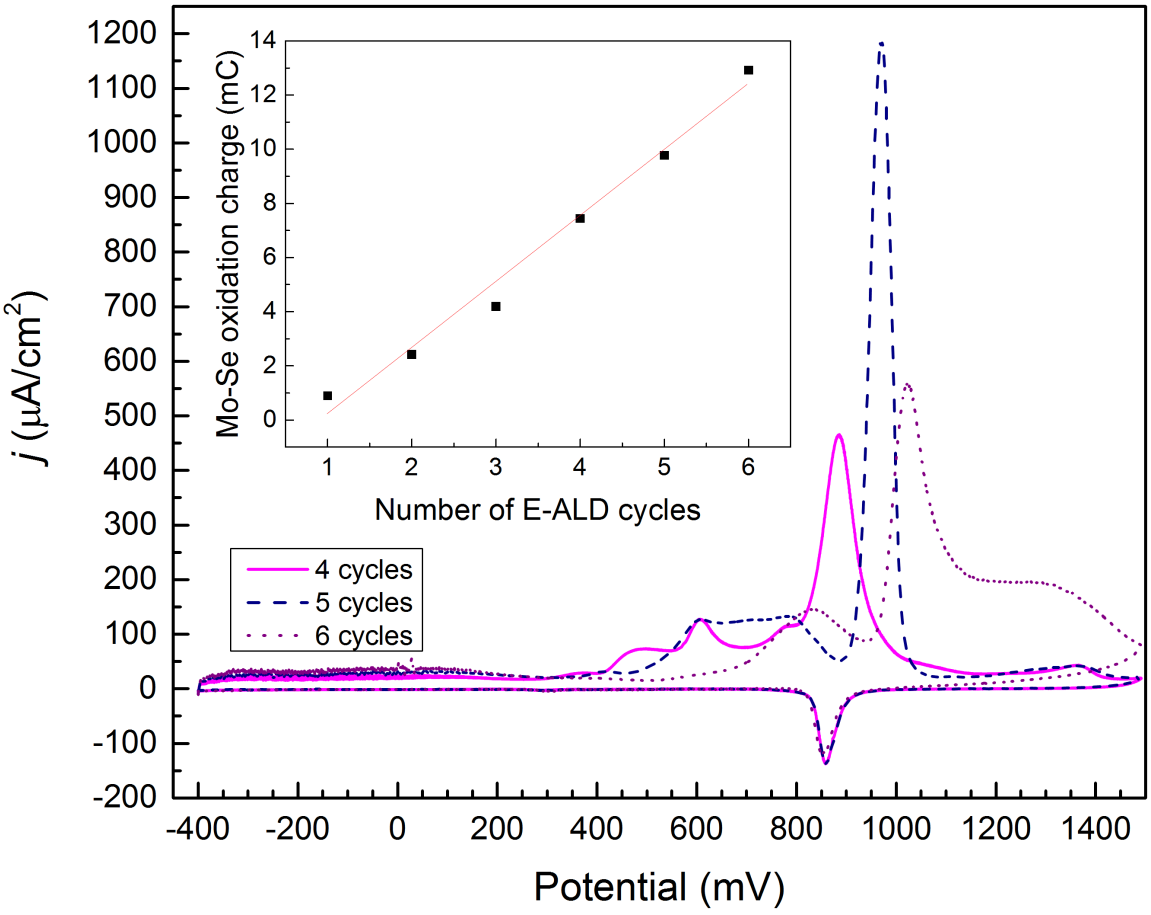

Figure 3.8: Oxidative stripping voltammograms in blank solution of preliminary $MoSe_2$ films grown by E-ALD. These films were grown by using $E1 = -200\,\mathrm{mV}$ and $E2 = -400\,\mathrm{mV}$. The inset shows the integrated oxidative charge from each film as a function of the number of E-ALD cycles.

that these oxidation peaks occurred at more positive potentials than the MoO_x or bulk Se oxidations seen in Figures 3.3 and 3.5, respectively. A gain in stability as a result of compound formation may result in the compound oxidizing at a potential more positive than the constituent elements alone.[37] Thus, this oxidation peak might be attributed to $MoSe_2$ oxidation.[38] The relative amount of deposition in each film can be quantified by integrating the oxidative stripping current to yield the charge. These charges as a function of the number of E-ALD cycles are plotted in the inset of Figure 3.8. The linear increase is consistent with an ALD process, confirming that thicker films can be deposited by increasing the number of E-ALD cycles.

Photoelectrochemistry was used to characterize a 50-cycle film grown by the same condition. In this PEC study, the photovoltage of the film was measured as a function of photoexcitation energy. The photovoltage is a change in the electrode's open-circuit potential arising from photogenerated electron-hole pairs.[39] It can be used to indirectly probe the absorption of light by the electrode. Since the Au substrate was not transparent to light in the UV-visible region, this is a convenient technique for characterizing the optical properties of these films. Figure 3.9 shows the photovoltage measurement for the 50-cycle film sample. Under the experimental conditions used, the photovoltage, E_{ph}, was assumed proportional to the optical absorption coefficient. This was the basis for plotting the data in the form of a Tauc plot for determining an optical bandgap.[40] Two absorption edges confirmed the presence of both $MoSe_2$ and MoO_2 in the film, which prompted the construction of two Tauc plots. MoO_2 has been known to show a direct transition, while bulk $MoSe_2$ is known to have an indirect band gap.[16,19,41] Extrapolating the corresponding absorption band edges yielded an optical band gap of 2.5 eV for MoO_2 and 1.1 eV for $MoSe_2$, both of which matched very well with literature values.[42]

To optimize the deposition potentials, $E1$ and $E2$, a series of 50-cycle deposits were prepared by varying $E1$ while holding $E2$ constant at -500 mV. Another series

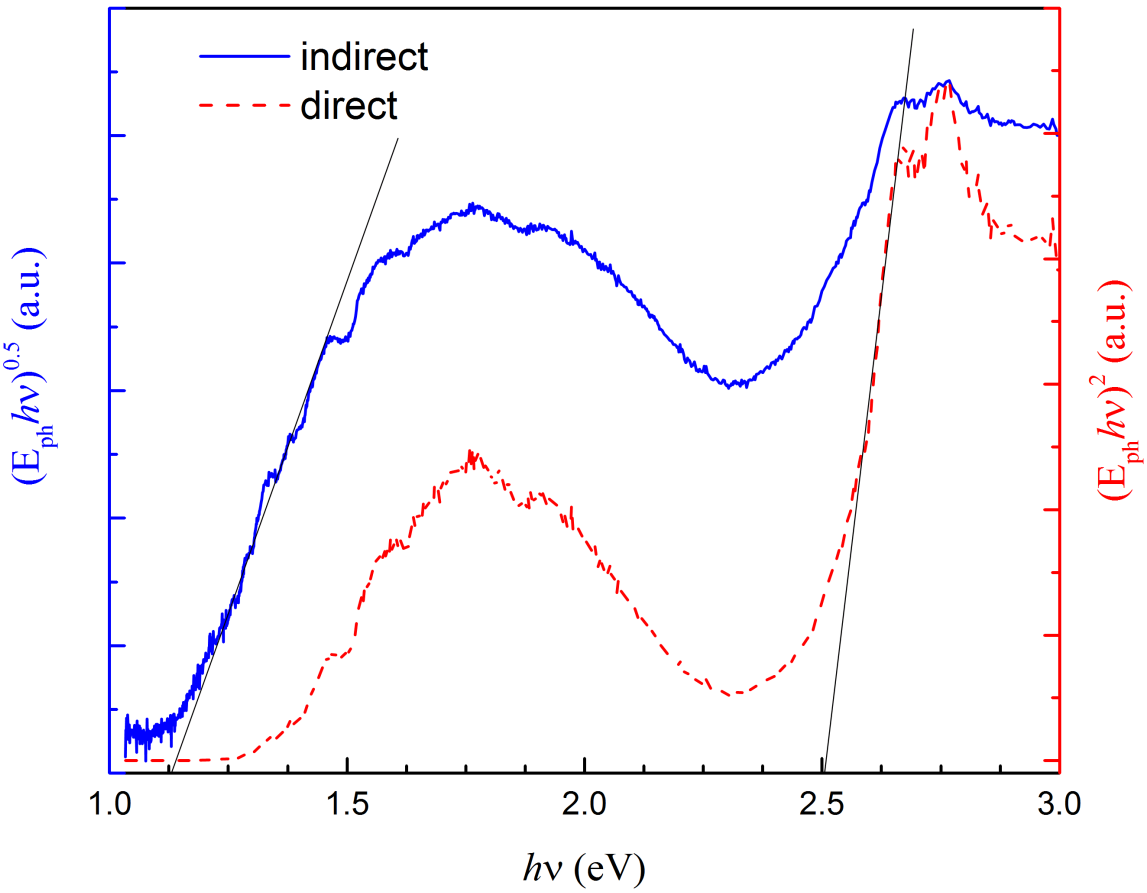

Figure 3.9: Photovoltage measurement of a $MoSe_2$ film grown by 50 E-ALD cycles. The data was plotted in two different forms that are appropriate for determining either a direct or an indirect band gap.

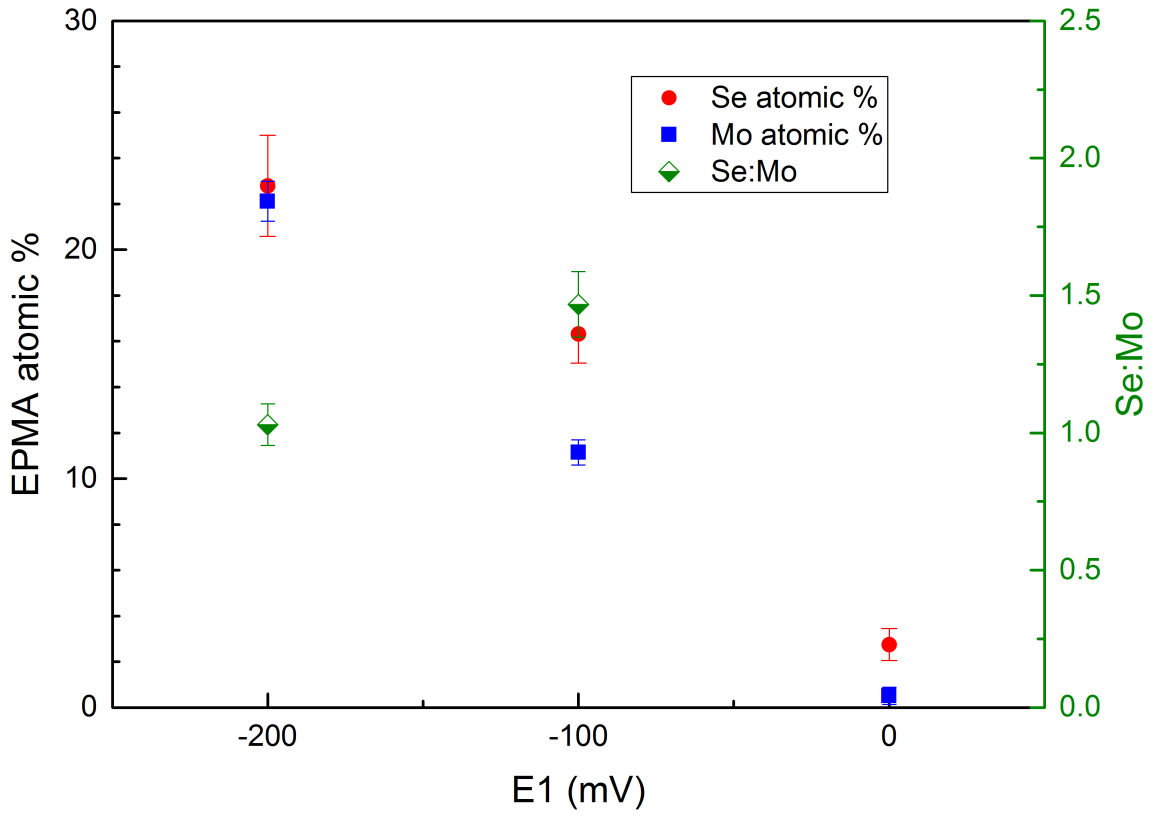

Figure 3.10: Composition analysis by EPMA for the series of 50-cycle deposits where $E1$ was varied while holding $E2$ constant at $-500\,\mathrm{mV}$.

of deposits were also prepared by varying $E2$ while holding $E1$ constant at $-100\,\mathrm{mV}$. The elemental compositions of these deposits were examined using EPMA. Figure 3.10 shows the composition analysis for the first series where $E2$ was held constant. The increase in Mo content at more negative $E1$ was expected, but the complementary increase in Se content was not as obvious. During the potential step to $E2 = -500\,\mathrm{mV}$ in the E-ALD cycle, only UPD Se was expected to remain on the surface because bulk Se would reductively strip at this potential. Furthermore, the CV for Se (Figure 3.5) showed approximately the same diffusion-limited deposition current from $0\,\mathrm{mV}$ to $-200\,\mathrm{mV}$. Hence the amount of Se deposited at $E1$ within the potential range shown in Figure 3.10 should not directly depend on $E1$. The amount of Se deposited, however, was affected indirectly by $E1$. This may be ascribed to the higher amount of MoO_x deposition at more negative $E1$ values. If only UPD Se were deposited by a surface-limited reaction, as presumed here, then more MoO_x deposition would lead to more Se deposition. Such surface-limited depositions are highly desirable for a layer-by-layer growth by E-ALD.

Figure 3.11 shows the composition analysis for the second series of deposits where $E1$ was held constant at $-100\,\mathrm{mV}$. $E2 < -400\,\mathrm{mV}$ was necessary to adequately strip the bulk Se. Although the amount of MoO_x deposited at $E1 = -100\,\mathrm{mV}$ should be constant, the Mo content in the deposits increased as $E2$ decreased. From this trend, it can be inferred that MoO_x was slowly reduced at $E2$ and subsequently bonded with Se, presumably forming $MoSe_2$. During the subsequent potential step from $E2$ to $E1$, $MoSe_2$ would suppress oxidation of the Mo into a soluble species, and thus a higher Mo content was observed for deposits made at a lower $E2$. In this series, the deposit made at $E2 = -450\,\mathrm{mV}$ and $E1 = -100\,\mathrm{mV}$ was chosen for the following annealing studies because it had a Se : Mo ratio closest to 2.

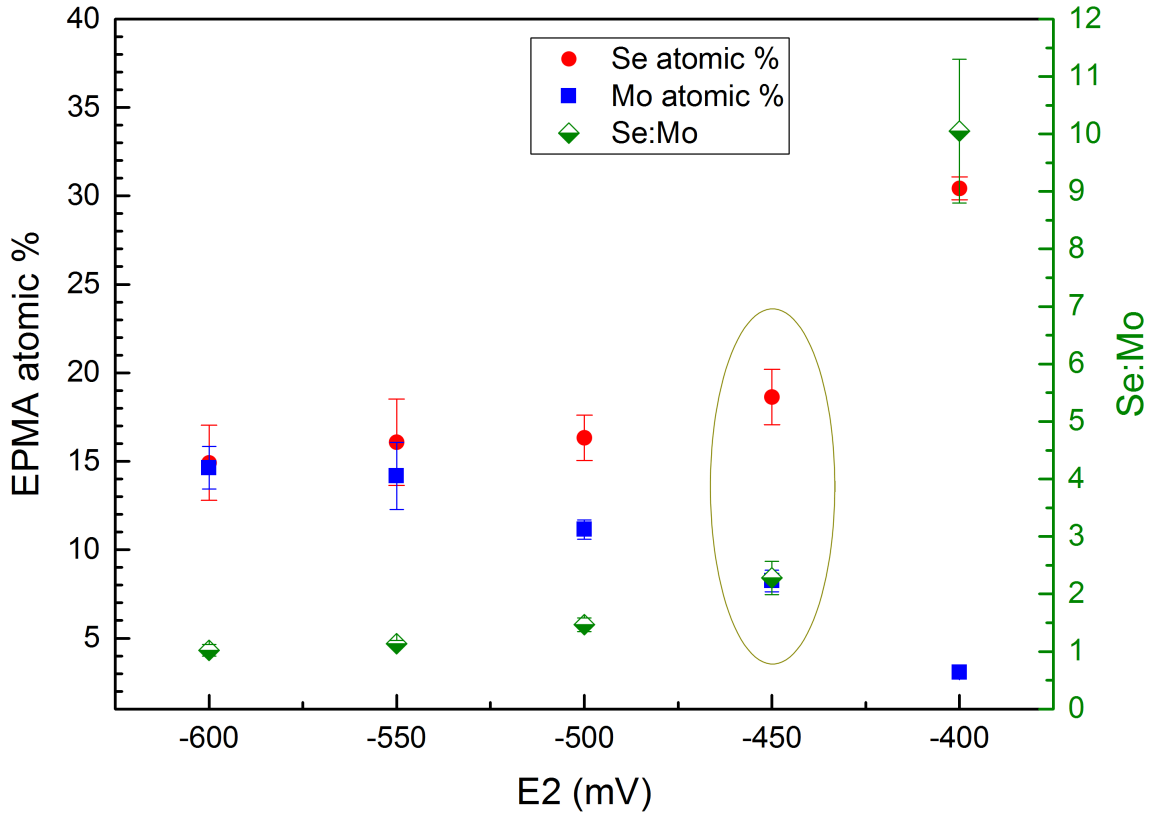

Figure 3.11: Composition analysis by EPMA for the series of 50-cycle deposits where $E2$ was varied while holding $E1$ constant at $-100\,\mathrm{mV}$.

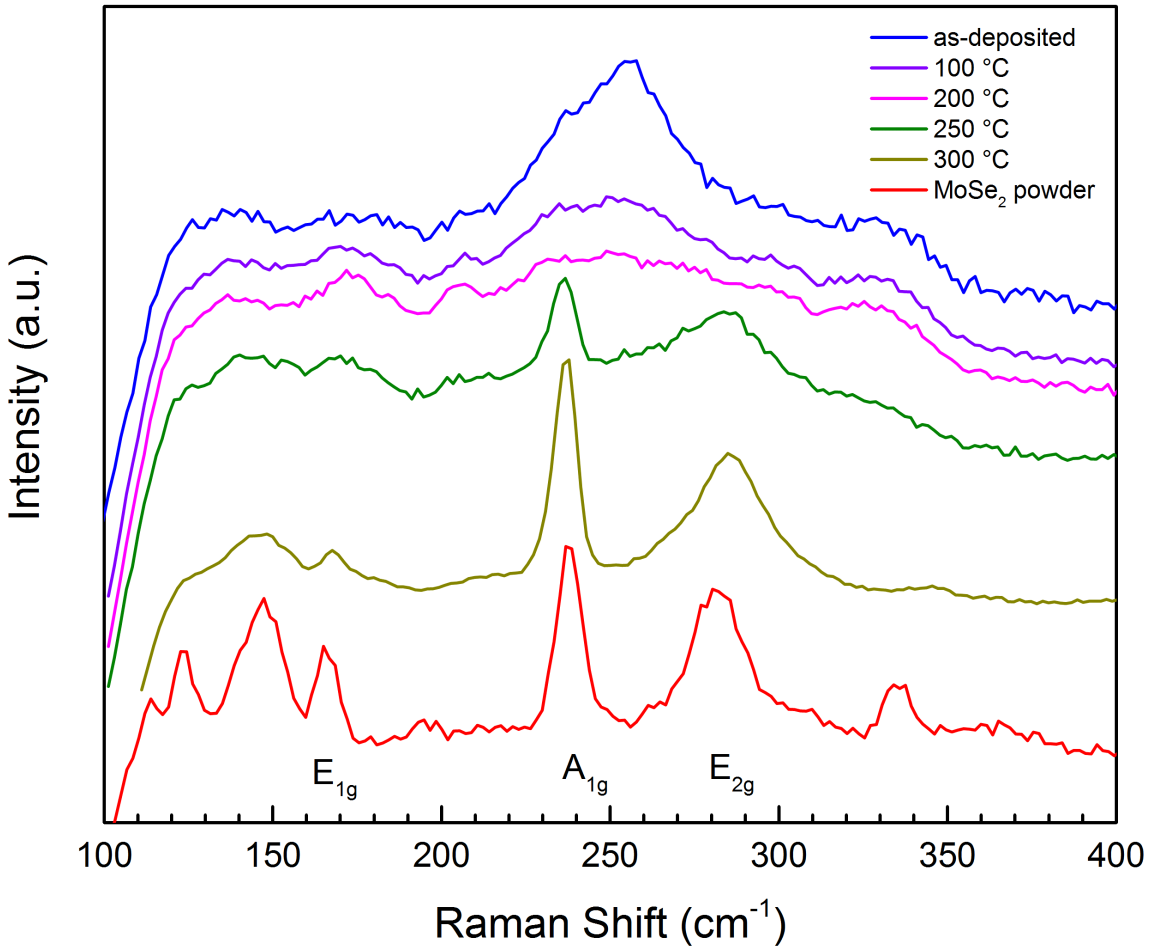

Figure 3.12: Micro-Raman spectra of some $MoSe_2$ films annealed at different temperatures.

3.4.3 Annealing Studies

Deposits made using $E1 = -100\,\mathrm{mV}$ and $E2 = -450\,\mathrm{mV}$ were thermally annealed in an atmosphere of 1 % H_2 and 99 % Ar. The evolution of their Raman spectra as a function of annealing temperature is shown in Figure 3.12. A broad asymmetric peak centered at $256\,\mathrm{cm}^{-1}$ was observed in the as-deposited film. This peak can be assigned to a Se-Se stretch mode, arising from a slight Se excess in the film.[20] No significant changes in the Raman spectra were observed until the films were annealed at 250 °C or above. At 250 °C and above, the well-known E_{1g}, A_{1g} and E^1_{2g} peaks of $MoSe_2$ can be identified.[16,43,44] The Raman spectrum of a commercial $MoSe_2$ powder sample is also shown for reference.

XPS was also used to follow the effect of annealing on the $MoSe_2$ films. Figure 3.13 shows XPS spectra for the Mo 3*d* and Se 3*d* regions. The Mo 3*d* signal from the as-deposited film and the film annealed at 100 °C appeared to originate predominantly from Mo oxides on the surface. At 300 °C and 350 °C, the Mo 3*d* peaks clearly shifted to lower binding energies that correspond to the oxidation state of Mo in $MoSe_2$.[20,21,45] Positions of the Mo $3d_{5/2}$ and Mo $3d_{3/2}$ doublet were 228.4 eV and 231.7 eV, respectively. The Se 3*d* peaks also exhibited a similar trend as a function of annealing temperature. At 300 °C and 350 °C, the Se 3*d* peaks were also shifted to a lower binding energy that corresponds to the oxidation state of selenide in $MoSe_2$. At 400 °C, the film was decomposed to form MoO_3 presumably due to trace oxygen present in the annealing atmosphere.[46,47] Also shown in Figure 3.13 are the XPS spectra of a sample made by replacing the SeO_2 solution with a blank solution during its deposition. Consequently, this deposit was composed of entirely MoO_x. The Mo 3*d* peaks of this "Mo-blank" deposit had higher binding energies than those of a normal $MoSe_2$ deposit. This is in agreement with the initial prospect that Se can be used to suppress Mo oxidation in the formation of $MoSe_2$.

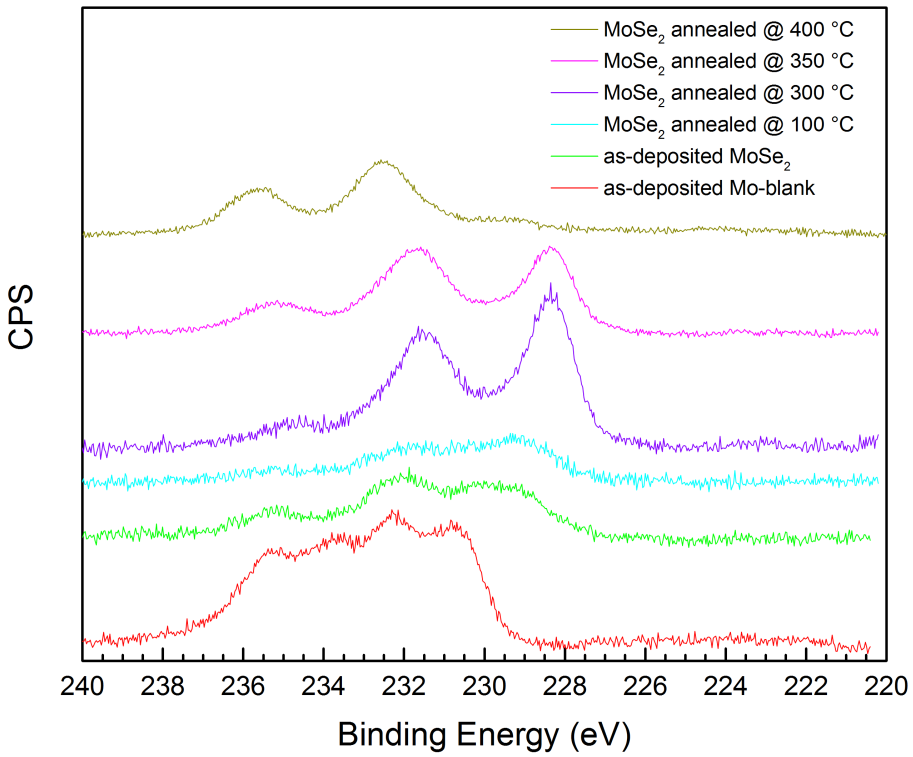

(a)

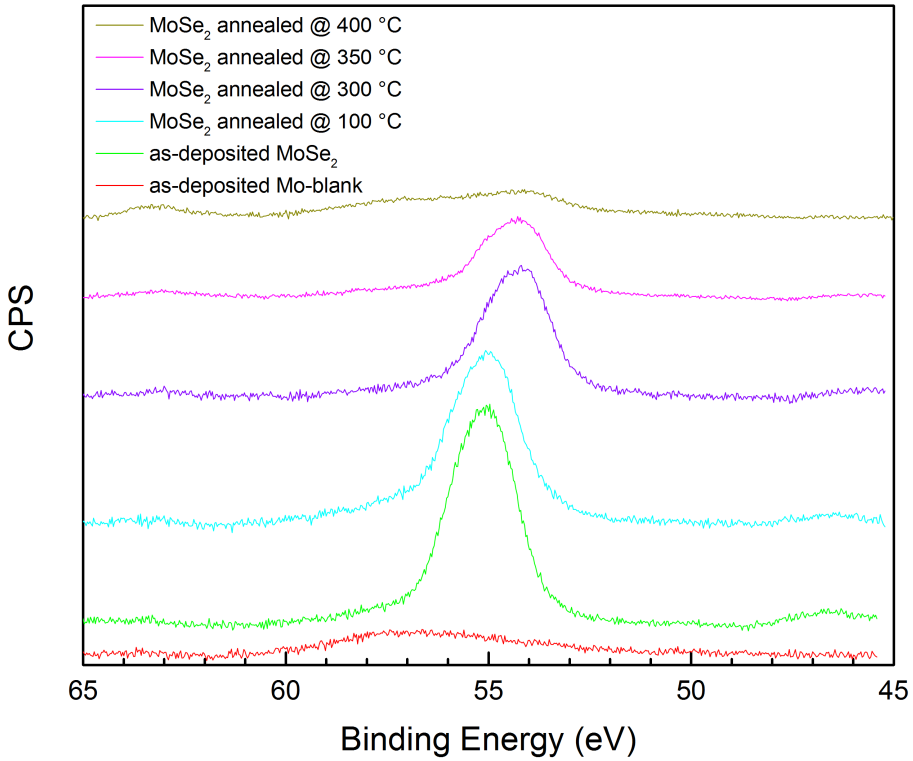

(b)

Figure 3.13: XPS spectra of the as-deposited and annealed $MoSe_2$ samples showing (a) the Mo 3*d* and (b) the Se 3*d* photoelectric peaks.

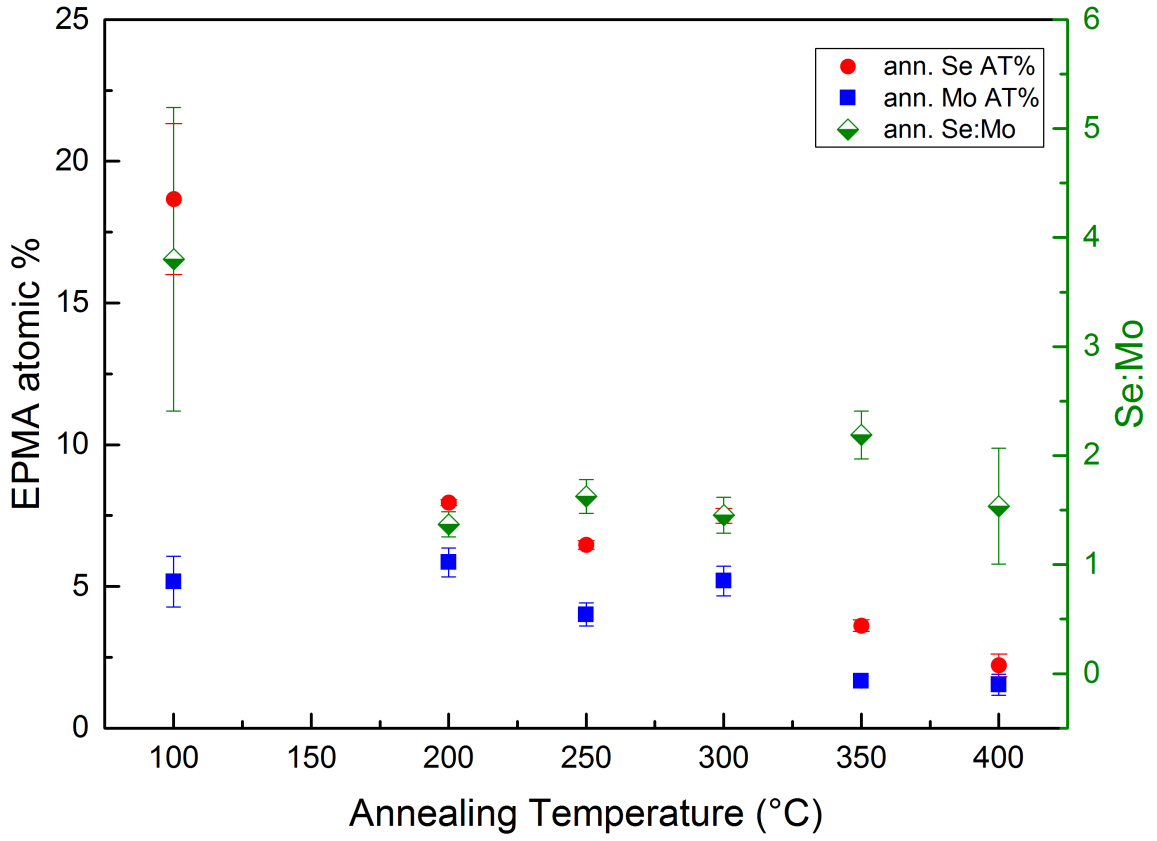

Figure 3.14: Composition analysis by EPMA of the deposits annealed at different temperatures. These deposits were grown using $E1 = -100\,\mathrm{mV}$ and $E2 = -450\,\mathrm{mV}$.

Both Raman and XPS data clearly showed the presence of $MoSe_2$ in samples annealed at 250 °C and above. Although 1 % H_2 was used during the annealing in an attempt to provide a reducing environment, its effect was deemed negligible. Samples annealed in pure N_2 also showed clear evidence of $MoSe_2$ by XPS, even though N_2 would not provide the necessary reducing environment to form $MoSe_2$.[19] Figure 3.14 shows composition analysis of the annealed deposits by EPMA. As the annealing temperature increased, there was an apparent loss of Se and Mo from the deposits compared to the as-deposited films. $MoSe_2$ is thermally stable up to almost 1000 °C, so the loss of Se and Mo content were most likely impurities in the deposits (Se and MoO_x).[48] A sample's surface is more susceptible to oxidation than its bulk; therefore, the surface was expected to have the most impurities. Removal of the surface impurities by annealing may explain the observed XPS peak shifts. While the annealed samples were amorphous by XRD, their crystallinity could still have been improved by annealing, which would account for the evolution of the $MoSe_2$ Raman peaks as a function of temperature.

A $MoSe_2$ sample annealed at 350 °C was imaged by STM and SEM. These images are shown in Figure 3.15. The disparity in the shape of the crystallites between the two images suggests the circular shapes observed in STM were due to a tip effect. Despite the misleading shapes, the height contrast in the STM image does reveal the stacking nature of the flakes in the sample, consistent with the van der Waals character of the 2D material. Figure 3.16 shows an SEM image of the STM tip after it was used to image the $MoSe_2$ sample. Thin $MoSe_2$ flakes, confirmed by EDS, were attached to the W tip during STM imaging, presumably owing to their weak adhesion to the film substrate. Some of the flakes on the tip resembled the typical triangular shape of $MoSe_2$ and MoS_2 grown by chemical vapor deposition (CVD).[19,49–51]

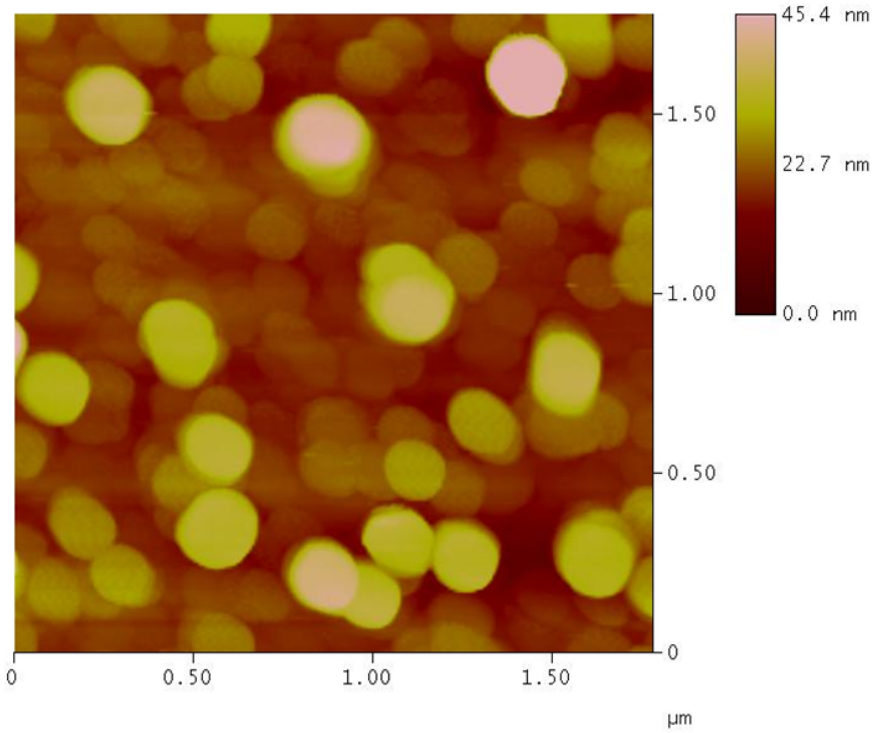

(a)

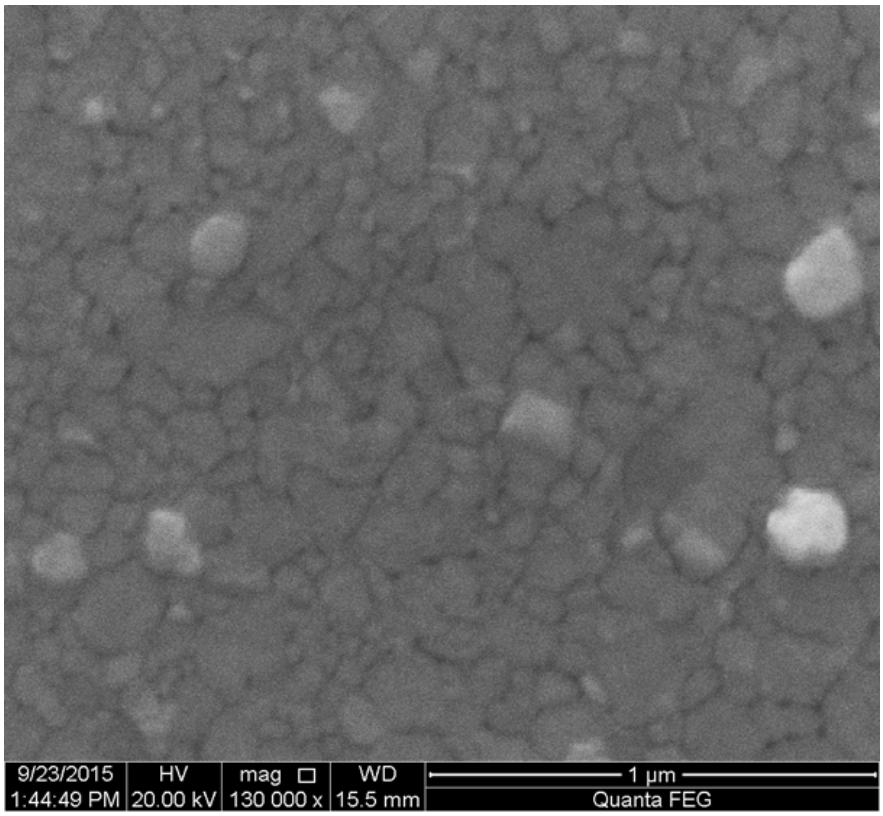

(b)

Figure 3.15: (a) STM and (b) SEM images of a $MoSe_2$ sample annealed at 350 °C.

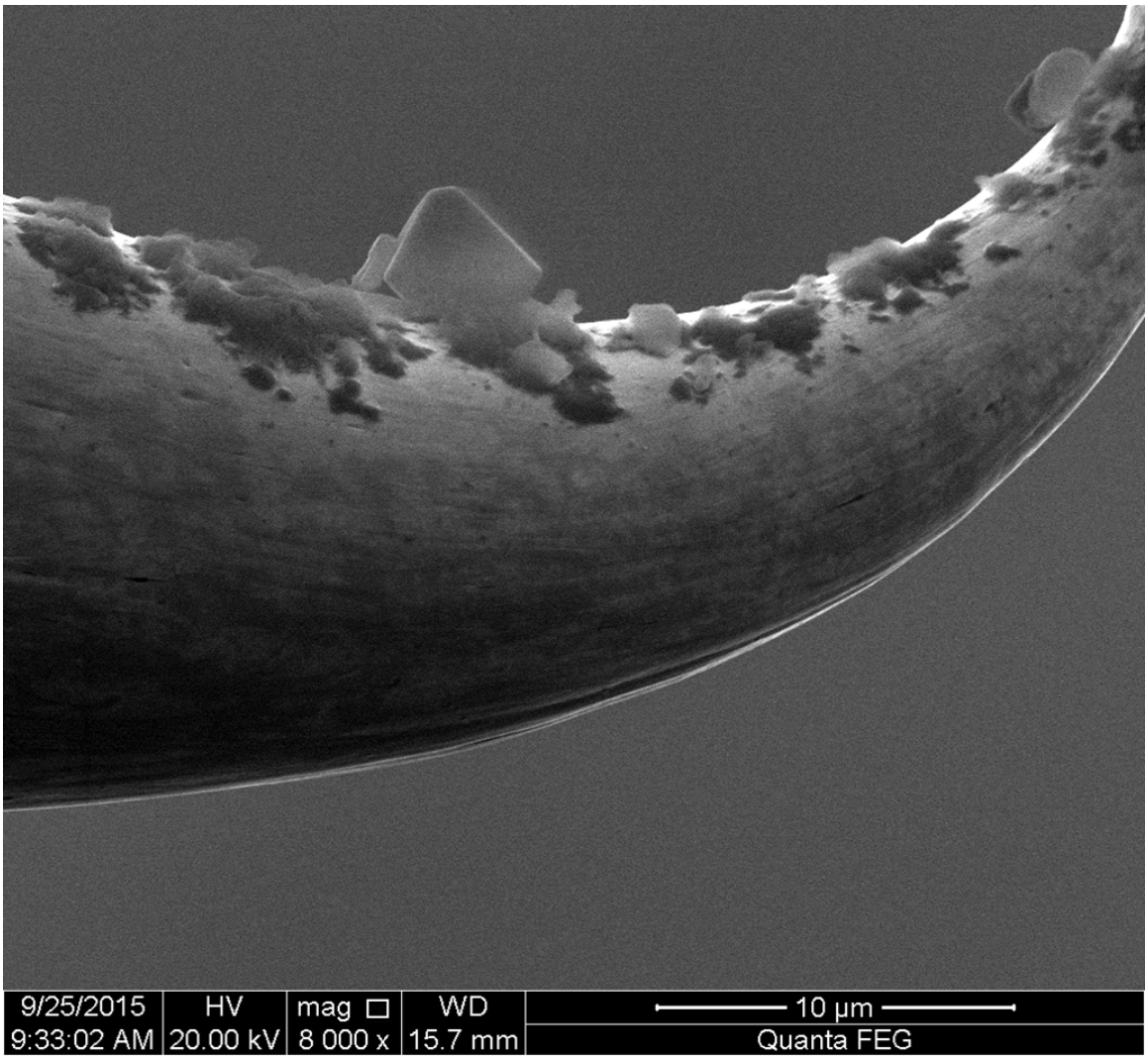

Figure 3.16: SEM of the STM tip after it was used to image the $MoSe_2$ sample.

3.5 Conclusion

The voltammetric behaviors of Au in MoO_3 and SeO_2 solutions were examined in both basic and acidic conditions. Preliminary thin films of $MoSe_2$ were successfully prepared by E-ALD using the acidic solutions of both precursors. PEC photovoltage measurement confirmed the presence of $MoSe_2$ as well as MoO_2 impurity in the as-deposited films. The impurities can be removed by thermal annealing. The enrichment of $MoSe_2$ in the annealed films was confirmed by XPS. The evolution of $MoSe_2$ Raman peaks as a function of temperature suggested there was an improvement in film crystallinity by annealing, though the films were still amorphous by XRD. Although the film growth conditions were not yet fully optimized, this study demonstrated that E-ALD can be used to grow $MoSe_2$ films. The premise of growing $MoSe_2$ by using Se to induce Mo deposition might be applicable to growing other dichalcogenides of molybdenum or tungsten. That would lead to the prospect of using E-ALD to grow TMDC heterostructures, which exhibit interesting novel properties for potential applications in electronic and optoelectronic devices.

3.6 Acknowledgments

Support for this work, from NSF ECCS, award number 1124733, is gratefully acknowledged. Helpful discussions from Chris Fleisher and for the use of the UGA Electron Microprobe Lab are appreciated. Dr. Zhengwei Pan is also appreciated for the use of his SEM.

References

(1) Novoselov, K. S.; Geim, A. K.; Morozov, S. V.; Jiang, D.; Zhang, Y.; Dubonos, S. V.; Grigorieva, I. V.; Firsov, A. A. Electric field effect in atomically thin carbon films. *Science* **2004**, *306*, 666–669.

(2) Wang, Q. H.; Kalantar-Zadeh, K.; Kis, A.; Coleman, J. N.; Strano, M. S. Electronics and optoelectronics of two-dimensional transition metal dichalcogenides. *Nat Nano* **2012**, *7*, 699–712.

(3) Chhowalla, M.; Shin, H. S.; Eda, G.; Li, L. J.; Loh, K. P.; Zhang, H. The chemistry of two-dimensional layered transition metal dichalcogenide nanosheets. *Nature Chemistry* **2013**, *5*, 263–275.

(4) McMillan, W. L. Landau Theory of Charge-Density Waves in Transition-Metal Dichalcogenides. *Physical Review B* **1975**, *12*, 1187–1196.

(5) Renteria, J.; Samnakay, R.; Jiang, C.; Pope, T. R.; Goli, P.; Yan, Z.; Wickramaratne, D.; Salguero, T. T.; Khitun, A. G.; Lake, R. K.; Balandin, A. A. All-metallic electrically gated 2H-$TaSe_2$ thin-film switches and logic circuits. *Journal of Applied Physics* **2014**, *115*.

(6) Yan, Z.; Jiang, C.; Pope, T. R.; Tsang, C. F.; Stickney, J. L.; Goli, P.; Renteria, J.; Salguero, T. T.; Balandin, A. A. Phonon and thermal properties of exfoliated $TaSe_2$ thin films. *Journal of Applied Physics* **2013**, *114*.

(7) Tsang, C.; Kim, Y. G.; Gebregziabiher, D.; Stickney, J. Ta Surface Chemistry in Aqueous Solutions and the Possible Formation of $TaTe_2$ and TaS_3. *Journal of the Electrochemical Society* **2013**, *160*, D3278–D3284.

(8) Adzic, R. R. Electrocatalytic Properties of the Surfaces Modified by Foreign Metal Adatoms. *Advances in Electrochemistry and Electrochemical Engineering* **1984**, *13*, 159–260.

(9) Gregory, B. W.; Norton, M. L.; Stickney, J. L. Thin-Layer Electrochemical Studies of the Underpotential Deposition of Cadmium and Tellurium on Polycrystalline Au, Pt and Cu Electrodes. *Journal of Electroanalytical Chemistry* **1990**, *293*, 85–101.

(10) Gregory, B. W.; Stickney, J. L. Electrochemical Atomic Layer Epitaxy (ECALE). *Journal of Electroanalytical Chemistry* **1991**, *300*, 543–561.

(11) Kolb, D. M. Physical and electrochemical properties of metal monolayers on metallic substrates. *Adv. Electrochem. Electrochem. Eng.* **1978**, *11*, 125–271.

(12) Lister, T. E.; Stickney, J. L. Formation of the first monolayer of CdSe on Au(111) by electrochemical ALE. *Applied Surface Science* **1996**, *107*, 153–160.

(13) Venkatasamy, V.; Jayaraju, N.; Cox, S. M.; Thambidurai, C.; Happek, U.; Stickney, J. L. Optimization of CdTe nanofilm formation by electrochemical atomic layer epitaxy (EC-ALE). *Journal of Applied Electrochemistry* **2006**, *36*, 1223–1229.

(14) Venkatasamy, V.; Jayaraju, N.; Cox, S. M.; Thambidurai, C.; Mathe, M.; Stickney, J. L. Deposition of HgTe by electrochemical atomic layer epitaxy (EC-ALE). *Journal of Electroanalytical Chemistry* **2006**, *589*, 195–202.

(15) Mak, K. F.; Lee, C.; Hone, J.; Shan, J.; Heinz, T. F. Atomically Thin MoS_2: A New Direct-Gap Semiconductor. *Physical Review Letters* **2010**, *105*.

(16) Tongay, S.; Zhou, J.; Ataca, C.; Lo, K.; Matthews, T. S.; Li, J. B.; Grossman, J. C.; Wu, J. Q. Thermally Driven Crossover from Indirect toward Direct Bandgap in 2D Semiconductors: $MoSe_2$ versus MoS_2. *Nano Letters* **2012**, *12*, 5576–5580.

(17) Zhang, Y.; Chang, T. R.; Zhou, B.; Cui, Y. T.; Yan, H.; Liu, Z. K.; Schmitt, F.; Lee, J.; Moore, R.; Chen, Y. L.; Lin, H.; Jeng, H. T.; Mo, S. K.; Hussain, Z.; Bansil, A.; Shen, Z. X. Direct observation of the transition from indirect to direct bandgap in atomically thin epitaxial $MoSe_2$. *Nature Nanotechnology* **2014**, *9*, 111–115.

(18) Lopez-Sanchez, O.; Lembke, D.; Kayci, M.; Radenovic, A.; Kis, A. Ultrasensitive photodetectors based on monolayer MoS_2. *Nature Nanotechnology* **2013**, *8*, 497–501.

(19) Wang, X. L.; Gong, Y. J.; Shi, G.; Chow, W. L.; Keyshar, K.; Ye, G. L.; Vajtai, R.; Lou, J.; Liu, Z.; Ringe, E.; Tay, B. K.; Ajayan, P. M. Chemical Vapor Deposition Growth of Crystalline Monolayer $MoSe_2$. *ACS Nano* **2014**, *8*, 5125–5131.

(20) Saadi, F. H.; Carim, A. I.; Velazquez, J. M.; Baricuatro, J. H.; McCrory, C. C. L.; Soriaga, M. P.; Lewis, N. S. Operando Synthesis of Macroporous Molybdenum Diselenide Films for Electrocatalysis of the Hydrogen-Evolution Reaction. *ACS Catalysis* **2014**, *4*, 2866–2873.

(21) Wang, H. T.; Kong, D. S.; Johanes, P.; Cha, J. J.; Zheng, G. Y.; Yan, K.; Liu, N. A.; Cui, Y. $MoSe_2$ and WSe_2 Nanofilms with Vertically Aligned Molecular Layers on Curved and Rough Surfaces. *Nano Letters* **2013**, *13*, 3426–3433.

(22) Tributsch, H. Hole Reactions from d-Energy Bands of Layer Type Group VI Transition Metal Dichalcogenides: New Perspectives for Electrochemical Solar Energy Conversion. *Journal of the Electrochemical Society* **1978**, *125*, 1086–1093.

(23) Bard, A. J.; Parsons, R.; Jordan, J.; Editors, *Standard Potentials in Aqueous Solution*; Marcel Dekker, Inc.: 1985, p 834.

(24) Enghag, P. In *Encyclopedia of the Elements*; Wiley-VCH Verlag GmbH & Co. KGaA: 2007, pp 589–604.

(25) Morley, T. J.; Penner, L.; Schaffer, P.; Ruth, T. J.; Benard, F.; Asselin, E. The deposition of smooth metallic molybdenum from aqueous electrolytes containing molybdate ions. *Electrochemistry Communications* **2012**, *15*, 78–80.

(26) Syed, R.; Ghosh, S. K.; Sastry, P. U.; Sharma, G.; Hubli, R.; Chakravartty, J. K. Electrodeposition of thick metallic amorphous molybdenum coating from aqueous electrolyte. *Surface & Coatings Technology* **2015**, *261*, 15–20.

(27) Elezovic, N. R.; Jovic, V. D.; Krstajic, N. V. Kinetics of the hydrogen evolution reaction on Fe-Mo film deposited on mild steel support in alkaline solution. *Electrochimica Acta* **2005**, *50*, 5594–5601.

(28) Pellicer, E.; Gomez, E.; Valles, E. Use of the reverse pulse plating method to improve the properties of cobalt-molybdenum electrodeposits. *Surface & Coatings Technology* **2006**, *201*, 2351–2357.

(29) Anand, T. J. S.; Sanjeeviraja, C.; Jayachandran, M. Preparation of layered semiconductor ($MoSe_2$) by electrosynthesis. *Vacuum* **2001**, *60*, 431–435.

(30) Chandra, S.; Sahu, S. N. Electrodeposited semiconducting molybdenum selenide films. I. Preparatory technique and structural characterisation. *Journal of Physics D: Applied Physics* **1984**, *17*, 2115.

(31) Delphine, S. M.; Jayachandran, M.; Sanjeeviraja, C. Pulsed electrodeposition and characterization of molybdenum diselenide thin film. *Materials Research Bulletin* **2005**, *40*, 135–147.

(32) Hankare, P. P.; Chate, P. A.; Delekar, S. D.; Bhuse, V. M.; Asabe, M. R.; Jadhav, B. V.; Garadkar, K. M. Structural and opto-electrical properties of

molybdenum diselenide thin films deposited by chemical bath method. *Journal of Crystal Growth* **2006**, *291*, 40–44.

(33) Shirley, D. A. High-Resolution X-Ray Photoemission Spectrum of Valence Bands of Gold. *Physical Review B* **1972**, *5*, 4709.

(34) Emery, S. B.; Hubbley, J. L.; Roy, D. Voltammetric and amperometric analyses of electrochemical nucleation: electrodeposition of copper on nickel and tantalum. *Journal of Electroanalytical Chemistry* **2004**, *568*, 121–133.

(35) Pourbaix, M., *Atlas of Electrochemical Equilibria in Aqueous Solutions*; Pergamon: 1966.

(36) Huang, B. M.; Lister, T. E.; Stickney, J. L. Se adlattices formed on Au(100), studies by LEED, AES, STM and electrochemistry. *Surface Science* **1997**, *392*, 27–43.

(37) Sorenson, T. A.; Wilmer, B. K.; Stickney, J. L. Electrochemical digital etching: Atomic level studies of CdTe(100). *Solid-Liquid Electrochemical Interfaces* **1997**, *656*, 115–125.

(38) Stickney, J. L.; Rosasco, S. D.; Schardt, B. C.; Solomun, T.; Hubbard, A. T.; Parkinson, B. A. Demonstration of the Surface Stability of the van der Waals Surface (0001) of $MoSe_2$ by LEED and Electrochemistry. *Surface Science* **1984**, *136*, 15–22.

(39) Sato, N., *Electrochemistry at metal and semiconductor electrodes*; Elsevier: Amsterdam ; New York, 1998.

(40) Stenzel, O., *The physics of thin film optical spectra: an introduction*; Springer Series in Surface Sciences; Springer: Berlin, 2005.

(41) Dukstiene, N.; Sinkeviciute, D. Photoelectrochemical properties of MoO_2 thin films. *Journal of Solid State Electrochemistry* **2013**, *17*, 1175–1184.

(42) Kam, K. K.; Parkinson, B. A. Detailed Photocurrent Spectroscopy of the Semiconducting Group-VI Transition-Metal Dichalcogenides. *Journal of Physical Chemistry* **1982**, *86*, 463–467.

(43) Larentis, S.; Fallahazad, B.; Tutuc, E. Field-effect transistors and intrinsic mobility in ultra-thin $MoSe_2$ layers. *Applied Physics Letters* **2012**, *101*, 223104.

(44) Terrones, H.; Corro, E. D.; Feng, S.; Poumirol, J. M.; Rhodes, D.; Smirnov, D.; Pradhan, N. R.; Lin, Z.; Nguyen, M. A. T.; Elías, A. L.; Mallouk, T. E.; Balicas, L.; Pimenta, M. A.; Terrones, M. New First Order Raman-active Modes in Few Layered Transition Metal Dichalcogenides. *Scientific Reports* **2014**, *4*, 4215.

(45) Abdallah, W. A.; Nelson, A. E. Characterization of $MoSe_2$(0001) and ion-sputtered $MoSe_2$ by XPS. *Journal of Materials Science* **2005**, *40*, 2679–2681.

(46) Magie, P. M. A Review of Properties and Potentials of New Heavy Metal Derivative Solid Lubricants. *Lubrication Engineering* **1966**, *22*, 262.

(47) Shi, H. Q.; Zhou, X. D.; Lin, Y. S.; Fu, X. Synthesis of $MoSe_2$ nano-flakes modified with dithiophosphinic acid extractant at low temperature. *Materials Letters* **2008**, *62*, 3649–3651.

(48) Brainard, W. A. *Thermal stability and friction of the disulfides, diselenides, and ditellurides of molybdenum and tungsten in vacuum (*10^{-9} *to* 10^{-6} *Torr)*; tech. rep. NASA-TN-D-5141; Lewis Research Center, 1969.

(49) Chang, Y. H.; Zhang, W.; Zhu, Y.; Han, Y.; Pu, J.; Chang, J. K.; Hsu, W. T.; Huang, J. K.; Hsu, C. L.; Chiu, M. H.; Takenobu, T.; Li, H.; Wu, C. I.; Chang, W. H.; Wee, A. T. S.; Li, L. J. Monolayer $MoSe_2$ Grown by Chemical Vapor Deposition for Fast Photodetection. *ACS Nano* **2014**, *8*, 8582–8590.

(50) Duan, X. D.; Wang, C.; Shaw, J. C.; Cheng, R.; Chen, Y.; Li, H. L.; Wu, X. P.; Tang, Y.; Zhang, Q. L.; Pan, A. L.; Jiang, J. H.; Yu, R. Q.; Huang, Y.; Duan, X. F. Lateral epitaxial growth of two-dimensional layered semiconductor heterojunctions. *Nature Nanotechnology* **2014**, *9*, 1024–1030.

(51) Ling, X.; Lee, Y. H.; Lin, Y. X.; Fang, W. J.; Yu, L. L.; Dresselhaus, M. S.; Kong, J. Role of the Seeding Promoter in MoS_2 Growth by Chemical Vapor Deposition. *Nano Letters* **2014**, *14*, 464–472.

Chapter 4

Conclusion and Future Studies

In order to devise a synthetic route for forming Ta/Nb chalcogenides by E-ALD, the electrochemical oxide reduction of Ta was studied by CV, EC-STM and XPS. Initial data from CV hinted that some oxide can be reduced at very negative potentials, as the HER current was correlated with the amount of surface oxide present. In the EC-STM study, an oxide-removal step at $-1.8\,\mathrm{V}$ was used prior to obtaining atomically-resolved images of a bare Ta surface. To avoid interference from the extensive HER occurring at such a negative potential, the imaging was performed at more positive potentials. The imaging process showed that an oxide-free Ta surface would spontaneously re-oxidize even at $-1\,\mathrm{V}$. Use of Te to passivate the Ta surface also resulted in atomic resolution, and suggested greatly increased stability, up to as much as $-0.3\,\mathrm{V}$. Following the deposition of Te onto Ta, a "double zigzag" pattern was observed in some STM images as evidence of $TaTe_2$ formed on the surface. S and Cu were also deposited onto Ta following the oxide-removal step. EC-STM of the S layer on Ta displayed rod-like structures that resemble TaS_3 chains. CV and XPS data also support these conclusions.

Being able to deposit onto a Ta substrate was not enough to create an E-ALD cycle for making Ta chalcogenides. A reliable Ta electrodeposition method was still missing. Attempts to deposit Ta from aqueous carboxylate-based precursors were made. Preliminary results from electrolysis of the precursors to deposit Ta onto Au indicated only the presence of Ta oxides by XPS. Even though the final precursor solutions were fluoride-free, very concentrated amount of HF at elevated temperatures

was still necessary in the early synthesis steps of the precursors.[1] The solutions were sometimes found to be unstable and precipitations, presumably Ta_2O_5, would form. The difficulty and hazard of preparing a reliable Ta precursor solution prompted a shift of focus toward electrodepositing Mo chalcogenides. The premise was that Mo is also a refractory metal like Ta that is highly reactive in the presence of oxygen. Because electroreduction of Mo is also greatly hindered by hydrogen evolution reaction in aqueous media, a method that overcomes this obstacle might be applicable to depositing Ta as well.

The voltammetric behaviors of Au in MoO_3 and SeO_2 solutions were studied to evaluate the feasibility of depositing $MoSe_2$. CVs have been performed in both basic and acidic conditions. MoO_x oxidation features appeared very similar in both basic and acidic conditions, suggesting the products of electrolysis in the MoO_3 solutions were the same for the basic and acidic solutions. On the contrary, Se deposition was much more pH-dependent. Among the conditions tested, pH 1.5 was the best for Se deposition. Preliminary thin films of $MoSe_2$ were prepared by E-ALD using the acidic solutions of both precursors. PEC photovoltage measurement confirmed the coexistence of $MoSe_2$ and MoO_2 impurity in the as-deposited films. The impurities can be removed by thermal annealing. XPS confirmed that the annealed films were enriched with $MoSe_2$. Micro-Raman spectroscopy was used to follow the annealing study. The Raman peaks characteristic of $MoSe_2$ emerged as a function of annealing temperature. The evolution of the $MoSe_2$ Raman peaks suggested there was an improvement in film crystallinity by annealing, though the films were still amorphous by XRD. This study demonstrated that E-ALD can be used to grow $MoSe_2$ films.

The growth conditions for $MoSe_2$ was not yet fully optimized. A different potential profile during the electrodeposition can be used to further induce $MoSe_2$ formation over MoO_x deposition. For instance, a brief but large negative potential pulse can be inserted into the E-ALD cycle to thoroughly reduce MoO_x and subsequently react it

with Se. The premise of growing $MoSe_2$ by using Se to induce Mo deposition might be applicable to growing other dichalcogenides of molybdenum or tungsten. If individual E-ALD cycles are made for creating different MX_2 materials, they can be combined to grow MX_2 heterostructures.[2–6] Sequential growth of heterostructures by the common MX_2 growth methods often failed.[7] A problem tends to be the passivation of the edges upon exposure to ambient conditions, which can no longer act as nucleation sites for subsequent growth of a different MX_2. Another problem is the first MX_2 usually cannot withstand the significant temperature changes in switching to a new growth condition for the second MX_2. E-ALD is performed at or near room temperature, and it is compatible for growing superlattices and heterostructures.[8,9] That raises the prospect of using E-ALD to grow TMDC heterostructures in future studies. The research area of TMDC heterostructures is currently very active. These materials exhibit interesting novel properties suitable for applications in electronic and optoelectronic devices. Without a doubt, there is a strong demand for a reliable route to synthesizing high-quality TMDC heterostructures.

References

(1) Panda, A. B.; Tarafdar, A.; Pramanik, P. Synthesis, characterization and properties of nano-sized $SrBi_2Ta_2O_9$ ceramics prepared by chemical routes. *Journal of the European Ceramic Society* **2004**, *24*, 3043–3048.

(2) Li, M. Y.; Shi, Y. M.; Cheng, C. C.; Lu, L. S.; Lin, Y. C.; Tang, H. L.; Tsai, M. L.; Chu, C. W.; Wei, K. H.; He, J. H.; Chang, W. H.; Suenaga, K.; Li, L. J. Epitaxial growth of a monolayer WSe_2-MoS_2 lateral p-n junction with an atomically sharp interface. *Science* **2015**, *349*, 524–528.

(3) Huang, C. M.; Wu, S. F.; Sanchez, A. M.; Peters, J. J. P.; Beanland, R.; Ross, J. S.; Rivera, P.; Yao, W.; Cobden, D. H.; Xu, X. D. Lateral heterojunctions within monolayer $MoSe_2-WSe_2$ semiconductors. *Nature Materials* **2014**, *13*, 1096–1101.

(4) Lee, C. H.; Lee, G. H.; van der Zande, A. M.; Chen, W. C.; Li, Y. L.; Han, M. Y.; Cui, X.; Arefe, G.; Nuckolls, C.; Heinz, T. F.; Guo, J.; Hone, J.; Kim, P. Atomically thin p-n junctions with van der Waals heterointerfaces. *Nature Nanotechnology* **2014**, *9*, 676–681.

(5) Gong, Y. J.; Lin, J. H.; Wang, X. L.; Shi, G.; Lei, S. D.; Lin, Z.; Zou, X. L.; Ye, G. L.; Vajtai, R.; Yakobson, B. I.; Terrones, H.; Terrones, M.; Tay, B. K.; Lou, J.; Pantelides, S. T.; Liu, Z.; Zhou, W.; Ajayan, P. M. Vertical and in-plane heterostructures from WS_2/MoS_2 monolayers. *Nature Materials* **2014**, *13*, 1135–1142.

(6) Fang, H.; Battaglia, C.; Carraro, C.; Nemsak, S.; Ozdol, B.; Kang, J. S.; Bechtel, H. A.; Desai, S. B.; Kronast, F.; Unal, A. A.; Conti, G.; Conlon, C.; Palsson, G. K.; Martin, M. C.; Minor, A. M.; Fadley, C. S.; Yablonovitch,

E.; Maboudian, R.; Javey, A. Strong interlayer coupling in van der Waals heterostructures built from single-layer chalcogenides. *Proceedings of the National Academy of Sciences of the United States of America* **2014**, *111*, 6198–6202.

(7) Duan, X. D.; Wang, C.; Shaw, J. C.; Cheng, R.; Chen, Y.; Li, H. L.; Wu, X. P.; Tang, Y.; Zhang, Q. L.; Pan, A. L.; Jiang, J. H.; Yu, R. Q.; Huang, Y.; Duan, X. F. Lateral epitaxial growth of two-dimensional layered semiconductor heterojunctions. *Nature Nanotechnology* **2014**, *9*, 1024–1030.

(8) Banga, D.; Perdue, B.; Stickney, J. Electrodeposition of a PbTe/CdTe superlattice by electrochemical atomic layer deposition (E-ALD). *Journal of Electroanalytical Chemistry* **2014**, *716*, 129–135.

(9) Wade, T. L.; Vaidyanathan, R.; Happek, U.; Stickney, J. L. Electrochemical formation of a III-V compound semiconductor superlattice: InAs/InSb. *Journal of Electroanalytical Chemistry* **2001**, *500*, 322–332.